Technical Design Report
for the
Paul Scherrer Institute Experiment R-12-01.1: Studying the Proton "Radius" Puzzle with μp Elastic Scattering

The MUon proton Scattering Experiment collaboration (MUSE):

A. Afanasev,[1] J. Arrington,[2] O. Ates,[3] F. Benmokhtar,[4] J. Bernauer,[5] E. Brash,[4] W.J. Briscoe,[1] K. Deiters,[6] J. Diefenbach,[3] C. Djalali,[7] B. Dongwi,[3] E. Downie,[1] L. El Fassi,[8] E. Fuchey,[9] S. Gilad,[5] R. Gilman (Contact person),[8] R. Gothe,[7] D. Higinbotham,[10] Y. Ilieva,[7] H. Jiang,[7] M. Kohl,[3] G. Kumbartzki,[8] J. Lichtenstadt,[11] A. Liyanage,[3] N. Liyanage,[12] M. Meziane,[13] Z.-E. Meziani,[9] D.G. Middleton,[14] P. Monaghan,[3] K.E. Myers,[8] C. Perdrisat,[15] E. Piasetzsky,[11] V. Punjabi,[16] R. Ransome,[8] D. Reggiani,[6] A. Richter,[17] G. Ron (Spokesperson),[18] A. Sarty,[19] E. Schulte,[9] S. Strauch,[7] V. Sulkosky,[5] A.S. Tadepalli,[8] and L. Weinstein[20]

[1] *George Washington University, Washington, DC, USA*
[2] *Argonne National Lab, Argonne, IL, USA*
[3] *Hampton University, Hampton, Virginia, USA*
[4] *Christopher Newport University, Newport News, Virginia, USA*
[5] *Massachusetts Institute of Technology, Cambridge, Massachusetts, USA*
[6] *Paul Scherrer Institut, CH-5232 Villigen, Switzerland*
[7] *University of South Carolina, Columbia, South Carolina, USA*
[8] *Rutgers University, New Brunswick, New Jersey, USA*
[9] *Temple University, Philadelphia, Pennsylvania, USA*
[10] *Jefferson Lab, Newport News, Virginia, USA*
[11] *Tel Aviv University, Tel Aviv, Israel*
[12] *University of Virginia, Charlottesville, Virginia, USA*
[13] *Duke University, Durham, North Carolina, USA*
[14] *Institut für Kernphysik, Johannes Gutenberg Universität, Mainz 55099, Germany*
[15] *College of William & Mary, Williamsburg, Virginia, USA*
[16] *Norfolk State University, Norfolk, Virginia, USA*

[17]*Technical University of Darmstadt, Darmstadt, Germany*
[18]*Hebrew University of Jerusalem, Jerusalem, Israel*
[19]*St. Mary's University, Halifax, Nova Scotia, Canada*
[20]*Old Dominion University, Norfolk, Virginia, USA*

Two years after the radius of muonic hydrogen was first reported, it is now known to be 7σ inconsistent with combined world ep atom and scattering experiment results. We propose to measure $\mu^{\pm}p$ and $e^{\pm}p$ scattering in the same experiment at the same time, which allows a precise comparison of the proton radius determined with electrons and muons, and more generally provides the best test of lepton universality in a scattering experiment to date, about an order of magnitude improvement over previous tests. Measuring both particle polarities will allow a test of two-photon exchange at the $\approx$1% level, about a factor of four improvement on previous low momentum transfer determinations, and similar to the current generation of higher momentum transfer electron experiments. The experiment has the potential to demonstrate whether the μp and ep interactions are consistent or different, and whether any difference results from novel physics or two-photon exchange.

CONTENTS

I. MOTIVATION

The proton radius was thought to be reliably determined to be ≈0.88 fm for several years, by atomic hydrogen and *ep* scattering measurements. The hydrogen atom experiments led, in the 2006 CODATA analysis [1], to $r_p = 0.8768 \pm 0.0069$ fm. The electron-proton scattering analysis gave $r_p = 0.895 \pm 0.018$ fm in the analysis of [2], which discussed the needed Coulomb corrections and choice of an appropriate parameterization to fit form factor data. This situation changed in summer 2010 when a Paul Scherrer Institute (PSI) experiment [3] reported that the radius determined from muonic hydrogen level transitions is 0.842 ± 0.001 fm, about 5σ off from the nearly order of magnitude less precise non-muonic measurements. We refer to this situation as the proton radius puzzle.

The proton radius puzzle is quite possibly more puzzling now than when it first appeared. First, while there have been a number of suggestions of possible resolutions to the puzzle, several appear to be ruled out or severely constrained based on other measurements, and none are generally accepted. Second, two new electron scattering experiments have reported their data along with new analyses of the proton radius, which increase the discrepancy to be greater than 7σ. One experiment was a precise cross section measurement [4] at Mainz that determined ≈1400 cross sections in the range $Q^2 = 0.01 \rightarrow 1$ GeV^2. The Mainz analysis of only their data with a wide range of functional forms gave a proton electric radius of 0.879 ± 0.008 fm. The second experiment [5] at Jefferson Lab measured $\vec{e}p \rightarrow e'\vec{p}$ to determine 1% form factor ratios in the range $\mathrm{Q}^2 = 0.3 \rightarrow 0.8$ GeV^2. A world analysis of data (excluding the Mainz data set) resulted in a radius of 0.870 ± 0.010 fm, consistent with the Mainz electric radius determination – although there were differences in the magnetic radius determination. A partial summary of recent proton radius extractions is shown in Figure 1.

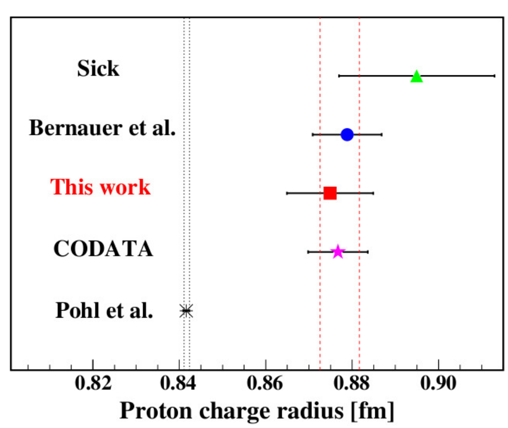

FIG. 1. A summary of some recent proton electric radius determinations, taken from [5].

The proton radius puzzle has attracted wide interest. There are several possible explanations for the puzzle.

- *Beyond standard model physics.* Several articles have appeared that propose possible novel physics that distinguishes μp from ep interactions. At this point we are unaware of any proposed physics that is generally accepted as an explanation. As an example, in [6] the possibility of a new $U(1)_R$ gauge symmetry is discussed, which leads to different μp and ep interactions. A proposed test is enhanced parity violation in μp scattering, orders of magnitude enhanced from the expected parity violation from Z^0 exchange. However, Ref. [7] points out that this model involves a new vector gauge boson with mass around tens of MeV, which could be radiated from muons. The lack of observation of such a boson in, e.g, $K \to \mu\nu$ severely constrains such models. Additional experimental limits on this idea are discussed below.

- *Novel two-photon exchange effects.* When the interaction in the bound atom or in the scattering process involves the exchange of two photons, the intermediate state is an off-shell proton, possibly an excited state of the proton. The relativistic bound state problem remains a difficult and arguably unsolved problem. In [8, 9, 10], it was suggested that the two-photon exchange correction has an effect from the proton being off shell, leading to larger corrections in the μp case than in the ep case. The idea is controversial, and it appears at present consistency with other data makes this effect too small to explain the radius puzzle [11].

- *Unexpected aspects of proton structure.* Extracting the radius from the muonic hydrogen Lamb shift requires a proton structure correction. Atomic physics calculations result in $L^{th}(meV) = 209.9779 - 5.2262\langle r_p^2\rangle + 0.00913\langle r_p^3\rangle_{(2)}$ where L^{th} is the measured Lamb shift, $\langle r_p^2\rangle$ is the proton radius, and $\langle r_p^3\rangle_{(2)}$ is a correction from the third Zemach moment of the proton, given by $\langle r_p^3\rangle_{(2)} = (48/\pi)\int_0^\infty (dq/q^4)[G_E^2(q) - q^2\langle r_p^2\rangle/3 - 1]$. The third Zemach moment depends mostly on $G_E(Q^2)$ at low Q^2. De Rújula [12, 13] suggested that $\langle r_p^3\rangle_{(2)}$ might be anomalously large. This result is inconsistent with standard fits of the proton electric form factor [14, 15]. This issue was investigated further in [16], which demonstrated that one can add bumps to unmeasured low Q^2 regions of $G_E(Q^2)$ that result in large $\langle r_p^3 \rangle_{(2)}$. Such structures are not predicted by any model of the proton structure of which we are aware. A recent discussion of the atomic physics corrections and their uncertainties is in Ref. [17].

- *Atomic Physics Corrections:* While errors or issues in the atomic physics calculations are in principle a possibility, the radius puzzle has led to a reexamination of the atomic physics that goes into the radius extraction. No significant problems have been found, although there are general critiques of the theory – see, e.g., [18]. At this point, we are unaware of any criticisms of the value of the radius extracted from atomic hydrogen measurements, but there is a criticism that the uncertainty in the radius is not as good as claimed. The essential argument is that many of the atomic physics measurements are correlated, having been done by a few groups. The averaging of these measurements as if they were uncorrelated ignores the issue of correlated techniques and possibly errors. Thus, because of the correlations, the true uncertainty resulting from the atomic hydrogen measurements is not as small as given by the CODATA analysis.

- *Issues in ep Scattering:* The *ep* scattering data is corrected for radiative, including two-photon, corrections. The conventional radiative corrections are considered to be under control. The two-photon corrections have been an issue in higher Q^2 *ep* scattering, but all models and all evidence to date is that these corrections become relatively small at low Q^2. They have been considered at differing levels in the analyses of Bernauer *et al.* [4] and Zhan *et al.* [5], and it appears that the uncertainties in these corrections are insufficient to affect the μp vs. *ep* proton electric radius discrepancy.[1] Once the cross sections are established, the form factors and their slope at $Q^2 = 0$ need to be determined. One can fit Rosenbluth-separated form factors, or the cross sections and any polarization data directly. The use of a functional form might introduce a model dependence. Sick [2] emphasized the use of the continued fraction expansion and a restriction to low-Q^2 data, along

[1] Issues related to fitting and 2γ corrections have much more effect on extractions of the magnetic form factor and radius at low Q^2, due to the dominance of the electric form factor in most low Q^2 cross section measurements.

with the issues of a conventional Taylor series expansion. Bernauer *et al.* [4] found no significant differences when using a number of functional forms to extract the radius, although they did find that the conventional dipole formula is not consistent with more flexible parameterizations. Hill and Paz [19, 20] argued in favor of a constrained z expansion, concluding that the model dependence of other fits leads to an uncertainty about twice as large as reported. They obtained $r_E^p \approx 0.871 \pm 0.01$ fm, consistent with previous ep determinations, but slightly smaller, $\approx 3\sigma$ from the muonic hydrogen result. This fit does not include the recent Mainz and JLab data, or full 2γ exchange corrections. While the radius might be sensitive to the 2γ corrections and parameterization used for the low Q^2 expansion, recent extractions have examined these effects and attempted to include estimates of the corrections and associated uncertainties. The different extractions yield consistent results and find that these effects are significantly smaller than the discrepancy with the muonic hydrogen result.

The differences between the proton radius measured in the μp system and in ep systems is a surprise in part due to universality being generally accepted. Tests of the equivalence of μp and ep systems from a few decades ago provided constraints on violations of and possible differences between the widely accepted universality of ep and μp interactions. We give two examples here.

The radius of ^{12}C is one of the most precisely determined radii from electron scattering. The electron scattering result [21] is $\langle r^2 \rangle^{1/2} = 2.472 \pm 0.015$ fm, based on scattering of 25 – 115 MeV electrons at momentum transfers from 0.1 – 1.0 fm^{-1}, or $Q^2 \approx 0.0004$ - 0.04 GeV^2. A subsequent analysis of world data [22] found that dispersive corrections increase the extracted radius to 2.478 $\pm$ 0.009 fm. Nuclear charge radii were also measured by determining the $\approx$90 keV X-ray energies in muonic carbon atoms to several eV [23]. Assuming a harmonic oscillator nuclear charge distribution resulted in a ^{12}C radius of $\langle r^2 \rangle^{1/2}$ = 2.4715 $\pm$ 0.016 fm. A subsequent muonic atom experiment[24] found $\langle r^2 \rangle^{1/2} = 2.483 \pm$ 0.002 fm. There is evidently no μp vs. ep issue in the carbon radius determination. One can question whether one might have opposite effects in the case of μn vs. μp interactions, whether the orbital size dominates so any ep vs./ μp difference is suppressed, or whether there might be important corrections – e.g., 2γ effects – omitted from the analyses.

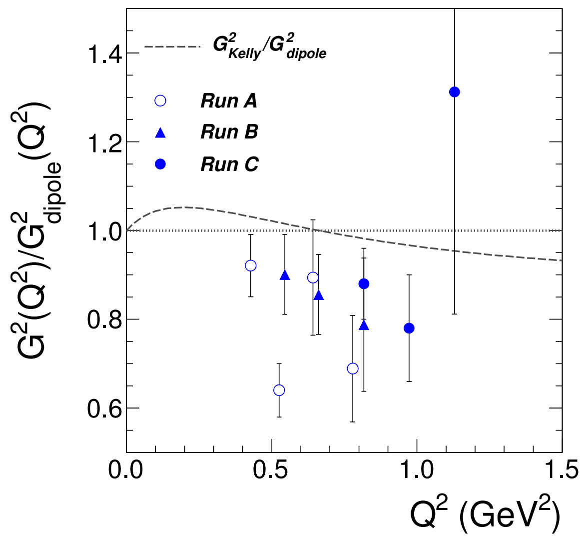

FIG. 2. Reduced cross sections, $d\sigma/d\Omega/d\sigma/d\Omega_{Mott}$, for μp elastic scattering, from Ellsworth *et al.* [25]. The data are somewhat below expectations from the dipole form factor parameterization. Use of the more modern Kelly parameterization [26] does not qualitatively change the result.

One of the better early μp elastic scattering experiments was Ellsworth *et al.* [25], which found that cross sections in the range $Q^2 \approx 0.5$ - 1 GeV^2 were about 15% below the standard dipole parameterization, $G_E = G_M/\mu_p = (1 + Q^2/0.71)^{-2}$ with Q^2 in GeV^2, and a similar percentage below modern form factor fits. as shown in Figure 2. While this suggests an ep vs. μp interaction difference, Ellsworth *et al.* interpreted the difference as an upper limit on any difference in μp and ep interactions. These data are too high in Q^2 to make any inferences about the proton radius. A subsequent experiment [27] covering $0.15 < Q^2 < 0.85$ GeV^2 found cross sections about 8% smaller than the electron scattering results, similar to [25], and considered the μp and ep scattering results consistent within uncertainties. A final elastic scattering experiment [28] analyzed the ratio of proton elastic form factors determined in μp and ep scattering as $G^2_{\mu p}/G^2_{ep} = N(1 + Q^2/\Lambda^2)^{-2}$, with the result that the normalizations are consistent with unity at the level of 10%, and the combined world μp data give $1/\Lambda^2 = 0.051 \pm 0.024$ GeV^{-2}, about 2.1σ from the electron-muon universality expectation of 0. For deep-inelastic scattering [29], a similar analysis yields a normalization consistent with unity at the level of 4% and $1/\Lambda^2 = 0.006 \pm 0.016$ GeV^{-2}. In summary, old comparisons of ep and μp elastic scattering have sometimes indicated several percent differences between μp and ep with similar size uncertainties, or sometimes indicated consistency with several percent uncertainties. The constraints on differing μp and ep interactions are not very good. While ep studies have advanced significantly in the past decade, the μp work has not.

Two-photon exchange effects have also been tested in μp scattering. In [30], no evidence was found for 2γ effects, with $\mu^+ p$ vs. $\mu^- p$ elastic scattering cross section asymmetries consistent with 0, with uncertainties from $4 \rightarrow 30\%$, and with no visible nonlinearities in Rosenbluth separations at $Q^2 \approx 0.3$ GeV^2. The Rosenbluth cross sections were determined to about 4%. Tests in ep scattering [31] have found no nonlinearities even with ≈1% cross sections; improved experiments are underway [32].

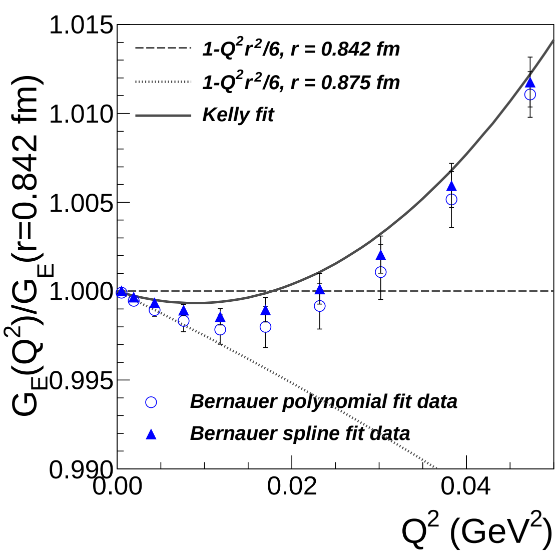

FIG. 3. Mainz results for the proton electric form factor determined by spline and polynomial fit analyses of the cross sections, along with the Kelly parameterization and a linear fit assuming the radius determined by ep measurements, relative to expectations from a linear fit using the radius determined from μp atoms. The data show that there is curvature in the form factors indicative of higher order contributions beyond the radius term. The very lowest Q^2 data are more consistent with a larger radius.

In *ep* scattering, the radius is determined from the slope of the form factor at $Q^2 = 0$. Here we consider the Mainz *ep* data in more detail, as it is related to the measurements that we will propose. Figure 3 shows an indication of the proton radius from the Mainz data set. The figure shows $G_E^p(Q^2)$ extracted from the cross sections using spline and polynomial fit functions to the data. Here one sees that the lowest Q^2 points are more consistent with the larger radius found in *ep* experiments, but that even before 0.02 GeV^2 the form factor is starting to show nonlinearities. The Kelly parameterization [26] generally predicts the trends of the data. The curvature at low Q^2 indicates the importance of measuring at low Q^2 to be sensitive to the radius.

Within the *ep* scattering community, the proton radius puzzle has led to studies about how to push the *ep* scattering measurements to lower Q^2, for the possibility that the experiments do not go to low enough Q^2 to see structure that might affect the radius determination from atomic physics measurements, as well as the form factor extrapolation to $Q^2 = 0$. An experimental proposal PR12-11-106 [33] was made to Jefferson Lab PAC38; it was conditionally approved by the PAC, which requested "an updated proposal with final target details, credible simulation of beam requirements including halo and stability, and a well defined path to extend reliability of radiative corrections to Q^2 down to 10^{-4}." But the JLab PAC considered the measurement of high importance, noting "*Testing of this result is among the most timely and important measurements in physics.*" It has since been upgraded to fully approved status by PAC39 in June 2012. Based on the JLab 12-GeV upgrade schedule, the experiment is not likely to run until 2016 or so. Studies have also been done of possible future experiments measuring high energy proton scattering on electrons [34], or using an *ep* collider [35]. However, it should be noted that the atomic hydrogen measurements are at even lower Q^2 than the muonic hydrogen measurements, and *ep* scattering and atomic hydrogen are consistent.

To summarize the situation, we quote from the Particle Data Group [36]: "Most measurements of the radius of the proton involve electron-proton interactions, and most of the more recent values agree with one another... However, a measurement using muonic hydrogen finds $r_p = 0.84184(67)$ fm, which is eight times more precise and seven standard deviations (using the CODATA 10 [37] error) from the electronic results... Until the difference between the *ep* and μp values is understood, it does not make much sense to average all the values together. For the present, we stick with the less precise (and provisionally suspect) CODATA 2010 value. *It is up to workers in this field to solve this puzzle.*" (Emphasis added.)

The resolution of the proton radius puzzle remains unclear. The resolution might arise from beyond standard model physics, novel two-photon exchange mechanisms / inadequacies in the theoretical treatment of the bound state problem, unexpected structure in the proton form factors, or issues and / or underestimated uncertainties in the determination of the radius from the actual experimental data. In the *ep* scattering community, a much discussed possible experimental approach to resolving this puzzle among the data from muonic hydrogen, atomic (*ep*) hydrogen, and *ep* elastic scattering is an improved low Q^2 *ep* elastic measurement.

Previous μp scattering data is of modest quality, and the proton radius has not been determined from μp scattering data. Thus our approach in this proposal is to measure the proton radius with μp elastic scattering and see if the results are consistent with electronic measurements or with muonic hydrogen. We will measure both μp and *ep* scattering at the same time to make the result more definitive – the relative uncertainties between μp and *ep* are much smaller than the absolute uncertainties, allowing a much better determination of the relative radius than the absolute radii. We will measure with both beam polarities to determine two-photon exchange effects – in much of our kinematic range our statistical uncertainties are smaller than the estimated uncertainties from two-photon exchange corrections.

II. EXPERIMENT OVERVIEW

A. Introduction

We are proposing a high-precision measurement of elastic *ep* and μp scattering, with absolute cross sections determined at the level of 1% – 2%, and relative cross sections (also for *ep* to μp) determined at the level of a few tenths of 1%. We use the πM1 beam line to generate a mixed e, μ, and π beam. We will take data at three beam momenta,[2] 115

[2] The momenta chosen are based on nominal detector positions, and will be re-optimized once the exact configuration of the experiment is known. Studies indicate that the momenta might change by a few MeV/c, which does not lead to significant differences in any projections in this report.

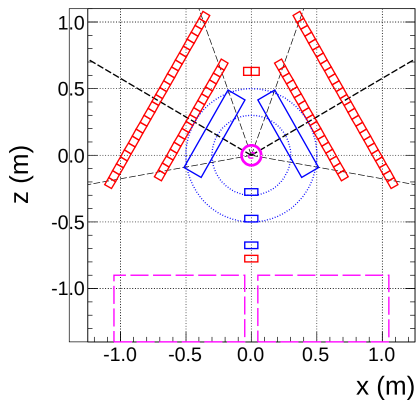

FIG. 4. Cartoon of the experimental systems in the πM1 area. In this view the beam proceeds vertically upward. Along the beamline we see (from bottom) a shielding wall, beam SciFi detector, three GEM chambers, the cryotarget and vacuum system, and the beam monitor scintillators. Scattered particles are detected by three drift chambers (shown as one blue box) and two planes of scintillator paddles, The light blue dotted circles indicate the annular table that will be used to support the chambers.

MeV/c, 153 MeV/c, and 210 MeV/c, with total particle fluxes of 10 MHz. We measure the beam particles RF time with a Scintillating Fiber detector at the intermediate focal point of the channel, where particles are momentum dispersed.

As the beam particles enter the M1 area, shown in Figure 4, they pass through a shielding wall intended to reduce the rate of secondaries from decays in flight incident upon the detectors. The beam RF times are again measured in a scintillating fiber array after the wall. The beam trajectories are determined in a set of three GEM chambers. Particles then pass into the vacuum chamber and a liquid hydrogen cryotarget, where they can scatter from liquid hydrogen, or from windows in the system. Particles largely do not scatter, and continue into a high-precision beam monitoring scintillator. Those that do scatter left or right pass into one of two identically designed detector systems, consisting of wire chambers to determine the scattered trajectory, and two planes of high-precision scintillators to trigger the DAQ and determine RF times and energy loss in the scintillators.

We want to emphasize at this point that all detector components and the target use *existing, often standard technologies.* The scintillating fiber arrays are reusing an existing detector. The GEM chambers are currently being used in the OLYMPUS experiment. Numerous hydrogen cryotargets exist; we plan on a new target based on systems used at Fermilab and Mainz. The scattered particle wire chambers are a copy of a system used at Jefferson Lab. The scattered particle scintillators are a copy of a new system developed for the Jefferson Lab 12-GeV upgrade. The novel feature of this experiment is assembling relatively modern high-rate detectors to measure a high-precision cross section in the PSI πM1 beam line.

B. Physics Reactions and Backgrounds

The desired reactions are ep and μp elastic scattering. The experiment must determine these cross sections precisely, while at the same time identifying and rejecting a number of background reactions higher in rate than the desired elastic scattering processes. The beam-induced background processes include the following:

- For incident μ's: scattering from the target end windows, decaying in flight, and knocking out δ's from the target. The rates for elastic muon scattering are shown in Figure 5, along with the projected statistical uncertainties for the experiment. For electrons the statistics are estimated be a few times better. The ratio of rates for elastic μ and e scattering from Carbon and Aluminum versus Hydrogen are shown in Figure 6, which illustrates the advantage of using a kapton target cell rather than an aluminum target cell. This background will need to be subtracted.

- For incident e's: scattering from the target end windows, and Moller and Bhabha scattering from atomic electrons. Positrons can also annihilate with atomic electrons. Both electrons and positrons radiate photons, to which we are insensitive, but the photons can knock electrons out of the target into the detectors.

- For incident π's: all processes are backgrounds. These include scattering from the LH_2 and target end windows, decaying in flight, and knocking out δ's. Charge exchange reactions are possible, and are of similar magnitude to the elastic and

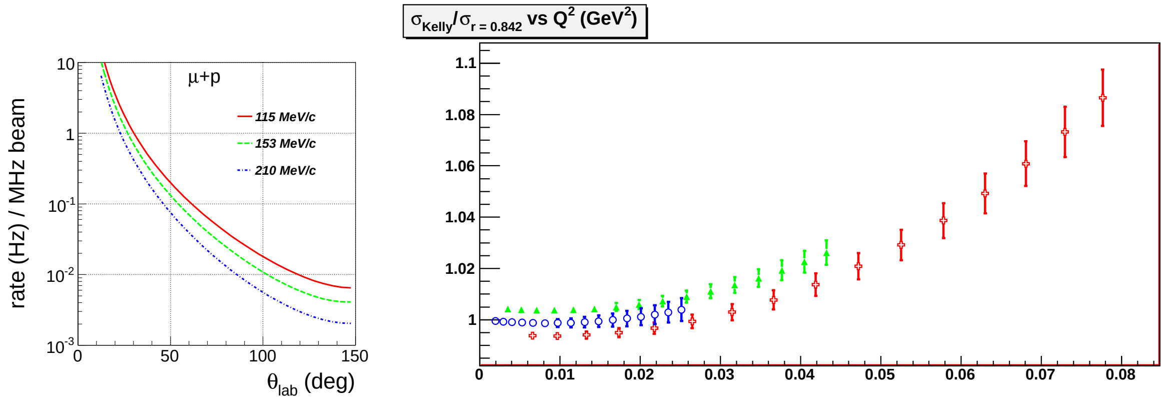

FIG. 5. (Left) Rates for elastic μ scattering from Hydrogen as a function of angle and beam energy. The thickness of the target was assumed to be 4 cm. Electron scattering distributions are very similarly shaped to the muon scattering distributions. (Right) Estimated statistical precision that will be obtained in this measurement for μ^+p, assuming the data follow the Kelly form factors. Data from the 3 different momentum settings are slightly offset for better viewability. Uncertainties for μ^-p are somewhat worse, whereas uncertainties for $e^{\pm}p$ are significantly better.

inelastic scattering, though the ensuing $\pi^0 \to \gamma\gamma$ decay generates two tens-of-MeV γ's to which our detectors are relatively insensitive.

In addition there are possible cosmic ray events and accidental coincidences, which we will consider later. We neglect the following beam-induced backgrounds, as their rates are small corrections to our background estimates.

- Quasifree scattering from the target end windows. Since the elastic scattering cross section is proportional to Z^2, it is about an order of magnitude larger, at low Q^2, than the quasifree scattering, which is proportional to Z. Thus, the quasifree scattering rate is small compared to the elastic rate.

- Electroproduction of π's. The 153 MeV/c setting is just above electroproduction threshold for the e beam, but the electroproduction cross section is small compared to the elastic scattering cross section.

- Elastic and quasifree π scattering from the target end windows. Since the cross section for strong-interaction processes on nuclei scales roughly as $A^{2/3}$, with an order of magnitude fewer nuclei in the end windows than in the liquid hydrogen the

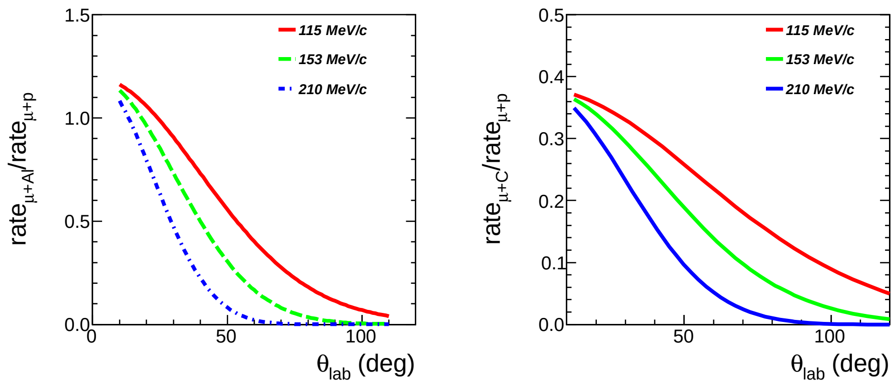

FIG. 6. Ratio of rates for elastic μ scattering for Carbon and Aluminum relative to Hydrogen as a function of angle and beam energy. The thicknesses of the materials were 250 μm for C, 200 μm for Al, and 4 cm for H. The nuclear form factors fall off faster with Q^2 as expected. The estimated rate for kapton is about 3 times smaller than for aluminum.

rates of π-induced processes on the end caps are a small correction to the rates of πp processes.

Background processes affect the experiment in several ways, leading to singles rates in the detectors which make it difficult to analyze events and leading to triggers (sometimes from accidental coincidences) limiting the read out of the elastic scattering events of interest. At the analysis level the background events if not sufficiently suppressed can be counted as elastic scattering events which affects the cross section determination.

TABLE I. Estimated flux of beam particles in MHz for a primary proton beam current of 2 mA, and the flux if the total for all particles is limited to 10 MHz.

Momentum (MeV/c)	115	153	210
μ^+	1	$2.5 \rightarrow 1.5$	$5 \rightarrow 0.62$
e^+	6	$7 \rightarrow 4.2$	$6 \rightarrow 0.74$
π^+	0.12	$7 \rightarrow 4.2$	$70 \rightarrow 8.64$
μ^-	0.2	0.5	$1 \rightarrow 0.5$
e^-	6	8	$7 \rightarrow 3.5$
π^-	0.023	1.4	$12 \rightarrow 6$

To estimate rates for processes we have to first know the beam fluxes. The π and e fluxes in the πM1 channel are well measured [38]. In Table I we give estimates for these fluxes at the chosen beam energies, based on figures of previous measurements, and also estimate the μ flux based on negative polarity RF time spectra at 270 MeV/c (1.3% of the beam is μ's) and positive polarity RF time spectra at 170 MeV/c (15% of the beam is μ's). The μ estimates are also based on a comment in [38] that the μ flux falls slower than the π flux as the energy decreases and an assumption that the μ/π ratio is the same for both polarities at each energy. The μ rates at 153 MeV/c are much more certain than the interpolation to 210 MeV/c or the extrapolations to 115 MeV/c.

We now present in Table II estimated singles and trigger rates for all processes at the three proposed beam momenta and for both beam polarities. The overall estimates summarize Geant4 simulation rates reported later in Table XII, which in principle include all processes – for π's and μ's, scattering from the target, decays in flight, and δ knockout, and for e^-'s (e^+'s) scattering from the target including Moller (Bhabha) scattering, and for e^+ annihilation. The reported singles rate is the integrated rate for all scintillator paddles in a wall. In many cases the rate is dominated by forward angle particles and the most forward scintillator has about half of the total rate quoted. For the π's, we also consider the efficiency of the beam PID at rejecting the π events; the efficiency factors are taken from Table V below.

In all cases the assumed target is 4 cm of LH_2, with 0.125 mm kapton entrance and exit windows. The simulation includes the shielding, target, and scattered particle scintillators shown in Figure 4. We have separately broken out the rate for the elastic scattering processes from the target and end windows, as trajectory reconstruction and RF time cuts should efficiently remove all other backgrounds. This was done as a standalone calculation.

The background rates were in some cases crosschecked with standalone estimates. For example, the rates for $\pi^{\pm}p$ scattering were also evaluated using cross sections from the SAID partial wave analysis, available online at `http://gwdac.phys.gwu.edu/`. The particle decays in flight were also approximately estimated, and agreed at about the 20% level with the more detailed Geant4 estimate.

TABLE II. Rates for both detector arms combined for various processes in Hz (or kHz) with the estimated beam fluxes totaling 10 MHz for all particle types. The "+" momenta indicate positive polarity particles, while the "-" momenta indicate negative polarity particles. For elastic processes from the target the singles and trigger rates are basically equal, but for particles from decays in flight or low energy particles knocked out of the target this is not the case. The rates are for both detector arms combined. The π-induced processes also take into consideration the reduction in rate from beam particle identification.

Momentum (MeV/c)	+115	+153	+210	-115	-153	-210
$\mu + p$ **elastic scattering**	**5.3**	**5.6**	**1.3**	**1.1**	**1.8**	**1.1**
μ+kapton elastic scattering	1.7	1.8	0.4	0.4	0.6	0.4
Geant4: μ singles	1600	1740	1080	320	560	940
Geant4: μ triggers	760	840	240	80	280	200
$e + p$ **elastic scattering**	**55**	**22**	**1.9**	**55**	**40**	**9**
e+kapton elastic scattering	18	7	0.6	18	13	3
Geant4: e singles	60k	42k	7.6k	64k	86k	38k
Geant4: e triggers	3k	2.2k	400	4k	5.2k	2.2k
Geant4: π singles	12k	280k	290k	2.2k	94k	200k
Geant4: π triggers	7k	220k	250k	1.4k	74k	176k
Geant4: π triggers + beam PID	0	22	76	0	8	52
Total singles rate	74k	324k	300k	66k	181k	239k
Total Geant4 triggers + beam PID	3760	3060	720	4080	5500	2450

The first point to note concerning the estimated rates is that no individual detector sees more than ≈160 kHz total rate in the individual detector systems. For the first plane of scintillators, with 17 paddles, the average rate in the paddles is then small, about 10 kHz, in the worst kinematics. For the first wire chamber the rate corresponds to 120 Hz/cm of wire, about 1% of the usual estimate for the gas physics limit, or about 5 kHz / wire. The forward most paddles and wires have the highest rates, and in the worst kinematics the forward-most paddles on each side will have about half the total rate in the scintillator hodoscope, or about 81 kHz, which is still quite moderately small. Similarly, the forward-most wire in the wire chamber will continue to have a modest rate, far below the gas physics limit and with nearly negligible probability of accidental coincidences – $P_{acc} \approx 15$ kHz $\times$ 100 ns = 0.15%.

From these estimates it is also apparent that the demands on the data acquisition system read out rate are large, but not very large. The work of much of the collaboration is centered at Jefferson Lab, where the CODA DAQ system is able to handle rates of the magnitude quoted in Table II with around 20% dead times, depending on the particular system. The more up to date systems with buffered electronics and faster conversion times have smaller dead times. Here we plan to decrease the demands on the DAQ system with two easily implemented techniques. First, a dual DAQ system would use two separate systems reading out the two detector arms, doubling the rate capability. Second, as the electron rate is generally much higher than the muon rate, we can prescale down the electron triggers and still have excellent statistics with no significant increase in systematics. Related to this, one can see from Table XII that much of the background rate for all incident particles is concentrated in the most forward angles. As a result, an alternate way to prescale the data exists, and that is to prescale events that strike the forward scintillator bars. Finally, much of the electron rate results from scattering from upstream of the target with low-energy forward going Mollers and Bhabhas. These events can be suppressed with relatively thin shielding just before the target and after the last GEM, or by raising the threshold on the rear plane of scintillators. We are continuing to study these options.

TABLE III. Top: Accidental trigger rates in Hz for π-induced processes to be randomly coincident with e or μ beam particles. Bottom: The probability that there is a beam π when there is a beam μ- or e-induced event. Both estimates assume beam fluxes totaling 10 MHz for all particle types. The "+" momenta indicate positive polarity particles, while the "-" momenta indicate negative polarity particles.

Momentum (MeV/c)	+115	+153	+210	-115	-153	-210
% of pulses with e's or μ's	14.0	11.3	2.7	12.4	16.8	8.0
Geant4: π triggers	7 kHz	220 kHz	250 kHz	1.4 kHz	74 kHz	176 kHz
Accidental coincidence rate	1 kHz	25 kHz	7 kHz	170 Hz	12 kHz	14 kHz
fraction of beam pulses with π's	0.24%	8.8%	17.3%	0.05%	2.8%	12%

Finally we need to consider the subject of accidentals. Generally we want to trigger the DAQ whenever there is a beam e- or μ-induced event from the target. We do not want to trigger on a beam π-induced event. But the total rate of e and μ beam particles, assuming

10 MHz total rates, ranges from 1.36 $\rightarrow$ 8.5 MHz, or, as there is 50 MHz beam, about 2.7% $\rightarrow$ 17% of the time there is a π-induced event it will be randomly coincident with an e or μ beam particle. The same consideration applies to cosmic rays. The estimated accidental trigger rates for π-induced events – elastic scattering and decays in flight – are shown in Table III. The accidental coincidences of π-induced events with e or μ beam particles lead to rates that are generally too large to be read out, except at -115 MeV/c, and if allowed will lead to large dead times. The solution to this is to use the beam PID system to identify pions and use the pion ID signal as a veto – if there are π's in the same RF bucket as an e or μ, the event will not be read out. The FPGA PID system is estimated to generally be $> 99\%$ efficient at identifying particles, so in the worst case at +153 MeV/c, the 25 kHz accidental rate will only be reduced to about 250 Hz.

Table III also shows the probability that there is an accidentally coincident beam π with a μ or e induced event, The probability ranges from 0.05% up to 17.3%. Thus, in the worst case at +210 MeV/c the statistics decrease by 17.3% and the statistical uncertainty only increases 8.7% (relative) from vetoing events with beam π's also present. We conclude that vetoing triggers when there is a beam π significantly reduces the random coincidence and readout rates while having little impact on the statistical precision of the experiment.

C. Overview of Equipment

Our intent is to measure accurate high-statistics cross sections for μp and ep elastic scattering. To our knowledge, no one has measured precise cross sections with a 4π spectrometer. The basic problem is knowing precisely the scattering kinematics. Most 4π spectrometers that detect particles have a solenoidal or toroidal field configuration, and knowledge of the field and the positioning of the detectors limits cross sections. The most precise scattering cross sections to date have been measured with small acceptance spectrometers. However, the low flux of the μ beam does not allow a statistically precise cross section to be measured in a reasonable time with a small acceptance spectrometer. Finally, given the beam properties and the lack of inelastic processes, a magnetic spectrometer does not appear to significantly improve our ability to subtract, e.g., target cell wall or other backgrounds. Thus, we propose here to measure cross sections with a non-magnetic spectrometer covering a good fraction of 4π, to enable adequate statistics and kinematic reconstructions in the experiment.

Experiment features include the following:

- The experiment is planned for the πM1 beam line, which to our knowledge has not previously been used for such an experiment, and for which the μ beam properties are not well understood. We will commence a series of measurements to determine the μ beam properties.

- The beam momentum must be known at the 0.1% level. While this can be done directly for the π beam using the dispersion at the intermediate focal point DR8, the validity of this technique for the μ beam has not, to our knowledge, been established. We will describe how the beam energy, and the spectrum after energy loss in the detectors, can be directly determined using time-of-flight techniques, to better than 0.1% at low beam momentum.

- The μ flux is not well known. We will describe how we plan to determine the μ flux in test measurements in fall 2012 for planning purposes, and how we will determine the μ and e flux by counting the beam particles during the experiment.

- The rates of particles in the detector from decays in flight are moderately large, such that accidental coincidences with beam e's or μ's is a potential problem. We plan to significantly suppress these backgrounds by shielding the beam line.

- The scattering angle must be precisely determined. We will describe how we plan to use GEM chambers to measure beam particles and conventional wire chambers to measure scattered particle trajectories, and how we plan to align the chambers to a precision of $\approx$0.5 mr, so that angle resolution is limited essentially by multiple scattering.

- The efficiency of the scattered particle detectors must be determined. We will describe both the detection efficiencies and dead times for the detectors, and the tracking efficiency for the wire chambers.

- The data acquisition system live time must be determined. We will describe the common techniques we will use to determine the system live time.

- The target thickness must be precisely known. Target thickness is one of the largest absolute uncertainties, but with the design of the experiment – measuring both *ep* and μp scattering at all angles at the same time – it becomes a small relative uncertainty.

D. Analysis and Corrections

Once the data are taken, the analysis must be performed. Event data are analyzed to determine yields. Various corrections are needed to determine cross sections. Some corrections (e.g., efficiencies) result mostly from the data while others (e.g., Coulomb corrections) are of a more theoretical nature. The form factors and the proton radius result from fits to the cross sections. Systematic uncertainties need to be evaluated.

The analysis procedures are fairly standard for a scattering experiment. For scintillator elements, pulse heights and times are determined. For chamber elements, wires hit and drift times are determined, and are used to generate tracks. The incoming and outgoing tracks are used to construct scattering angle and target variables. These values in addition to the timing are used to determine the type of the incident particle and the kinematics of the scattering event. After cuts are applied, we have a number of scattering events of interest, and target data minus empty target data give a net number of counts which, after being corrected for various efficiencies, are used to generate the scattering cross sections. The above outline focuses on the event data. Analysis is also needed of slow controls and scaler data are needed for the cross sections as well. For example, the slow controls data are used to determine the target thickness, and scaler data are used to determine the incident flux. Detector efficiencies are largely determined through studies of the event data.

Once the raw cross sections are determined, various corrections are needed. These include Coulomb corrections, and radiative corrections, including two-photon corrections.

The primary goals of the measurement are an extraction of the proton radius, which depends on the Q^2-dependence of the data, and the comparison of $e^{\pm}$-p and $\mu^{\pm}$-p cross sections. For the extraction of the radius, only those uncertainties which yield a Q^2 dependence enter into the extraction, while for comparison of electron and muon (or positive and negative leptons), systematics which are independent of the lepton beam (e.g. target thickness, detector offsets, etc...) largely or completely cancel. Thus, the relative systematic uncertainties that go into the proton radius extraction are estimated to be ≈0.5%, with some additional cancellation in the comparison of the radius as extracted from electron or muon scattering, or in the direct comparison of the electron and muon scattering cross sections. In addition, combining the data from positive and negative leptons allows for an extraction where the charge-dependent radiative corrections (Coulomb corrections, hard two-photon exchange effects, and lepton/proton bremsstrahlung interference terms) cancel, allowing for a comparison of the measurements and extraction of the radius free of this significant correction [39, 40, 41, 42].

The extraction of the radius from the cross section introduces additional systematic or model-dependent uncertainties. An extraction of the radius using the higher beam momentum settings yields an uncertainty in the extracted radius of ≈0.0140 fm for muon scattering, corresponding to a 1.6% measurement of the radius, with the statistics and experimental systematic uncertainties dominating the total uncertainty. This estimate accounts for the statistical and systematic uncertainty, including the correction for backgrounds from scattering in the target window. The fit includes normalization factors for the different beam momentum settings, so that the uncertainty associated with the knowledge of the normalization is propagated into the fit, and also includes an estimate of the error made when fitting to a second-order polynomial.

Taking only the lowest beam momentum setting, the Q^2 range is such that a linear fit is sufficient to extract the radius, which yields an uncertainty of 0.015 fm, yielding a largely independent extraction where the uncertainty is dominated by the uncertainty associated with the linear truncation. This uncertainty is difficult to estimate precisely, but we take a conservative approach assuming a simple linear fit in Q^2, rather than a first order expansion with a better physics motivation (e.g. a dipole form [43] or continued fraction [2] expansion). The combined uncertainty based on these two extractions should be close to 1% for the μ^+ and μ^- measurements, and somewhat better for e^+ and e^- due to the improved statistical precision.

The uncertainty on the absolute extraction of the proton radius is comparable to previous measurements, but not better. However, we have the unique capability to compare electron and positron (or μ^- and μ^+) scattering to directly examine the impact of two-photon exchange effects in both cases, as well as making a direct comparison of the electron and muon scattering results. In this case, we have essentially identical Q^2 coverage and relative precision for the electron and muon data, and thus the error associated with the choice of fit function in the extraction will be identical and cancel in the comparison. In addition, several sources of systematic uncertainty will at least partially cancel in comparing the different data sets, in particular for the comparison of like-sign electron and muon measurements which are made at the same time. Therefore, in the comparison of different radius extractions, the relative uncertainties are below 0.005 fm, compared to the $\approx$0.015 fm uncertainty on the absolute measurement, allowing for extremely precise comparison of the different measurements.

III. THE πM1 BEAM LINE

In this section we briefly review properties and simulations of the π beam, and discuss estimates for the μ beam. The πM1 channel views the M production target at an angle of 22°. The channel includes a number of focusing quads, two dipoles which each bend the beam 75°, two sets of jaws (FS11 to reduce the flux, FS12 to limit the momentum range in the dispersed beam tune), and a no-longer-functioning electrostatic separator.

The default tune is point-to-point, producing an image of the production target at a distance of about 24 m. The tune also has a dispersed beam at the intermediate focal point, at a distance of $\approx$12 m from the production target, with a dispersion of 7 cm/% and a resolution of 0.1%.

The πM1 channel fluxes, measured by Schumacher and Sennhauser in 1987 [38], are shown in Figure 7. Fluxes for and properties of the μ's coming through the channel are not as well established, as discussed with our estimates in Section II B. We do not attempt to estimate the actual fluxes or the ratio of the μ flux to the π flux from simulations of physics at the production target. To do so requires an accurate physics model of production processes at the M target. Instead, in this section we discuss the results of a TURTLE simulation intended to investigate the widths and angular divergences of the beam. The simulation used a smooth distribution of π's thrown roughly in the direction of the πM1 channel, and of μ's resulting from decays of these π's.

Because π's and μ's are unstable particles, they continuously decay producing a beam halo of μ's and e's, respectively. For our range of momenta the decay rates are of order 10%/m for π's and 0.1%/m for μ's. The desired muon beam then consists of 2 components, one component being μ's produced in the region of the M production target, which as a beam have properties presumably similar to those of the π beam, and the second component being μ's produced from π decays in flight generally within or after the πM1 channel. Similarly, the electron beam has a (relatively small) component from the decays of muons. Figure 8 shows that the π decays produce μ's at forward angles, leading to an unwanted background that is generated at minimum 0.5 m upstream of the target (see Table XIII). Figure 9 shows that the μ decays produce e's over a wide range of angles, due to the 3-body nature of the decay. However, there is a much smaller absolute rate of μ decays.

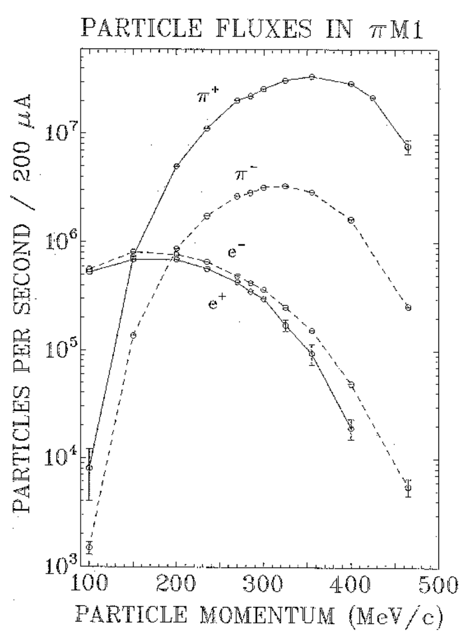

FIG. 7. Fluxes of e's and π's in the πM1 channel for a 200 μA proton beam incident on a 2 mm thick carbon production target. The measurements used a 3 cm × 4 cm scintillator 4 mm thick. The figure is taken from the report by Schumacher and Sennhauser.

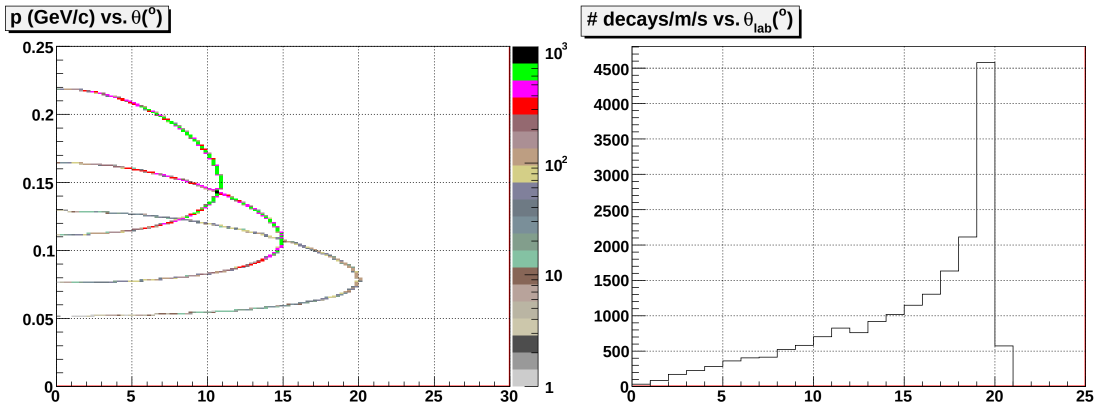

FIG. 8. (Left) Simulation of π decays in flight showing μ momentum vs. angle for the three selected beam momenta. (Right) Simulation showing the angular distribution of muons from the decay in flight of 115 MeV/c pions.

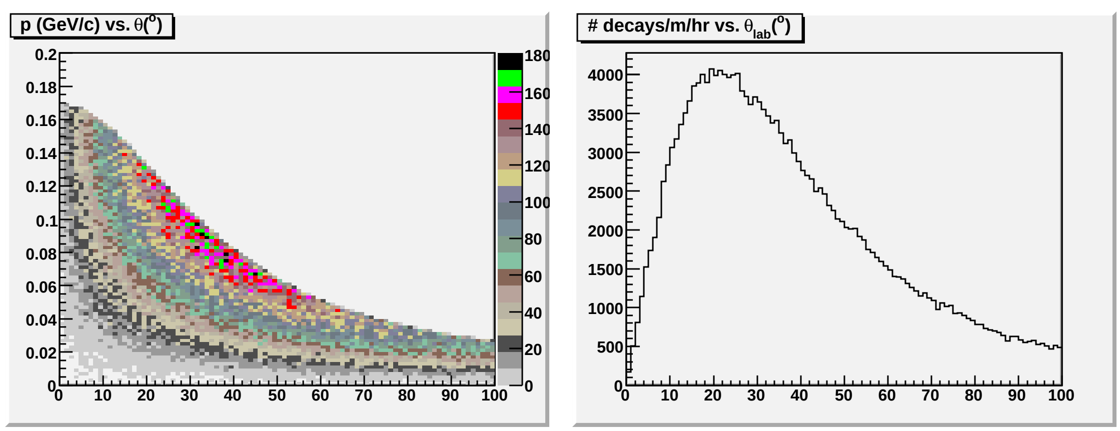

FIG. 9. (Left) Simulation of e momentum vs. angle for μ decays in flight for a muon momentum of 153 MeV/c. (Right) Simulation showing the angular distribution of electrons from the decay in flight of 153 MeV/c pions. The distribution shifts slightly to smaller or larger angles if the muons are polarized.

A. Beam Line Simulations

A summary of the properties of the π beam for a standard beam tune is shown in Figure 10. The dispersion of the beam at the intermediate focus and the few cm size of the beam spot at the target can be seen.

We have studied the distribution of all μ's reaching the target region using TURTLE.

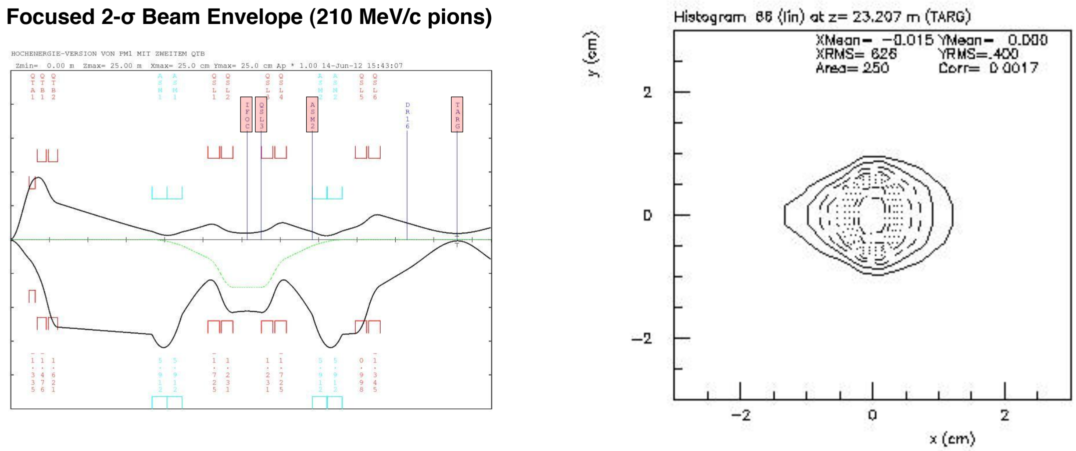

FIG. 10. TURTLE simulations of the πM1 π beam. (Left) The beam envelope. The top part of the figure is the vertical or y direction. The bottom part of the figure is the horizontal or x or dispersion direction. Tick marks indicate 10 cm in the vertical direction and 2 m in the horizontal direction. The dispersion of the beam at the intermediate focal point ("IFOC") can be seen. (Right) The beam spot at the target position. The outer solid curve indicates the 2σ limits. Because the beam cuts off sharply in the y direction, the full width is also about ±1 cm, whereas in the x direction small tails of the beam reach to $\approx\pm2.5$ cm – about 0.5% of π's are outside the central ±2 cm.

While the distribution is broad in position, angle, and momentum at the target, it appears that almost all the widths are due to the decay of π's within the last few meters of the beam line before the target. Figure 11 shows the TURTLE simulations of π's and μ's *from the production target only* at the scattering target position. In x, the μ distribution appears broadly similar to the π distribution, with both a few cm wide at the target in both x and y directions. The tail in the x distribution appears to be correlated to a tail in the x' distribution (not shown) to $+x'$ and to tails in the momentum distribution. It *appears*, based on simulations with and without channel apertures, that the satellite peak results from events passing into unphysical regions of the modeled magnetic field that would in reality be removed by apertures in the channel. The divergence of the μ's in the target region (not shown) is also similar to the divergence of the π's. The differences we see here between π and μ distributions will need to be confirmed with beam line measurements.

Figure 12 shows the TURTLE simulations of π's and μ's *from the production target only* at the intermediate focal point. Here the x distributions of π's and μ's are similar,

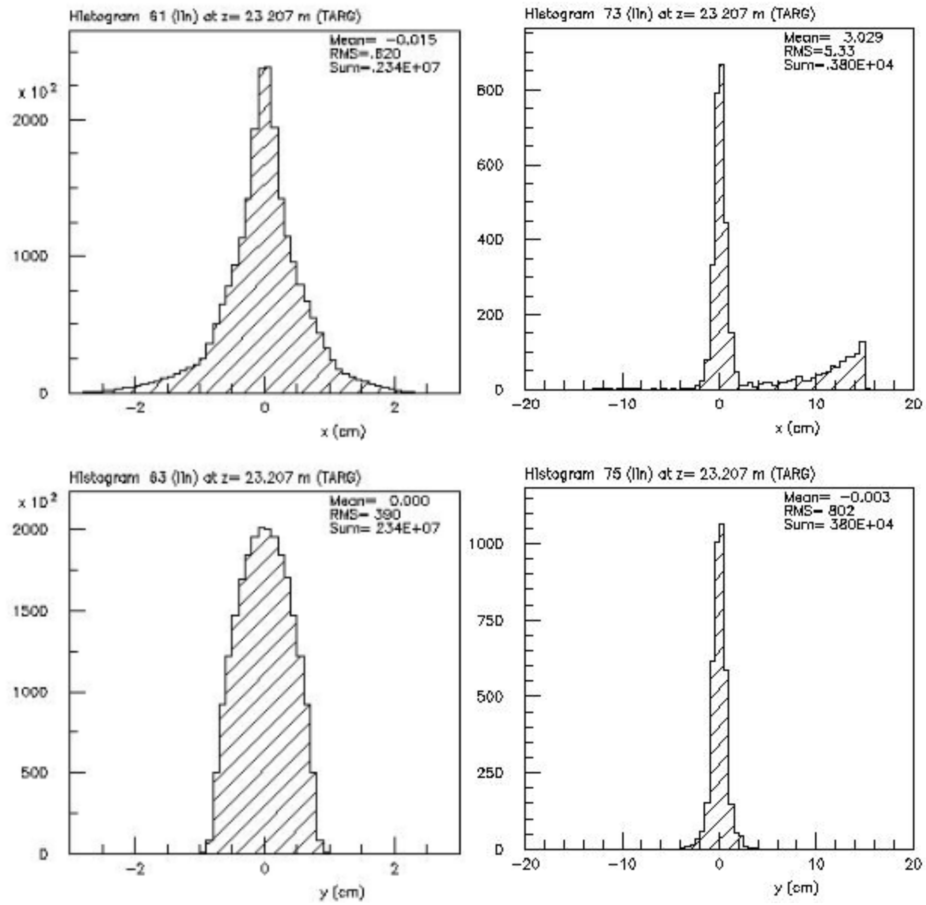

FIG. 11. Simulation of the distributions at the scattering target of pions (left) and muons (right) that come from the production target. Note that the horizontal scales are about a factor of 10 different. While the statistics are poor, the distributions seem to be generally similar, except for the tail in the x distribution. The y distribution of μ's is about twice the size of the y distribution of π's.

but the μ y distribution is much broader. For the angle divergences (not shown), the μ x' distribution is, like the x distribution, slightly wider, ≈30 mr vs 25 mr. But the μ y' distribution is, like the y distribution, about 6x wider, ≈100 mr vs 15 mr. While the distributions at the IFP are much broader in y and y', the significantly greater number of μ's in the IFP spectra as compared to the target spectra suggests that apertures in the beam line remove the μ's that are outside the π distribution phase space. This tentative conclusion will need to be verified with measurements. These observations suggest that the x position at the IFP remains a good measure of the beam momentum, for μ's that

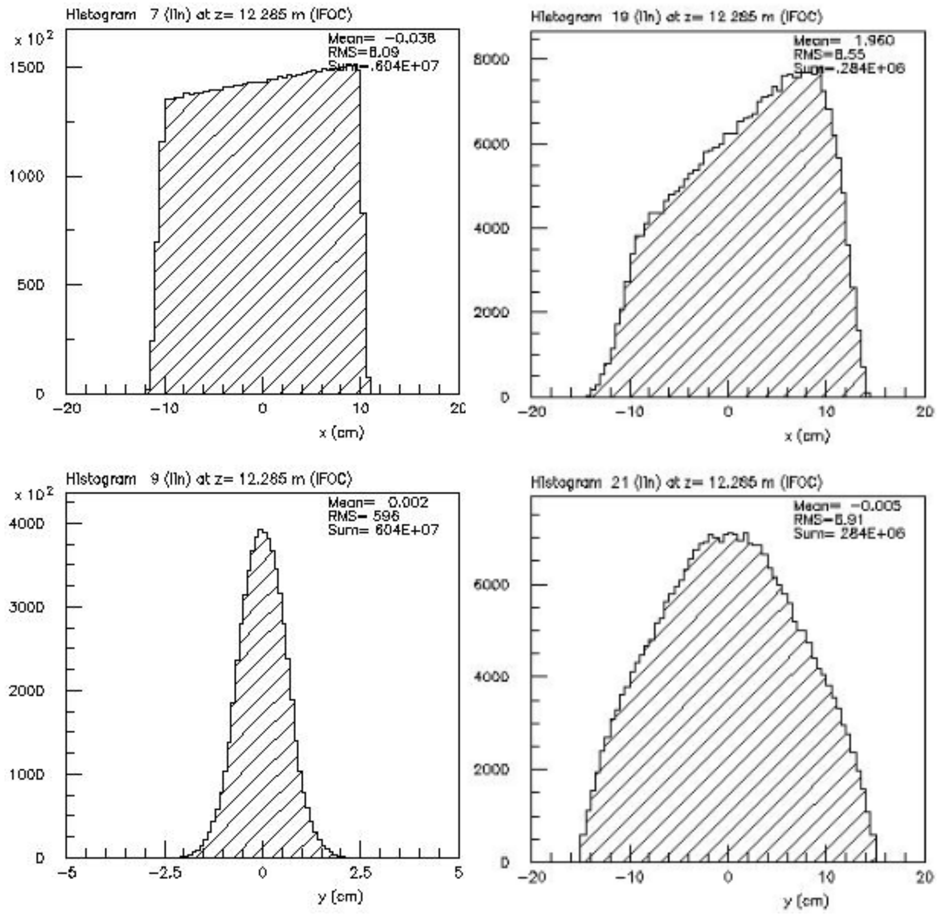

FIG. 12. Simulation of the distributions at the intermediate focal point of pions (left) and muons (right) that come from the production target. Note that the horizontal scales for the y distributions are a factor of 4 different. While the x distribution are basically similar, with the μ spectrum less sharply cut off, the y distribution for the μ's is several times wider.

reach the scattering target, but at this point it is not clear if the resolution remains at the 0.1% level or is a few times worse. Again, measurements will be needed to determine the resolution. These measurements are discussed in Section V.

B. Beam Line Shielding

A sample spectrum demonstrating the benefit of beam line shielding is shown in Figure 13. The absolute scale in the figure is not important, but the relative scale between the curves is based on the estimated flux for positive polarity particles given in Table I. With

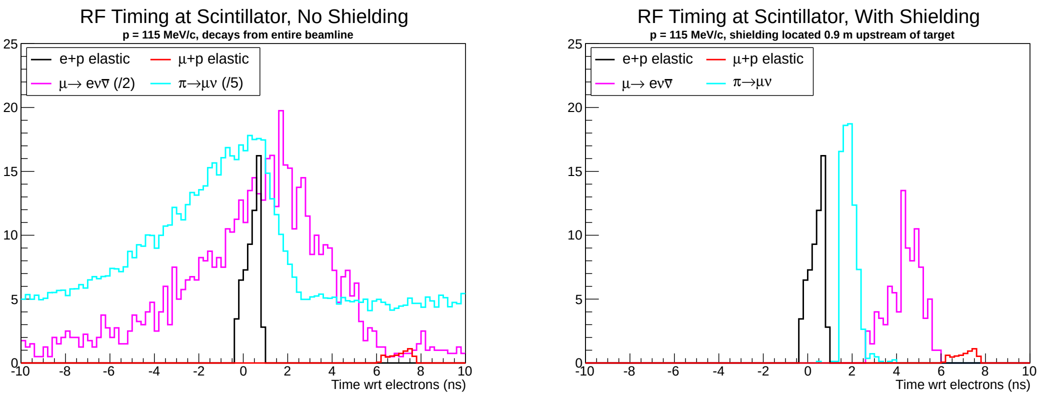

FIG. 13. GEANT simulation of the RF time spectrum for positive polarity particles at the scintillators with 115 MeV/c beam momentum without shielding (left) and with beam line shielding (right). In the left panel, the counts from $\mu \to e\nu\bar{\nu}$ decays and $\pi \to \mu\nu$ decays are scaled down by a factor of 2 and 5, respectively. These are raw RF time spectra, which do not account for reductions in the π-induced events from beam PID cuts, from removal of events that do not track back to the target, or from flight path corrections.

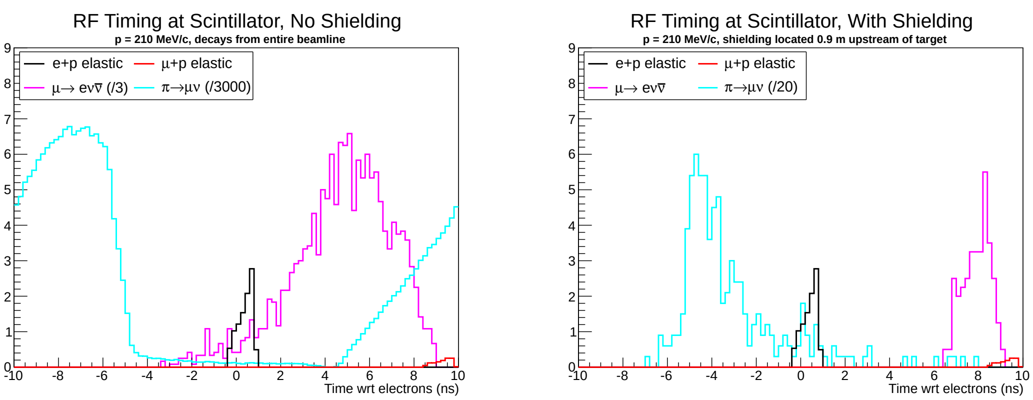

FIG. 14. GEANT simulation of the RF time spectrum for negative polarity particles at the scintillators with 210 MeV/c beam momentum without shielding (left) and with beam line shielding (right). In the left panel, the counts from $\mu \to e\nu\bar{\nu}$ decays and $\pi \to \mu\nu$ decays are scaled down by a factor of 3 and 3000, respectively, while in the right panel the $\pi \to \mu\nu$ decays are scaled down by a factor of 20. These are raw RF time spectra, which do not account for reductions in the π-induced events from beam PID cuts, from removal of events that do not track back to the target, or from flight path corrections.

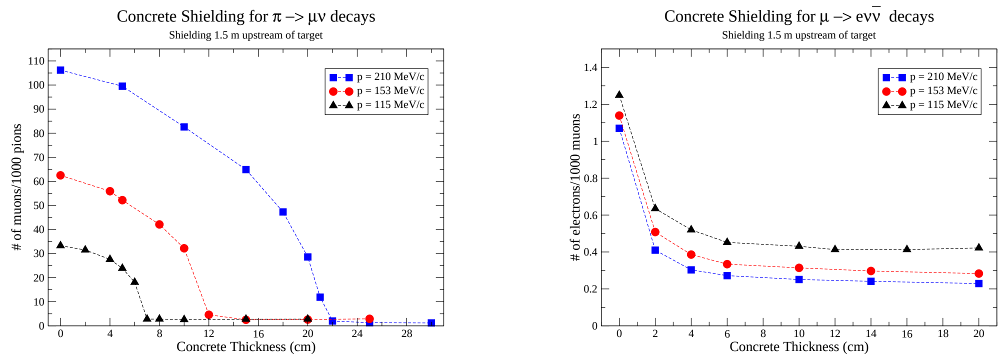

FIG. 15. GEANT simulation of the reduction in the number of muons from π decay (left) and electrons from μ decay (right) as a function of the thickness of concrete shielding. The shielding is oriented perpendicular to the beam, and the $\cos\theta$ increase in the thickness of concrete is included.

the addition of 50 cm of concrete shielding around the beam pipe located 0.9 m upstream of the target (right panel), the tails of the μ and π decay spectra are significantly reduced. At 115 MeV/c, there is essentially no overlap of muons from π decay in the ep elastic signal or electrons from μ decay in the μp elastic signal. The event rate at the scintillators is reduced by a factor of 50 for π decays and a factor of 5 for μ decays. The trigger rates will be much lower when RF timing for PID is considered, but these reductions help reduce the demand on the detector system.

Figure 14 shows the RF timing peaks for 210 MeV/c without and with beam line shielding, where the estimated flux for negative polarity particles is used for relative weighting. At 210 MeV/c the RF timing peaks are better separated, however there is a very large flux of π and μ decays hitting the scintillator which lead to tails overlapping the desired elastic signals. The event rates are reduced with the addition of shielding by a factor of 400 for π decays and a factor of 6 for μ decays. Again, these event rates will be highly suppressed at the trigger level from RF timing. The remaining events can be removed at the analysis level by the additional requirement that the particle track projects back to the target.

The simulations used a shielding wall that is 50 cm thick and located with its end 0.9 m upstream of the target. This thickness is based on readily available shielding at PSI and is much thicker than what is actually needed. A calculation of the thickness needed for the beam line shielding is shown in Figure 15 for π decays (left) and μ decays (right).[3] The scale is not weighted for the flux of each particle momentum, but rather shows the number of decay events that hit the scintillator per incoming particle. In all cases, the thickness of shielding required is well below the 50 cm thick concrete that is available for use.

Thus, the use of a 50 cm thick shielding wall before the target significantly reduces experimental backgrounds. As engineering designs develop we will study whether it is possible and beneficial in practice to add additional shielding to the sides of the GEM chambers to further reduce backgrounds from particle decays in flight.

IV. BEAM PID AND COUNTING SYSTEM

The beam particle identification (PID) counting system consists of the following:

- a scintillating fiber detector at the intermediate focal point, DR8, about 12.2 m from the π production target. The scintillating fiber detectors mentioned in this section are described further in Section VI. The detector, to be discussed in more detail later, consists of two offset planes each with 110 2-mm fibers.

- a scintillating fiber detector just upstream of the target. In the simulations shown below, this detector is assumed to be a 23.5 m flight path from the π production target. This detector consists of 3 planes of 2-mm fibers in XYU orientation, with an active area of about 3 cm $\times$ 3 cm.

- a set of custom FPGA boards. These boards have inputs from the SciFi fibers and the beam RF signal. They determine an RF time for each hit and output a μ, e, or π signal, on separate channels, or no signal.

- additional logic, which we expect to set up in a commercial CAEN v1495 VME board. If the FPGAs identify for both SciFi detectors μ or e or π RF times, the corresponding coincidence signal is sent to scalers to be counted and to the data

[3] In these simulations the shield wall was 1.5 m upstream of the target, but the conclusions are the same.

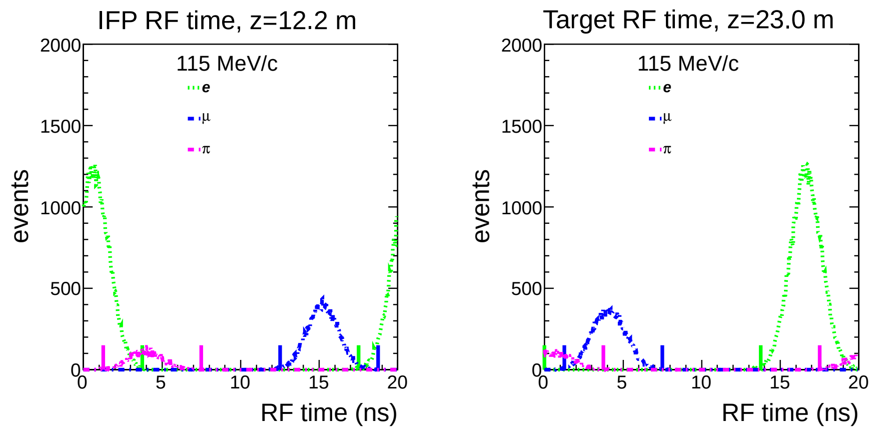

FIG. 16. RF time distributions at the intermediate focal point (left) and target (right) for 115 MeV/c beam momentum, assuming 1 ns resolution in the beam scintillators. The absolute number of counts is arbitrary, but the relative number of counts for each particle type is based on estimates for positive polarity particles in the proposal. The μ peak overlaps the e peak at the IFP but the π peak at the target. The e peak overlaps the π and μ peaks at the IFP but only the π peak at the target. The short vertical lines indicate cuts used to quantify PID performance, described in the text.

acquisition system for use in event data, and to the trigger system for further processing. Accidental coincidence signals will also be generated and sent to scalers for counting.

The system identifies particles through timing techniques. It is intended to count the beam particles so that the cross sections may be precisely normalized, and to identify the type of beam particle responsible for any scattering event, so that π-induced events, which are not the intent of this measurement, can be suppressed. In this section we will demonstrate how the system provides a high efficiency for identifying particles, and a low probability for misidentifying particles, at the hardware level.

A. Identifying and Counting Particles through Timing Differences

The ability of the system to identify beam particle types is examined in Figures 16, 17, 18, which were generated assuming that the beam scintillators have 1 ns time resolution

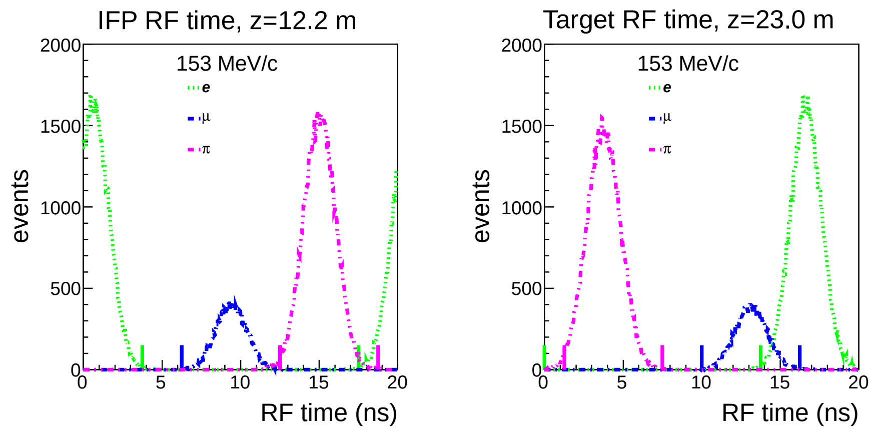

FIG. 17. RF time distributions at the intermediate focal point (left) and target (right) for 153 MeV/c beam momentum, assuming 1 ns resolution in the beam scintillators. The absolute number of counts is arbitrary, but the relative number of counts for each particle type is based on estimates for positive polarity particles in the proposal. The μ peak overlaps the π peak at the IFP but the e peak at the target. The e peak overlaps the π peak at the IFP but the μ peak at the target. The short vertical lines indicate cuts used to quantify PID performance, described in the text.

(σ) in hardware, and the channel is set to the full 3% momentum bite. For each of the proposed beam energies, it can be seen that the RF time peaks for the particles are generally well separated, overlapping only in the tails, so that the combination of the RF times from the two detectors can efficiently identify the beam particle type in hardware. Determining whether a particle is in the e, μ, or π RF time peak in hardware with conventional NIM electronics is likely prohibitively difficult. We are instead designing an FPGA based particle identification system that has the beam RF time signal and beam scintillator signals as inputs. The design work will be done by Ed Bartz, of the Physics electronics shop at Rutgers University, who is an experienced designer of FPGA and other systems who has worked with us on a number of projects. Ed is currently working mostly with the Rutgers high energy group on LHC projects, on which he has collaborated with PSI personnel. We currently expect that the LHC work will require Ed's time until fall 2012, at which point he can start design of the system discussed here. Our tentative plan for the system has 10 32-channel FPGA boards.

The FPGAs will subdivide the ≈20 ns RF period into 16 1.25-ns bins. The FPGA will

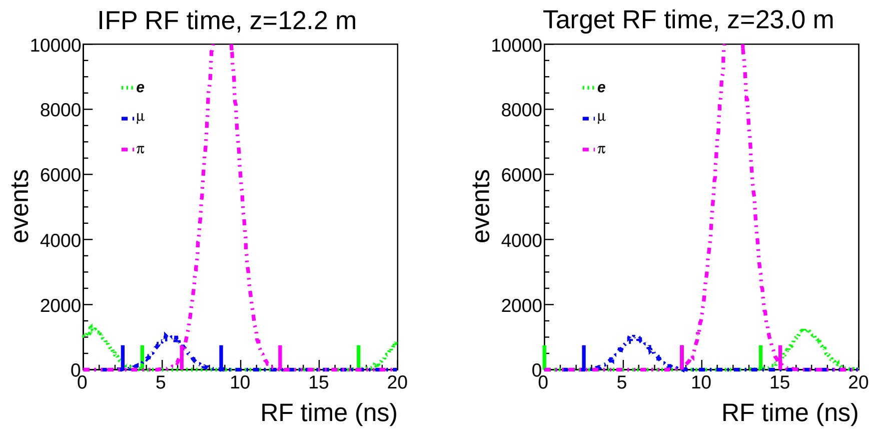

FIG. 18. RF time distributions at the intermediate focal point (left) and target (right) for 210 MeV/c beam momentum, assuming 1 ns resolution in the beam scintillators. The absolute number of counts is arbitrary, but the relative number of counts for each particle type is based on estimates for positive polarity particles in the proposal. The μ peak overlaps both e and π peaks at the IFP but neither peak at the target. The e peak overlaps the μ peak at the IFP but the π peak at the target. The short vertical lines indicate cuts used to quantify PID performance, described in the text.

be programmable, so that a signal appearing in a particular bin might lead to an e or μ or π output, or no output at all – since the tails of the timing peaks can overlap, an input signal can lead to more than one type of output signal. Each FPGA board will OR together the separate particle type signals from all channels on the board and output the resulting e, μ, and π signals.

We will then OR together separately the e, μ, and π outputs of all modules for a given detector, and AND together the DR8 and target detectors to determine if there is an e or μ or π passing through both SciFi detectors. These signals are sent to scalers for counting and to the data acquisition trigger logic. In addition to sending the final e or μ and π signals to the scalers, we also plan to send these signals on an individual plane basis, and also to send the combinations e AND μ, e AND π, and μ AND π to identify accidental coincidences of different particle types. The planned system does not allow us to identify accidental coincidences of the same particle type whose signals are processed by the same FPGA board.

TABLE IV. Probability of identifying a particle as given type from RF time measured at a single beam SciFi detector.

Momentum (MeV/c)	Detector	Particle Type	Fraction e ID	Fraction μ ID	Fraction π ID
115	IFP	e	0.9983	0.0245	0.2780
115	IFP	μ	0.0135	0.9959	0.0000
115	IFP	π	0.4227	0.0000	0.9948
115	target	e	0.9978	0.0000	0.2028
115	target	μ	0.0001	0.9955	0.3666
115	target	π	0.3112	0.2892	0.9917
153	IFP	e	0.9983	0.0000	0.0248
153	IFP	μ	0.0000	0.9978	0.0017
153	IFP	π	0.0084	0.0063	0.9936
153	target	e	0.9977	0.3359	0.0000
153	target	μ	0.2896	0.9970	0.0000
153	target	π	0.0001	0.0000	0.9904
210	IFP	e	0.9982	0.0324	0.0000
210	IFP	μ	0.0379	0.9980	0.2339
210	IFP	π	0.0000	0.4683	0.9943
210	target	e	0.9975	0.0000	0.0480
210	target	μ	0.0000	0.9976	0.0020
210	target	π	0.0500	0.0007	0.9972

We have investigated the efficiency of the system with a simple algorithm. We use a simple 5 bin window = 6.25 ns wide region for identifying the particle types - slightly wider than 6σ. The centroid of the peak determined the central bin of the window, with two bins added on each side. The simulation simply aligns the 20-ns RF window to the start of the flight of the particles from the production target, although in practice the phase of the RF time is basically arbitrary, due to variations in cable lengths into the electronics. Results are shown in Table IV. The "diagonal" elements should be roughly unity, while the off-diagonal elements (e.g., the fraction of μ's identified as e's and the fraction of e's identified as μ's) should be roughly symmetric – but not exactly since the peaks are not equally centered in the bins. The probabilities do not have to add to unity in each row, since a signal in some time bins leads to two different particle types being identified.

TABLE V. RF timing identification system estimated efficiencies. The misidentification of π's as e's at 115 MeV/c needs to be corrected, as discussed in the text.

Momentum (MeV/c)	115	153	210
e efficiency (%)	99.61	99.60	99.57
μ efficiency (%)	99.13	99.47	99.56
π's IDed as e's (%)	13.15	$\approx 10^{-4}$	$\approx$0
π's IDed as μ's (%)	$\approx$0	$\approx$0	0.03
e's IDed as μ's (%)	$\approx$0	$\approx$0	$\approx$0
μ's IDed as e's (%)	$\approx 10^{-4}$	$\approx$0	$\approx$0

TABLE VI. RF timing identification system estimated efficiencies with 50 ps offset. The misidentification of π's as e's at 115 MeV/c needs to be corrected, as discussed in the text.

Momentum (MeV/c)	115	153	210
e efficiency (%)	99.62	99.62	99.60
μ efficiency (%)	99.16	99.44	99.53
π's IDed as e's (%)	11.65	$\approx 10^{-4}$	$\approx$0
π's IDed as μ's (%)	$\approx$0	$\approx$0	0.03
e's IDed as μ's (%)	$\approx$0	$\approx$0	$\approx$0
μ's IDed as e's (%)	$\approx$0	$\approx$0	$\approx$0

Combining the results of two planes of detectors shown in Table IV gives us overall system efficiency estimates shown in Table V. In terms of the trigger and scalers, we only lose a few tenths of a percent in count rate due to inefficiencies, which is not a problem. The probability for misidentifying particles is small, except for π's being misidentified as e's at 115 MeV/c. This large probability of misidentifying π's as e's is not as troubling as it might at first seem to be. The most important reason is that at 115 MeV/c the π time of flight from the IFP to the target SciFi is 21 ns longer than the e time of flight. Thus, a π overlaps with the electron RF time from one RF bucket at the IFP and from the subsequent RF bucket at the target. When the coincidence is formed between the e signals from the two detectors, the π even if in the e RF time in each will not be in coincident e buckets, and will not be identified as an electron. Thus, the one significant misidentification number, of π's as e's, of order 10% from the overlap of Rf time misidentification probabilities, will become 0 in practice from the time of flight.

One concern is the stability of the beam RF time. There is some indication that the beam RF time is very stable when the machine runs, but can shift by up to 100 ps when the machine goes down and is brought back up. To study this issue we recalculated the efficiencies with the same algorithm but assuming the beam RF time is shifted 50 ps. Table VI shows the results. The efficiencies of identifying e's and μ's is stable to better than 0.1%, and the misidentification probabilities remain small.

As indicated before, it is important that the μ and e efficiencies are high to not lose statistics, but the cross section is not affected by an inefficiency here. The misidentifications are more important. Misidentification of beam particles leads to incorrect scaler counts and mis-normalization of cross sections. For μ's, the worst background is at 210 MeV/c, where the π/μ ratio is $\approx$14. The μ count will then be off by about 0.4% due to misidentified π's if the correction is not determined and applied. A second possible issue is whether the trigger rate has a large increase; it does not as as discussed in Section II A in relation to Table II for event rates and in relation to Table III for accidental coincidence rates. A third possible issue is whether misidentified, e.g., elastic πp events that are read out could affect the cross section, but due to the superior time resolution of the scattered particle scintillators in the analysis, these events are rejected.

Thus, the beam RF time ID system provides a sufficient suppression of π events at the trigger level to keep their readout rate small and the normalization accurate, once it is calibrated – the calibration procedure is discussed further below in Section IV B.

The numerical results presented here represent, in our view, a conservative estimate of the system performance. Several factors that might improve the actual experimental performance are the following:

- The Tel Aviv group achieved 0.96 ns with a scintillating fiber detector - we expect to reconfigure this detector into the scintillating fiber detector we need at the IFP and at the target. Therefore it is likely that the hardware time resolution will be better than we assume here.

- The target scintillating fiber system consists of three planes of scintillating fibers, so that an XY position can generally be determined even though the individual planes have about a 94% geometrical efficiency. In the logic for the system that we have described, all three planes are ORed together, so the system has essentially 100% geometric efficiency. If needed we can instead require timing signals on at least 2 of 3 planes of the detector. This requirement reduces the e and μ efficiencies about 1%, due to geometric effects and to the efficiency of particles being in the timing window. However, it has the effect of improving the timing resolution of this detector by a factor of $\sqrt{2}$, since the time is being measured twice. This should reduce the rate of π's identified as e's at 115 MeV/c by a factor of 3, and the rate of π's identified as μ's at 210 MeV/c by about a factor of 1000. The v1495 logic is flexible enough for us to independently choose to do this or not for each particle type (e's and μ's) at each energy. Our plan is to only implement the additional logic if needed.

- No fine tuning of the bins was done with the simple algorithm used, but it is clear from the figures that the e and μ efficiencies can be improved by extending the cuts into background free regions.

B. Calibrating the Beam PID System

It is important during the actual experiment to be able to determine the phase of the RF timing system and the optimal windows for the e and μ cuts, and to measure the system efficiency. This will be done with a high-precision, 50-ps time resolution South Carolina scintillator at the target position, after the target scintillating fiber array, and the scintillating fiber detector initially removed to minimize energy loss in the beam. We will use the FS11 channel jaws just before the first dipole to reduce the beam flux and make the rate of accidentals negligible. Closing the channel jaws is believed to leave beam properties other than the flux unaffected. At low rates, the data acquisition system can be set to read out and analyze essentially all beam particles. In analysis, since the relative timing of the 3 particle types is known, the RF time phase and the particle peaks can be identified in two distinct ways. First, since the channel selects a 3% bite in momentum, the π RF time peak is wider than the μ peak, while the e peak has no significant broadening since $\beta_e \approx 1$ at all beam momenta. Second, the fluxes of π's and e's are approximately known, so we know the relative sizes of these two peaks. Finally, a powerful check is that we should find the same RF time offset at all three beam momenta – the e peak position is independent of beam momentum. Figure 19 shows a simulation of the resulting RF time spectra in a South Carolina scintillator placed slightly downstream of the target position for all three beam momenta.

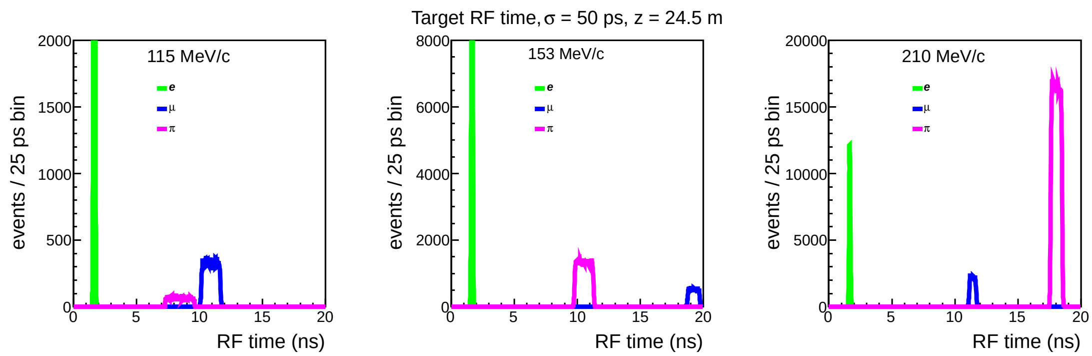

FIG. 19. Simulation of RF time distributions at the target for all proposed beam momenta, determined by a South Carolina scintillator. The absolute number of counts is arbitrary, but the relative number of counts for each particle type is based on estimates for positive polarity particles in the proposal. The squared-off peak shape results from the time of flight variation from the 3% momentum acceptance of the πM1 channel being much greater than the timing resolution of the scintillators. The difference in widths is due to the same momentum bite corresponding to different ranges in β for the different particles, and thus to different ranges in time of flight.

Determining the RF phase requires only relatively low statistics data, about 100,000 events so that even 1% components of the beam are reasonably well determined. Thus the time needed for this measurement depends mainly on the overhead of setting it up. Once the data analysis procedures are set up, the analysis time should be less than one hour. Once the RF timing phase is determined for the detectors at the target, the scintillating fiber array at the IFP can be put back in place, and its peaks easily identified as well in the event data.

The FPGA gates can now be programmed for each beam momentum. It is important at each channel setting to measure the efficiency for identifying particles as well as the fraction of other particles misidentified as e's or μ's. This can be done by the same measurement, taking event data on the beam PID system with the added South Carolina scintillator to much higher statistics, except that one important issue that we have omitted so far must be addressed first.

It is equally important to determine the rate, effect of, and corrections for accidental coincidences of multiple beam particles. Under normal running conditions, the beam flux will be ≈10 MHz, so there is about a 20% chance of more than one particle in a given RF bucket. (The Poisson distribution for an expectation of 0.2 background particles is 81.9% 0, 16.4% 1, 1.6% 2, and 0.1% 3 background particles.) If additional particles pass through different scintillating fibers, we obtain signals from multiple fibers in a plane, but the scalers can only count one particle of each type per beam RF bucket. (Note also that there is a small chance to have one particle with a trajectory at a sufficient angle, >40 mr, that passes through multiple fibers in a plane.) But if two particles pass through the same scintillating fiber in either detector, because of the width of electronic pulses the FPGA will only see the first pulse. The second particle signal will not be available for triggering logic or counting in the scalers. Given the size of the beam, the probability for this is ≈3% for the target SciFi array, but only ≈0.2% for the IFP SciFi array. Corrections for these effects can in principle be modeled if the time resolution of the system is well enough understood, but we plan as well to directly measure them.

The study will be done with a series of measurements with the same system, starting at low flux, about 10 kHz, and prescaling the different trigger types differently so that <0.1% statistics can be achieved in ≈3 hour runs. The entire set of measurements will require about 1 day. Studying the variation in efficiency and misidentification as a function of beam flux will allow the needed corrections to be precisely determined. Some care will have to be taken at the full beam flux, as it is likely that the South Carolina scintillator performance deteriorates at fluxes somewhat above 1 MHz. One way to extend the measurement capability is to divide the beam between multiple scintillators. Note that what is important is to determine the response of the SciFi + FPGA system to particles whose type is cleanly identified in the South Carolina scintillator; there is no problem with removing any ambiguous events from the analysis.

Finally, the stability of the beam RF must also be considered. As indicated earlier, there is some indication that the beam RF time is very stable when the machine runs, but can shift by up to 100 ps when the machine goes down and is brought back up.

Because of the high precision of the South Carolina scintillators, it is in principle possible to determine this indirectly by simply monitoring the RF time of scattered particles. But because of the variety of scattering and background events that occur, the most direct test is to continuously have a beam scintillator downstream of the target that is read out on all triggers. Thus we plan to put a scintillator enough beyond the target position that it can be left in and read out on event data. Accidental coincidences and short dedicated runs will allow the beam RF times to be monitored. If there are rate issues, we will replace one of the standard scintillators with a smaller one that samples a fraction of the beam. If the beam RF time is found to wander during the course of the run, it might be a simpler adjustment to have several interchangeable cables with lengths several mm different so that the RF time phase shift can be compensated for, rather than redoing the entire series of calibrations.

C. Summary

In summary, the beam PID and counting system consists of target and IFP scintillating fiber arrays, used with a custom FPGA system to identify particle types in hardware. This information is sent to scalers to provide beam normalization and to trigger logic so that we can efficiently trigger e- and μ-induced events, while suppressing π-induced events. Commissioning the system and calibrating its efficiencies is straightforward, using a South Carolina scintillator after the target Sci-Fi array. These activities will require 1 week of beam time, as we expect to do the calibrations twice at each energy.

V. BEAM MOMENTUM DETERMINATION

Since the elastic scattering cross sections depend on the beam energy, it is important to know the energy to extract the elastic form factor. Figure 20 shows the results of our study of the sensitivity of the measured cross sections to offsets in the beam energy. Roughly speaking, the relative change in the cross section is $1-2$ times the relative change in the beam momentum, and the variation of the correction with angle is several times smaller than the average correction. The change in the form factor, and thus in the extraction of the radius, is about half the change in the cross section. This suggests that knowledge of the beam momentum at about the 0.1% level is desirable.

Since the πM1 channel has a 3% momentum bite, we also studied the sensitivity of the measured cross sections to averaging over a range of beam momenta. Figure 20 also shows the result for averaging over a $\pm 1.5\%$ momentum bin, assuming a simple but unrealistic uniform distribution in incident momentum. For fixed scattering angles, we evaluated the average cross section for the full momentum bin and compared the result to the cross section for a mono-energetic beam at the central momentum. The effects of averaging are down about an order of magnitude from the effects of offsets, and are almost negligible.

Thus, in an idealized experiment the beam momentum sensitivity is small. We now consider some complicating factors.

In principle the momentum of beam particles can be determined by measuring the x position of beam particles at the channel intermediate focus position, DR8 – the channel resolution is known to be 0.1%. Since the optics are identical for π's and e's, which come from the same region of the πM1 production target, the channel momentum resolution should suffice for e's and π's. To our knowledge, the validity of using the position at DR8 for determining the momentum of μ's has not been established. It certainly does not hold

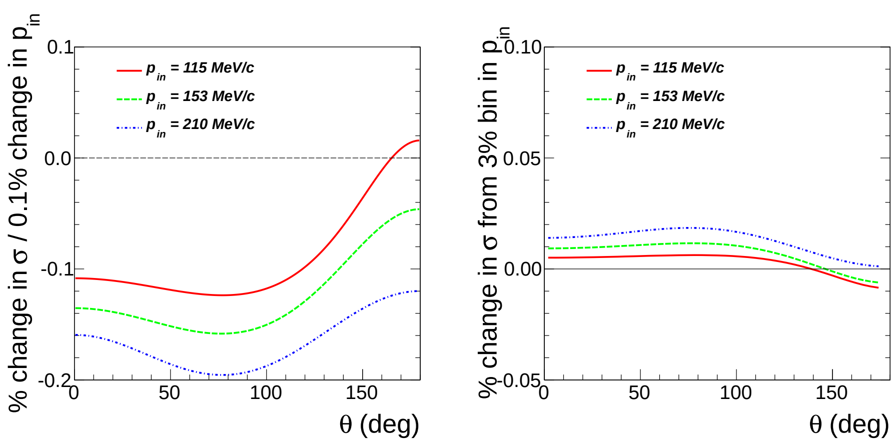

FIG. 20. Left: Change in cross section in percent for a 0.1% change in the beam momentum. Right: Change in cross section in percent when averaging over a $\pm 1.5\%$ bin in the beam momentum. The relative change in the form factor is half of the relative change in the cross section. Both studies used the Kelly form factor parameterization.

for μ's that result from π decays in or after the first channel dipole. But μ's produced in π decays near the production target might have sufficiently similar optics to the π's so that their DR8 x position provides a $\approx$0.1% determination of their momentum. In Section III we argued on the basis of beam line simulations that it appears that the momentum resolution of μ's at the IFP from the production target is close to 0.1%. To ensure this is about right, we need to perform an independent measurement of the beam momentum, to study the accuracy of the DR8 x position being used to give the μ momentum and to confirm the determination of the e and π momenta.

The basis of our plan to calibrate the beam momentum is to use a high-precision "South Carolina" scintillator near the target position to determine the beam momentum through time of flight (TOF) techniques – this is exactly the same set up discussed in Section IV that will be used to calibrate the beam PID and counting system.

If the TOF of a particle can be determined with uncertainty ΔT, then the momentum is determined to $\Delta p/p = (1 + \beta^2\gamma^2)\Delta T/T$. For the πM1 channel, we do not know the actual TOF, but we do measure the TOF of e's, μ's, and π's simultaneously. The e's have $\beta = 1$ to a good approximation for all our momenta, thus determining in essence the start time for the μ's and π's, at a cost of a factor of $\sqrt{2}$ worse resolution. We neglect here uncertainties from the z positions of the scintillators, which should be of order 1 mm / 10 m = 0.01%.

The resulting momentum determinations are shown in Table VII. The numbers calculated used a distance of 24.5 m from the πM1 production target to the scattering target, and assumed a 1σ resolution of 50 ps for the scintillator. It is important to understand

TABLE VII. Estimated momentum *resolution* – not the determination of the centroid – from μ and π RF time measurements. The result includes the resolution of the e peak.

Momentum (MeV/c)	σ_p/p_μ (%)	σ_p/p_π (%)
115	0.20	0.13
153	0.31	0.20
210	0.54	0.33

that this is the 1σ *resolution* for the beam momentum, the width of a presumably nearly

Gaussian peak. For determining the beam momentum, the important quantity is how well we know the centroid of the peak. Insofar as the peak is Gaussian, we can estimate the knowledge of the centroid to be $\Delta p \approx \sigma_p/\sqrt{N}$, but this is too optimistic as the TOF measurement will have some level of non-Gaussian tails to the peak. Past experience indicates that the peak centroid can probably be determined at the level of $\sigma_p/10$ - $\sigma_p/5$, but not significantly better. This is sufficient to determine the πM1 channel setting and beam central momentum at the 0.1% level or better. Note that this measurement is automatically done as part of the calibration of the beam PID and counting system.

TABLE VIII. Variation in timing from channel momentum acceptance.

Momentum (MeV/c)	$\Delta T/\Delta p_\mu$ (ps/%)	$\Delta T/\Delta p_\pi$ (ps/%)
115	510	765
153	320	500
210	185	300

Determining the central beam momentum can be done with reduced momentum acceptance to avoid the issue of the 3% momentum spread of the beam, but we do plan to run with the 3% acceptance. Table VIII gives the variation in timing of μ's and π's in ps/%; the full variation due to the 3% momentum spread of the beam is about three times the number given. These variation in timing are large compared to the timing resolution of 50 ps, and, as we should expect from the discussion of determining the central momentum, will allow a check of the dispersion of the channel through these timing measurements at the $\approx$0.1% level or better, and confirm the nominal 0.1% resolution. As discussed above, it is important that this be done for μ's since the validity of using the DR8 position to determine the momentum of μ's produced at the πM1 production target is not confirmed.

Confirming the dispersion of the channel requires knowing the DR8 x position of the beam particles. The DR8 SciFi detector determines positions, but also causes energy losses which affects timing, so using DR8 will not be the primary measurement. The dispersion can be done with multiple short measurements using different settings of the channel FS12 momentum-defining jaws, and we plan to use this technique, but we also plan as an extra check to insert a sieve slit immediately upstream of the IFP SciFi position that will also

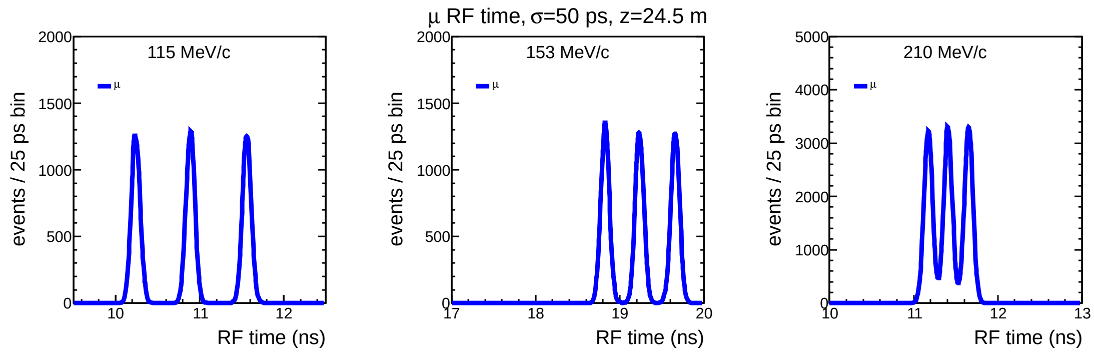

FIG. 21. Simulated timing spectra for a 50-ps resolution scintillator at z = 24.5 m with a 3-slit sieve at DR8. Slits are set at $\delta p = 0\%$, $\pm 1.3\%$ with widths of 0.1%. Only the μ portion of the spectrum is shown, since the π's have better peak separation while the e's have no peak separation.

provide separated timing peaks. Figure 21 shows the resulting RF time spectra for the three proposed beam energies. It is apparent that the peaks are sufficiently well resolved.

TABLE IX. Variation in timing at the target scintillator from energy loss in detectors at the IFP, and variation in beam momentum for a fixed 50-ps change in time at the target scintillator.

Momentum (MeV/c)	$\Delta T/\Delta E_\mu$ (ps/MeV)	$\Delta T/\Delta E_\pi$ (ps/MeV)	Δp_μ (50 ps) (%)	Δp_π (50 ps) (%)
115	300	530	-0.20	-0.13
153	130	220	-0.31	-0.20
210	50	90	-0.54	-0.33

The preceding discussion ignores the important issue that the energy of importance is the e or μ energy *when the particle elastically scatters from a hydrogen nucleus in the target.* Due to energy loss in the beam detectors and in the target before the scattering, this is not the same as the energy measured by the DR8 x position. The energy loss in the scintillating fiber detector at DR8 is ≈1 MeV. Table IX shows how the timing of μ's and π's changes due to energy loss in the scintillating fiber array, and also what momentum change corresponds to a change in TOF of 50 ps, the resolution of the system. It can be seen that the ≈1 MeV energy loss leads to a measurable effect in the timing of particles, and that the measured timing can determine the beam momentum change with a resolution of a few tenths of a percent. The energy loss dE/dx can be calculated with an accuracy of 4%, which is better than our TOF measurement resolution at all beam momenta. Also, the distribution of particle energy losses can be modeled with the well-known Landau-Vavilov distribution. As a result, measurements of beam energy loss in the IFP array should serve to confirm the accuracy of our models of the experiment.

The additional energy loss from the beam line detectors near the target and the target itself can also be calculated or even measured directly by inserting these materials into the IFP region. Finally, we note that the maximum energy loss possible is constrained in hardware by the coincidence trigger and in analysis by the measured RF time of the South Carolina scattered particle scintillators. Since the flight from the target and beam line detectors near the target to these scintillators is about a factor of 10 shorter than the flight path between DR8 and the scintillators, the measurement is correspondingly an order of magnitude less precise.

VI. BEAM SCINTILLATING FIBER DETECTORS

In this section we discuss the scintillating fiber detectors that we plan to use to measure beam particle momentum, RF timing, and as a result particle type.

A. Intermediate Focal Point Detector

In order to determine the beam momentum a scintillating fiber array will be installed at the intermediate focal point (IFP). The nominal dispersion at the IFP is 21 cm/3% = 7 cm/%, and the channel momentum resolution is 0.1%. Simulations show that the dispersed π beam at the IFP is 22.5 cm wide (full width at 10% maximum) with sharp edges. The vertical beam distribution is roughly Gaussian with width $\sigma = 0.60$ cm, and no visible tails outside ± 2.25 cm. The μ beam appears to be 2 - 3 cm wider in the dispersed direction, according to the simulations in Section III, but significantly wider in the vertical direction, about ± 15 cm. As discussed there, we believe much of the additional acceptance is from μ's that do not make it to the scattering target, and an important aspect of our test measurements will be to determine the needed active area at the IFP.

The required momentum resolution of 0.1% translates into a required position resolution of 7 mm, easily achievable with 2 mm × 2 mm scintillating fibers. The timing resolution required is at least 1 ns. We plan to use 2 planes of 128 2 mm × 2 mm fibers, offset by 1 mm. This geometry will leave about 1.5 cm of scintillator to each side which will measure background rates. Light readout will be performed by coupling the scintillating fibers directly to multi-anode PMTs of 64 channels each on both sides of the fiber.

An issue for positive polarity beam is that the channel has a large flux of low energy protons. The proton kinetic energies at our 3 momentum settings of 115 MeV/c, 153 MeV/c, and 210 MeV/c are 7.0 MeV, 12.4 MeV, and 23.2 MeV. We plan to stop these protons with a thin sheet of plastic. For polycarbonate, for example, the needed thicknesses are 0.6 mm, 1.6 mm, and 4.8 mm. The thickness will be adjusted to be appropriate for each beam momentum setting, to minimize multiple scattering and energy loss of the muons and electrons.

1. *Scintillating Fibers*

The existing Tel Aviv detector uses BCF-10 scintillating fibers manufactured by Saint Gobain Crystals. The core density is 1.05 g/cm^3. The refractive index of the scintillator core is $n = 1.68$. The core is surrounded by an optical cladding of polymethylmethacrylate (PMMA), with a thickness of 4% of the total fiber size, and a lower refractive index $n = 1.49$. An extra mural absorber (EMA), white coating (10 to 15 μm thick), is applied primarily to eliminate crosstalk among closely packed fibers. The trapping efficiency is 4% and is independent of the scintillator event's location in the fiber. The typical light yield of these scintillators is ≈8000 photons/MeV. The attenuation length of the scintillator material is 2.2 m (for 1 mm diameter, measured with a bialkali cathode PMT). The emission spectra of the fibers are shown in Figure 22.

2. *Multianode PMTs*

We plan to use the H7546B-200 multianode PMT manufactured by Hamamatsu Inc. The PMT is a 64 channel (8 × 8 channel) photomultiplier with individual readout for each channel. The fibers will be directly coupled to the PMT using Bicron optical grease

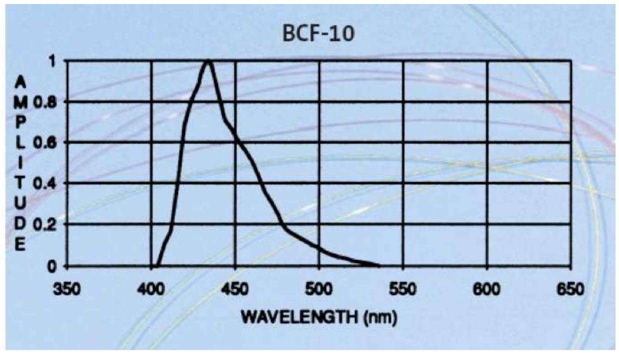

FIG. 22. Emission spectra of the BCF-10 fibers.

BC-630. The PMT spectral response is shown in Figure 23.

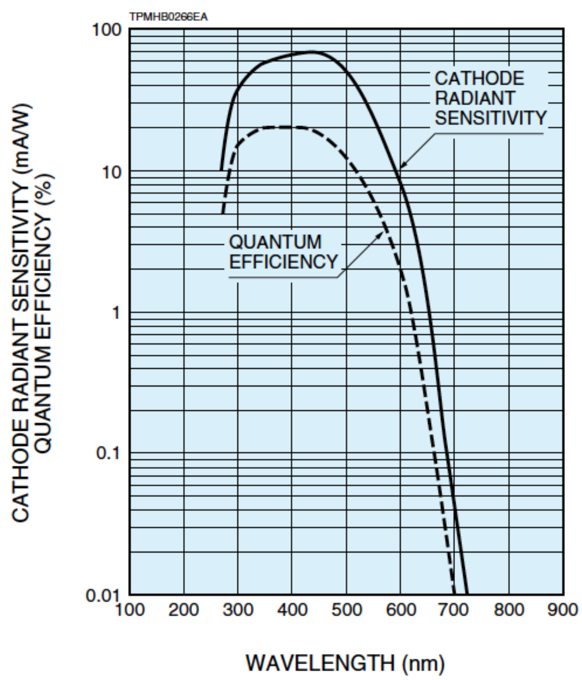

FIG. 23. Typical spectral response for the H7546B multianode PMT.

3. Light Collection Budget

Typical light yield for the scintillating fibers is ≈8000 photons/MeV. For a minimum ionizing particle we expect 8000 photons/MeV × 2 MeV/cm × 2 mm ≈ 3200 photons. For a collection efficiency of 4% (2% each side) and a quantum efficiency of 20% we expect

≈13 photons per event per PMT.

4. SciFi Array Prototype

The test setup consisted of a multianode PMT, 2 additional single PMTs, 9 scintillating fibers $2 \times 2 \times 750$ mm^3, and an additional scintillator counter $2.52 \times 252 \times 40$ mm^3, as shown in Figure 24.

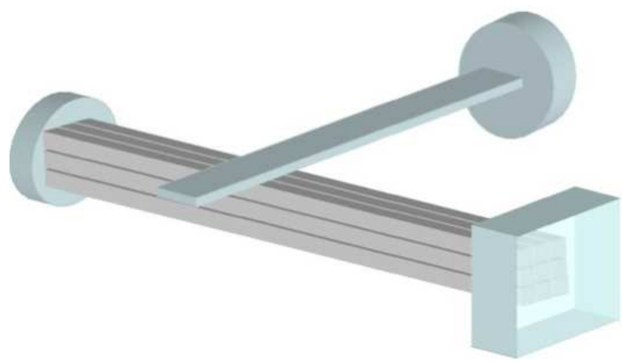

FIG. 24. A schematic of the test setup for the prototype array.

The time resolution of the multianode PMT was measured using a combination of two different anodes from the multianode PMT:

$$T = T_{Ri} - T_{Rj},$$

with the resolution defined as:

$$\sigma_{Meas} = \sqrt{2}\sigma_R,$$

where we assumed that all anodes of the multi anode PMT have equal timing resolution. The timing resolution was tested in three locations along the fiber. A representative timing histogram is shown in Figure 25. Each channel of the TDC corresponds to 40 ps, giving a timing resolution of 33.82 ch $\times$ 40 ps/ch / $\sqrt{2} = 0.96$ ns. At the analysis level, this leads to 0.68 ns resolution for each plane, and 0.48 ns from four signals on two planes.

To estimate the crosstalk we used a configuration in which the bar scintillator was placed parallel to the fibers. As described above all anodes of multianode PMT share the same

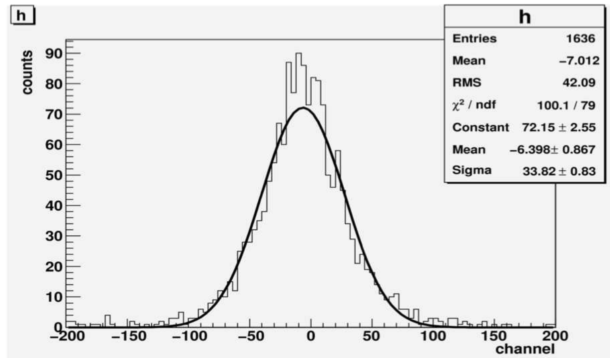

FIG. 25. A representative timing histogram for the multianode PMT.

photo-cathode. Due to this configuration there are possible false signals in one (or more) anodes that originate from (one or more) different anodes of the multianode PMT. The manufacturer of the multianode PMT states that the crosstalk is about 2%. A comparison of ADC spectra for real and crosstalk signals is shown in Figure 26. The signal is above channel 200. About 4% of the time a crosstalk signal is in this region; about half of the crosstalk events are from dark noise – the exponential of the pedestal peak – and about half of the crosstalk events are actual crosstalk. Thus the crosstalk signal is clearly well separated from the real signal. In addition, in order to further reduce crosstalk effects the ordering of the anodes on both sides of the fibers will be such that adjacent anodes will be different on each side of the fiber, significantly reducing the coincidence probability of crosstalk events. In the trigger electronics we will require coincidences of the phototubes at both ends of the fiber, which reduces the efficiency by less than 0.01%.

B. Target Scintillating Fiber Array

In order to identify the beam particles impinging on the target we plan to install a scintillating fiber array just upstream of the target, ≈23 m in flight path from the production target. The detector will consist of 3 planes of 2 mm × 2 mm scintillating fibers, arranged in an XYU configuration. The active area of the detector will be about 5 cm × 5 cm, leading to 25 fibers in the XY planes and 35 in the U plane. The intent is that this detector should be larger than the beam spot, and cover the aperture in the shielding. The additional 2 cm (1 cm on each side of the active area) will be used to measure the

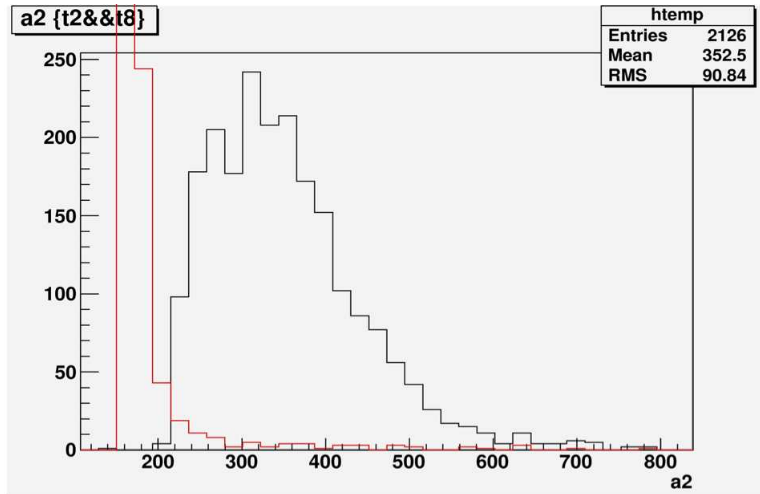

FIG. 26. A comparison of the ADC spectra for real (black) and crosstalk (red) events. The red crosstalk spectrum largely consists of pedestal events.

beam halo. Thus a large majority of decay particles that might make it to the detectors will still give good RF times in this counter, so that they can be identified by timing, and will give position information as well, which can also be used to reject them at the analysis level, and possibly at the trigger level, if needed. The fibers and PMTs used will be the same as those for the IFP detector. We will use 2 PMTs for each fiber (1 on each end) with the fibers coupled directly to the multi anode PMTs.

C. SciFi Detectors for Beam Test

The 3 single plane SciFi detectors to be used for the beam test – see Figure 27 – are modifications of the forward tracker of the SANE experiment at JLab. The scintillating fibers are Bicron BC-408, 3 mm × 3 mm square. Each fiber is glued to two 1.2 mm diameter wavelength shifting fibers (Bicron BCF-92MC) – see Figure 28. The WLS fibers are glued on the scintillator surface for light collection and to a multi anode PMT through a Delrin plastic block – see Figure 29. Each fiber goes into a single pixel in the PMT. The PMTs are Hamamatsu H75546B. The board on the PMT sums the signals from two pixels corresponding to the same scintillating fiber and the output goes into one cable.

FIG. 27. 3 SciFi planes to be installed for the test beam, one plane in the IFP and two near the target.

FIG. 28. Scintillating fibers and WLS fiber arrangement.

For the beam test we plan to use one counter at the IFP and two detectors at the planned target position area. The detectors at the target area can be arranged so that they are parallel and at a distance to measure angular divergence in each direction, or perpendicular to each other to produce a 2D beam profile of the beam.

VII. BEAM GEM DETECTORS

Measuring high-precision cross sections requires a precise knowledge of the kinematics of the scattering events. However, due to the large emittance of the secondary πM1 beam,

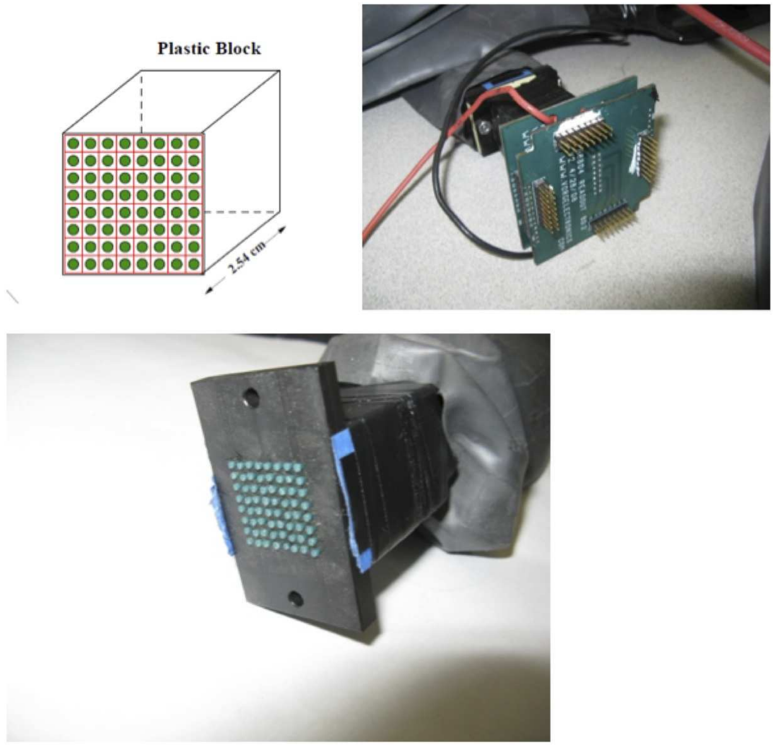

FIG. 29. Fiber coupling to the PMTs.

S

with a beam spot size of $\approx$4 cm (x) $\times$ 2.0 cm (y) and an angle divergence of about $\pm$20 mr (x' and y') – see Section III – it is necessary to measure the incoming trajectories on an event by event basis to reconstruct the kinematics.

Precise event-by-event tracking of beam particles with a spatial resolution of better than 100 μm and typical flux of 10^7 beam particles per second has been a serious technological challenge that has only been overcome in recent years. In the past, secondary-beam experiments with beam tracking typically had to rely on scintillator hodoscopes (also to be used in this experiment), which are limited to spatial resolutions determined by the thickness of scintillating fibers, typically to a few mm. Detectors providing higher spatial resolution such as wire chambers could by far not be operated at fluxes that high. In principle, the tracking resolution can be improved to arbitrary levels by using silicon strip detectors, which can be highly segmented down to the μm scale, however they are quite costly and are usually not as radiation-hard as one would like.

The most effective solution for tracking a 10 MHz beam with < 100 μm resolution is the use of GEM detectors (Gas Electron Multiplier). GEMs have been demonstrated to withstand harsh radiation environments while maintaining high resolution and efficiency for single events. Besides, they show little to no aging effects. GEMs have been successfully operated at intense high-energy muon beams at the COMPASS experiment at CERN, which has served as a role model for the development of GEMs in many other experiments and applications. They are low-mass detectors of order 0.5% of a radiation length, thus keeping multiple scattering at a minimum. Resolutions of 50-100 μm are typically achieved with a two-dimensional strip readout at some 400 μm pitch. This way the amplified charge is distributed over several readout strips as a few mm wide cluster, which allows for an improved resolution smaller than the pitch by using a centroid weighting technique. The two-dimensional hit information from several GEM detectors is combined to determine the beam trajectory. The reduced number of electronics channels and a rather simple construction scheme makes GEM detectors very cost-effective.

The Hampton group has developed, built, and is currently successfully operating a set of 10×10 cm^2 GEM detectors at the OLYMPUS experiment at DESY. These detectors will become available for the proposed experiment at PSI in the course of 2013, after OLYMPUS data taking has been completed. The OLYMPUS experiment aims to precisely measure the effect of two-photon exchange in elastic lepton-proton scattering at

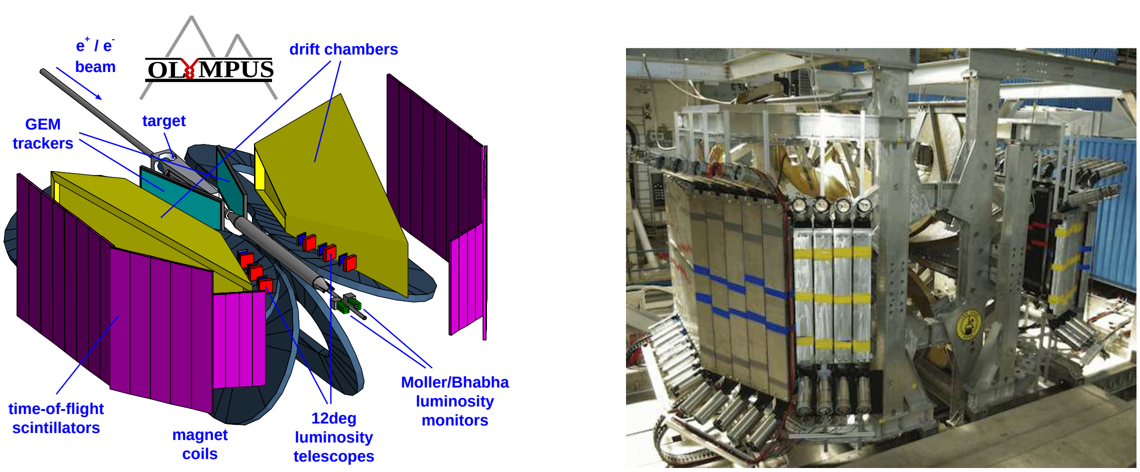

FIG. 30. Design and reality of the OLYMPUS experiment with components labeled in the figure. The schematics shows the forward-angle luminosity telescopes at 12 degrees. The photo was taken shortly before the installation into the DORIS ring in July 2011.

intermediate to high momentum transfer $Q^2 = 0.6$-2.2 $(\mathrm{GeV/c})^2$, by comparing the elastic electron and positron scattering cross sections. The layout of OLYMPUS is shown in Figure 30, along with a photo taken shortly before the rolling-in of the OLYMPUS detector into the DORIS storage ring in July 2011. At OLYMPUS, these GEM detectors are used for monitoring of the luminosity by determining the forward-angle elastic scattering rate on an event-by-event basis, where the two-photon exchange effect and difference between e^+ and e^- are expected to be negligible.

Three GEM elements have been arranged as a tracking telescope with approximately 40 cm gaps in between GEMs. One such telescope is situated at 12 degrees both in the left and right sector of OLYMPUS. The GEM elements are identified as US (upstream), MI (middle), and DS (downstream), left and right sector. Additional tracking elements built as multi-wire proportional chambers (MWPC) are located interleaved with the GEM elements. The tracking array is sandwiched between upstream and downstream scintillators read out by silicon photomultipliers which provide the trigger signal for the GEM readout. Both the GEM and MWPC telescope can be operated independently.

Figure 31 (upper half) is a picture of the nine GEM detectors produced for OLYMPUS. The lower half shows one of the GEM/MWPC tracking telescopes installed in OLYMPUS.

The OLYMPUS GEMs are 10x10 cm^2 in size and are read out with strips in two dimensions with a pitch of 400 μm. The design of the GEM stack parameters such as the drift gap and gaps between the three GEM layers and the readout plane follow that of the COMPASS design, which has been demonstrated to provide reliable detection of hit locations at routine rate densities of 2.5 $\mathrm{MHz/cm}^2$ and of up to 25-100 $\mathrm{MHz/cm}^2$ in dedicated tests. The expected rate density for a nominal beam spot at PSI of 1.0 x 1.5 cm^2 is approximately 7 $\mathrm{MHz/cm}^2$, with a single-track probability of over 80%. The OLYMPUS GEMs are therefore very suitable to provide event-by-event beam particle tracking under these conditions.

The GEMs are read out using FPGA-controlled frontend electronics based on the APV-25 chip developed for CMS. The readout hardware has been developed by INFN Rome and Genova for the Hall A SBS spectrometer in the framework of the 12 GeV upgrade of Jefferson Lab, and has been used for the first time in a realistic setting at OLYMPUS. It consists of a frontend card hosting the APV chip, which is directly attached to the GEM detector, and a VME based controller board hosting an FPGA located in the counting house at some 25 m distance. The APV processes 128 readout channels and pipelines both analog and digital information of 128 channels on a single cable. Raw signals on all strips are sampled with either 20 or 40 MHz frequency. After adjusting the latency, "snapshots" of the analog signal are taken and sent as frames to the VME based controller. The controller provides power, clock, and trigger to the APV, and receives and digitizes the raw data into on-board ADCs. The DAQ software is running on a CPU that controls the VME bus to write the data to disk or to send it to the event builder. As each APV chip reads out 128 channels, a 10×10 cm^2 chamber corresponds to 2x250 channels, which are read out with four frontend chips. One VME controller can operate up to 16 APVs, i.e. one such controller can operate up to four GEMs (two telescopes of three GEMs are

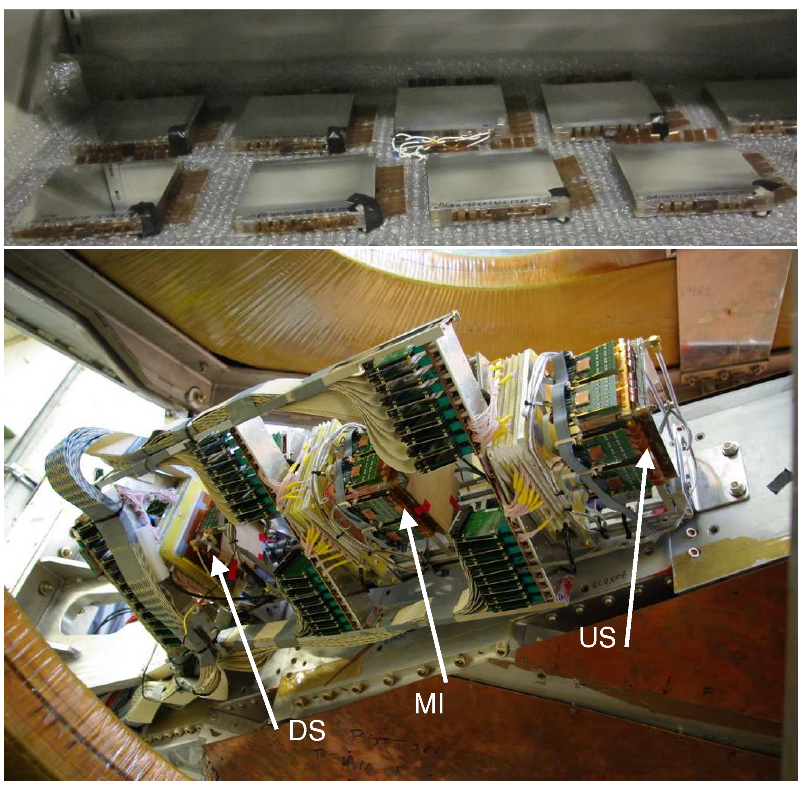

FIG. 31. Top: The final nine GEM elements produced for OLYMPUS. Bottom: Photo of the mounted tracking telescope for luminosity monitoring at OLYMPUS with the US, MI, and DS element labeled.

in use, each read out with one separate controller). The strip numbers and digitized pulse heights of the hit clusters in x and y give the spatial information for the track. Figure 32 shows the digitized pulse height after pedestal subtraction of a single event versus the strip number, of the US, MI, and DS GEM in both x and y direction (250 channels each). The red triangles indicate the candidate cluster locations returned by the cluster finding algorithm.

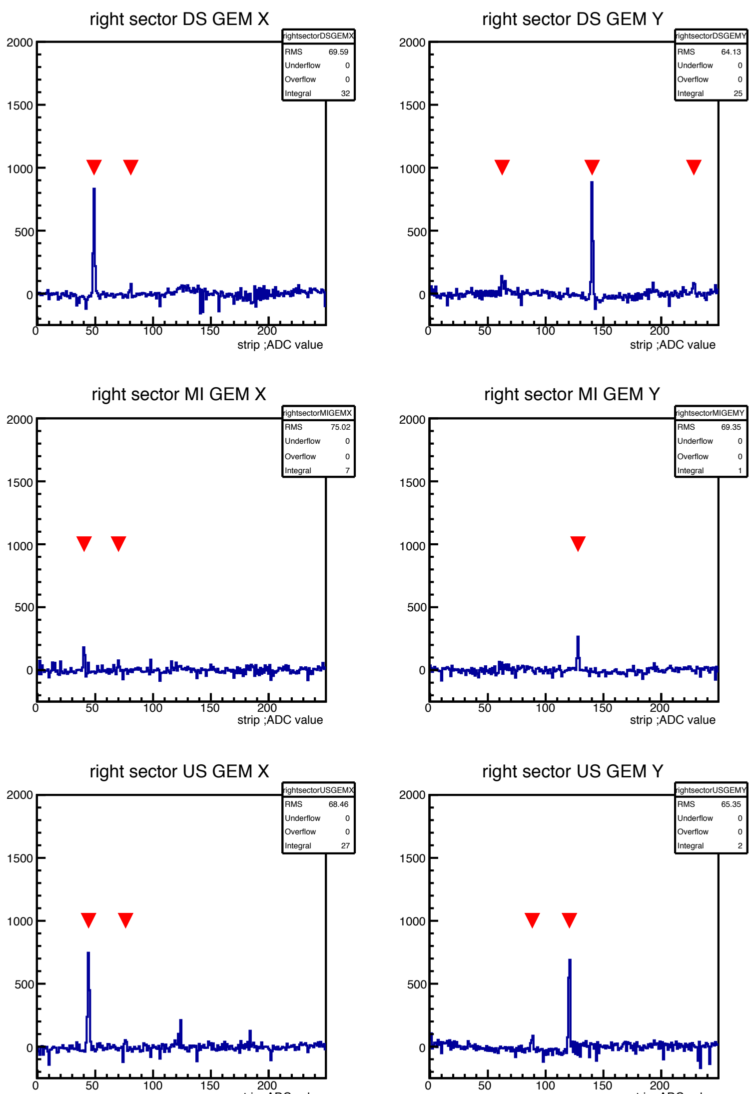

FIG. 32. ADC channel versus strip number in x and y direction for the US, MI, and DS GEM elements. The red triangles mark the location where the cluster finding algorithm yields a candidate cluster location.

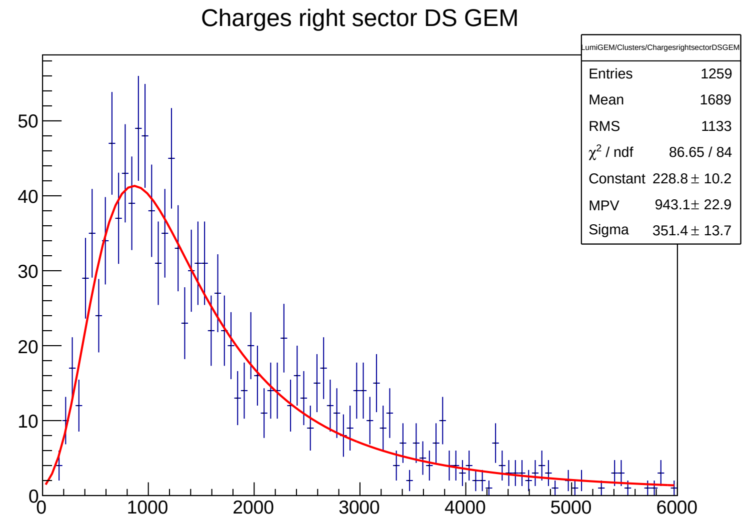

FIG. 33. Histogram of cluster amplitudes of the DS GEM element in the right sector of OLYMPUS. The data are well fit with a Landau distribution.

The cluster amplitudes observed with a GEM detector follow a Landau distribution, displayed in Figure 33 for the right sector DS element. To generate this plot, pedestals were subtracted from the raw ADC data. The ADC values for 250 strips were processed through a Gaussian filter to reduce single-channel noise. For the identification of a charge cluster, multiple adjacent strips are expected to give a higher reading than the pedestal. The algorithm is looking for local maxima as a function of strip number. The cluster amplitude is obtained by integrating the readings of the active strips belonging to a local maximum. As is expected for low-mass detectors, the amount of amplified charge from the ionization process follows a Landau distribution.

One important property of GEM detectors is the sharing of the collected charge of a cluster between the x and y strips. Figure 34 shows how the charge cluster amplitudes are correlated between the x and y strips of the three GEMs. If charges are read in equal portions in both directions, one expects a good correlation at equal magnitudes for any given charge cluster. This has been established very well as seen in the two-dimensional figures for the US, MI, and DS element shown for a common data sample.

In order to achieve a readout rate of order 1 kHz, sparsification of the GEM readout will be implemented. In principle, the GEM readout can be sparsified (or zero-suppressed

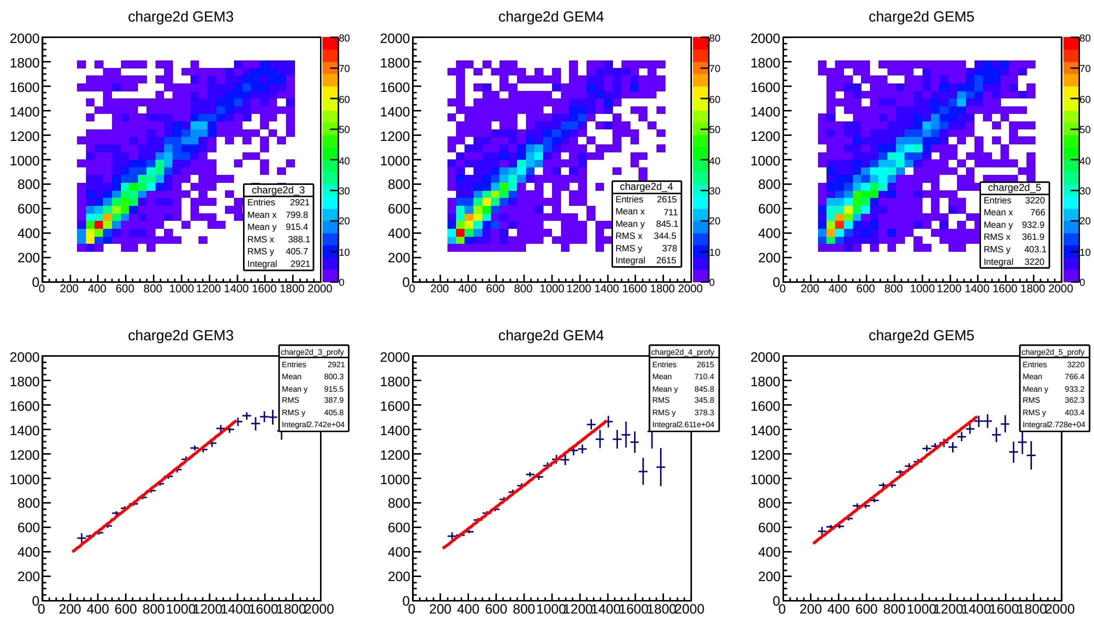

FIG. 34. Sharing of cluster charge between strips in x and y orientation.

after pedestal subtraction), either at the hardware level or at the DAQ stage. Algorithms for sparsification in the presence of common mode noise have been partially developed but not yet fully implemented. In the OLYMPUS experiment, the readout rate in the telescopes has been of order 100 Hz, for which sparsification has not been required.

The OLYMPUS GEM telescopes have been working very well. The operation has been very stable, noise levels are very low. Intrinsic resolutions have been found to be around 70 μm, and the efficiencies appear to be very close to 100%, as shown in Figures 35 and 36.

As mentioned above, this system will be available for the proposed experiment at PSI after completion of OLYMPUS in 2013, including expertise and manpower. The same postdoc – Dr. Jürgen Diefenbach – who has built and successfully brought the GEM system into operation will be available to transfer the system from DESY and to re-commission it at PSI.

For the planned beamtest in fall 2012, two GEM detectors will be provided by the UVa group to study beam properties such as composition of pions, muons, and electrons, beam flux, as well as beam size and divergence. The UVa GEMS are similar in size and

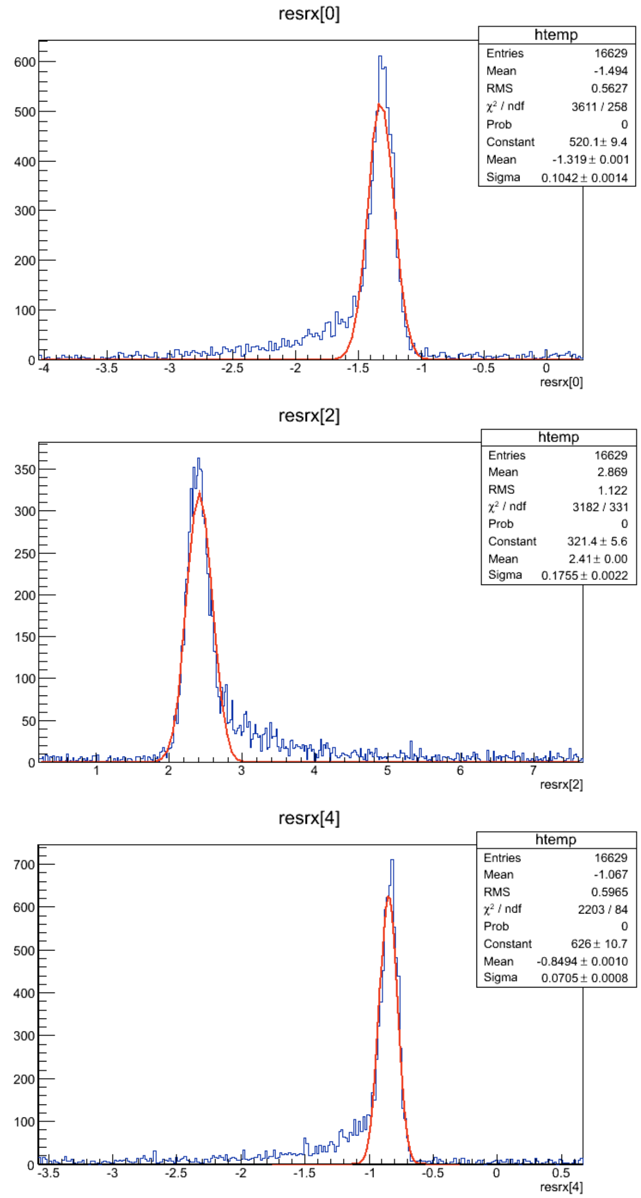

FIG. 35. Track residuals for OLYMPUS forward-angle trajectories in the 12-degree GEM telescope fitted with straight lines. The residual width is composed of the intrinsic resolution and the track uncertainty. The residual centroids are off zero and of opposite sign of the middle GEM element due to the curvature of the track. Intrinsic resolutions of 73 μm, 75 μm, and 70 μm have been achieved for the US, MI, and DS element, respectively.

performance to the Hampton GEMs that will be used for the actual measurement.

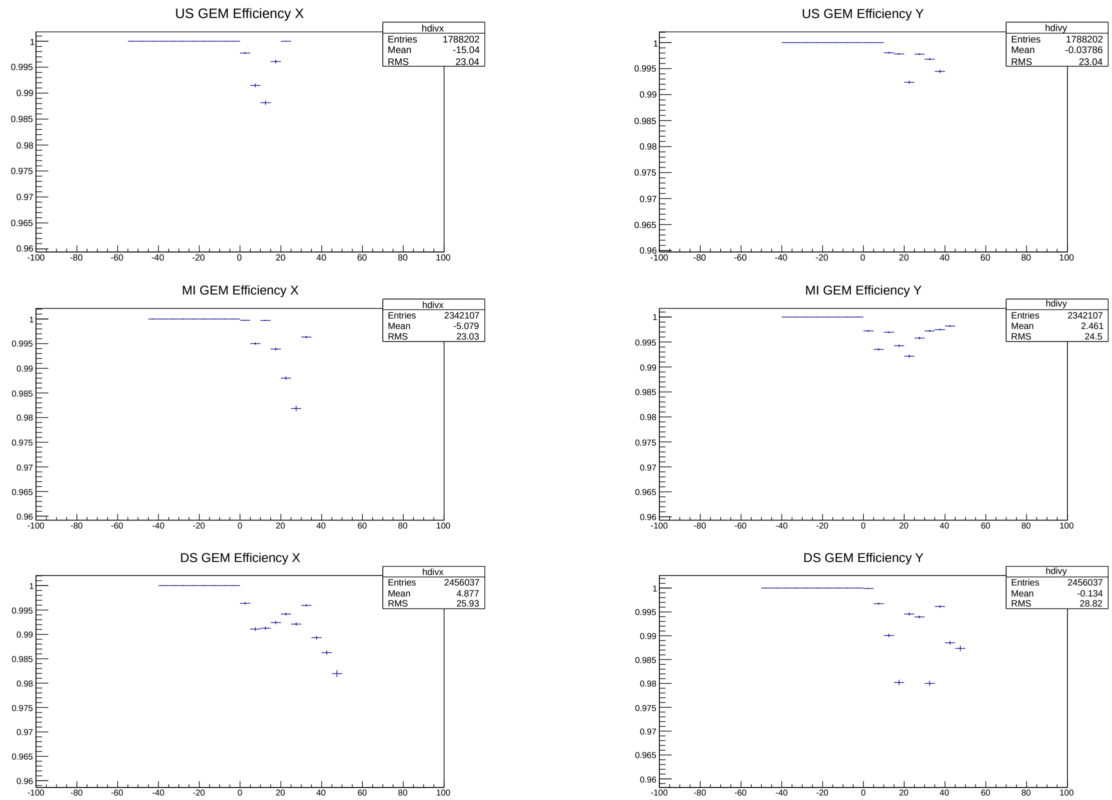

FIG. 36. Efficiencies of the US, MI, and DS GEM elements as a function of x and y. Tracks were identified and fitted with 3 MWPC + 2 GEM elements, in order to verify if the respective third GEM element shows a hit at the expected location. Efficiencies are generally very close to 100% and are exceeding 98% even in regions of local inefficiencies.

VIII. TARGET

Measuring elastic μp and ep cross sections requires scattering from a hydrogen target. We choose to use a liquid hydrogen target, rather than a solid CH_2 foil, for example, to reduce the amount of other nuclei in the beam, and thus to reduce unavoidable subtractions of backgrounds of nuclear elastic scattering that would increase our uncertainties. Rutgers University has assumed responsibility for the target.

Liquid hydrogen targets in vacuum systems are a mature technology, with existing targets capable of handling kW level power depositions. For the experiment proposed here, the anticipated power deposition in the target is $P \approx 7$ MeV$\cdot$cm^2/g $\times$ 0.3 g/cm^2 $\times$ 10^7 e/s $\times$ 1.6$\times$10^{-19} C/e = 3$\times$10^{-6} W = 3 μW.

A recent example of a low-power, standalone, cryotarget system is the Fermilab E906 [44] target, developed by the Michigan and Maryland groups. This system provides a model for a modern low-power – beam power deposited in the target is about 3 W – standalone target produced with up to date safety standards. As such, we expect the cryotarget system for this experiment to be generally similar to the E906 system. However, in this section we will largely not consider issues of cryogenic target safety, instrumentation, etc. We expect a safety review of the target will be required by the laboratory subsequently. We will instead focus of issues of the cryocell design and vacuum system windows, since the interaction of the beam with these elements directly determines the statistics of the measurement, backgrounds, and resolutions, and on target systematics.

The main issue with a simple copy of the E906 system for use in this experiment is that the target was built with the needs of an experiment where an incident 120-GeV proton beam interacts with a long target to produce several GeV muons that subsequently go through meters of concrete and detectors. The system uses vacuum windows and a cryotarget cell that would lead to too much multiple scattering and thus are too thick for this experiment.

An example of a system with much thinner walls is the Fermilab E907 target [45], shown in Figure 37. In this target the liquid hydrogen was contained in a 125-μm thick mylar/kapton flask. The vacuum system in the region of the target used an almost spherical shell 15.2 cm inner diameter and 5 mm thick, made of Rohacell (a low density foam) + fiberglass + epoxy. The target cell is made by gluing a sheet of mylar into a tube, and forming ≈2-cm long end caps that are then glued over the ends of the tube. Hydrogen liquid enters through the bottom and exits through the top of a support clamp that surrounds the tube, near the upstream end.

Figure 37 also shows an example of a kapton target cell used by the Mainz MAMI A2 collaboration for real photon experiments. Beam enters from the right. Hydrogen fills the region between the outer kapton cell and an inner aluminum tube which supports a kapton entrance window. The cell is formed by gluing a kapton sheet into a cylinder, and gluing on a short ≈5-mm long end cap. There is a small lip on the end cap to provide a larger gluing surface. Hydrogen enters and exits the cell through the metal base at the right edge of the photo.

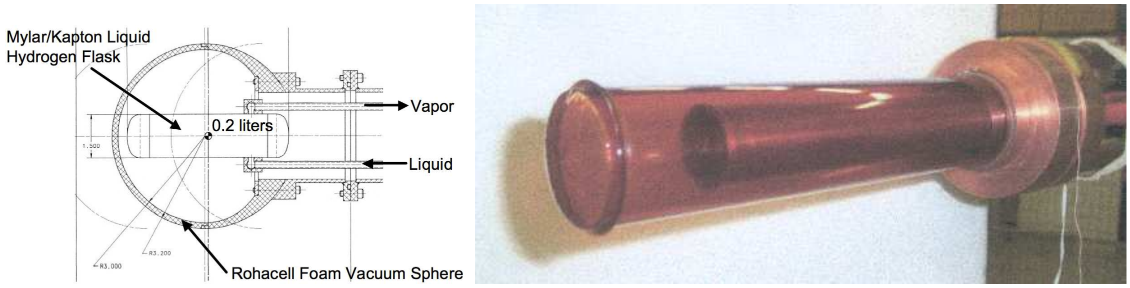

FIG. 37. (Left) Drawing of the Fermilab E907 cryotarget. Beam enters from the right. (Right) Picture of a kapton target cell used in Mainz MAMI A2 photon experiments. The entrance window and the tube on which it is mounted can be seen inside the kapton cell.

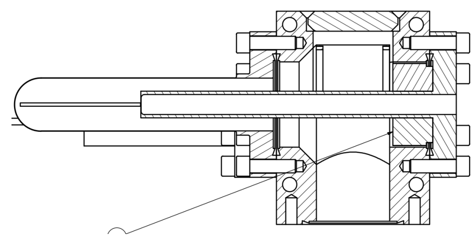

FIG. 38. Drawing (top view) through part of the Jefferson Lab Hall A cryotarget, showing the cell, flow diverter, and entrance tube and window to the left, and the cell block to the right.

The standard Jefferson Lab high power cryotargets use Aluminum cells, typically with 0.1 mm thick walls, in a variety of geometries. The "beer can" geometry, shown in Figure 38, is very similar to the Mainz kapton cell shown in Figure 37, with the liquid hydrogen pumped into one side of the cell, vertical flow diverters installed at the top and bottom of the cell cause the hydrogen flow to be largely transverse where the beam goes through the hydrogen, and the hydrogen flowing out the other side of the cell. The "tuna can", and "race track" configurations use a vertical flow configuration, with hydrogen entering the top of a thin walled cell and exiting the bottom.

For a low-power experiment such as this one, the slightly thicker 125-μm kapton flask – kapton is preferred over mylar for hydrogen targets – is superior to the thinner 100 μm Aluminum in providing reduced multiple scattering ($\approx$0.044% of L_{rad} for kapton vs. $\approx$0.11% of L_{rad} for Al for entrance or exit window), reduced energy loss (0.032 MeV for kapton vs. 0.044 MeV for Aluminum for entrance or exit window), and a reduced rate of nuclear scattering backgrounds.

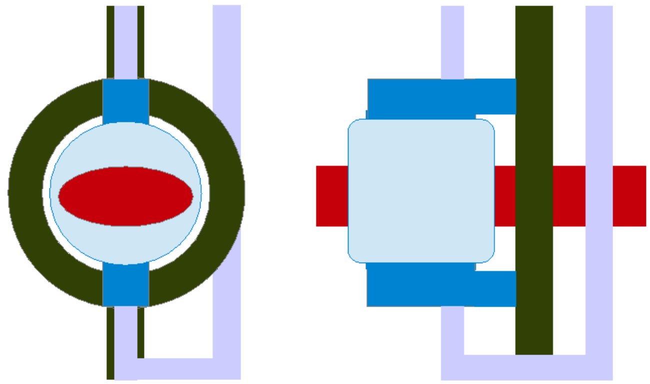

FIG. 39. Cartoon of the planned design for the target cell of this experiment. (Left) End view. (Right) Side view. The beam goes through an annular support ring into the target cell. The cell is supported between two arms coming out from the support ring. Liquid hydrogen fill and vapor exhaust tubes attach to the kapton cell through the support arms. The cell is also wrapped in aluminized mylar (not shown).

With the scattered particle detectors to the sides of the beam, constraints from a low-energy beam and multiple scattering, and a desired scattering angle range of 20° - 100°, the optimal choice of the target cell configuration is similar to the Fermilab 907 design, but with a kapton cell with endcaps of the Mainz design, and supports above and below, but not around the cell. Although the Mainz design has obvious lips that appear to have more material than the E907 flask, in the 907 design there is a ≈1 cm overlap of the cylinder and the end cap to provide a gluing surface, so there is actually more material in the 907 design. This configuration is shown in Figure 39.

We are tentatively planning on a 4-cm long 4-cm diameter cell. Based on the beam line simulations in Section III, this will lead to tails of the beam going through the side walls of the cell. The cell size might be adjusted in light of the planned measurements of the beam size, but we note that whatever the cell size the beam halo will go through the walls, and fiducial cuts on the incoming particle will be a necessary part of the analysis.

There are several contributions to the systematic uncertainty from the cryotarget.

- For operational temperatures about 19 K, the density change in the target is about 1.5%/K. With calibrated resistors the temperature can be determined to better than 0.1 K and thus the density to ≈0.1%.

- The variation of density with pressure is about 0.01%/psia. Pressure can be determined to at least 0.3 psia, so the uncertainty is small.

- Room temperature H_2 is largely in the ortho (spins parallel) configuration, but cryogenic H_2 liquid is >99.8% para (spins anti-parallel). The time constant for the conversion is of order a day for pure H_2, but typically small amounts of contaminants in the hydrogen shorten the conversion time significantly, an order of magnitude or more. The density difference between the two spin configurations is about 0.6%. As long as the cryotarget is cooled a few hours before data taking, the uncertainty from the ortho-para fractions is small.

- The equation of state is known to about 0.1% for LH_2.

- In high-power experiments, there is an issue of energy deposited in the target leading to boiling. For this experiment, the 3 μW expected from the beam is insignificant.

- Thermal radiation is however a significant issue. If we use $\epsilon = 1$, as for a black body, the room temperature surroundings radiate $\approx$3.5 W of power into the cryotarget cell, potentially leading to bubbles and density variations. This energy transfer is typically suppressed by wrapping the target in 8 or so layers of aluminized mylar, to reflect the thermal radiation. The emissivity of aluminized mylar or kapton is $\approx$0.03.

- The length of the target cell varies with temperature. It is possible to estimate the change in length form thermal expansion coefficients, and to measure the change in dedicated tests. This uncertainty is typically a few tenths of a percent.

- The target cell length for the planned design varies by about 5% from the center to the edges. It will be necessary to measure the beam position and angle distributions and use a Monte Carlo to determine the average thickness. Since the central 2σ of the beam are about 2 cm diameter, vs the 4 cm cell, the total variation in length for much of the beam is only about 2%. The uncertainties will have to be evaluated from the simulation, but are likely not more than a few tenths of a percent.

- The position of the target has to be determined relative to the beam. Spectra of reconstructed z_{target} from particles scattered at large angles can likely determine the z position of the target to ≈0.5 mm, but the data cannot be used to determine the transverse positions. The uncertainty typically leads to several tenths of a percent uncertainties in systems with relatively larger curvature of the end caps compared to the beam size. Here it appears to be smaller.

Considering the above points, it appears that the point-to-point systematic uncertainty due to the cryotarget is negligibly small. For each beam momentum the target contribution to the luminosity is the same for all points. When beam momenta are changed, the energy deposited by the beam in the target is so small that the momentum change does not matter. The likely issues with the point-to-point uncertainty, which will need to be evaluated based on the target performance during the run, are whether there are any day-night or seasonal changes in ambient temperature that lead to differences in thermal radiation and boiling in the target, and whether the target operates stably. Power glitches or reboots of electronics could affect the target density.

For the absolute density, there are several effects that are at the 0.1% level, and the total uncertainty should be about 0.5%. Achieving this uncertainty in practice will require dedicated measurements to understand what if any target boiling there is from thermal radiation, and how the target cell length and position vary when the target is cooled. Dedicated measurements can be done either optically or with, for example, X-rays.

The simplest way to construct the vacuum system is to mount the targets in a vertical vacuum pipe ≈15 cm diameter. The cold head for the target will be at the top of the tube, above a bellows which will allow the target vertical position to be adjusted between cryocell, dummy foil, and empty target settings, while allowing all the electronics and motion system to be in air. The tube will require thin entrance and exit windows. The entrance window will be circular with 4 cm diameter, corresponding to an angular range of 31° in the backward direction. So that the acceptance is not limited by scattered particles passing through the thick vacuum wall on their trajectory towards the scintillators, the exit window needs to be about 16 cm high, and cover the angle range from -120° to +120°. While the entrance window can be much thinner, about 50 μm of kapton, the exit window will need to be about 200 μm thick. Because the angle range of the windows is large, support posts might be necessary.

IX. SCATTERED-PARTICLE SCINTILLATORS

The scattered-particle scintillators are part of the event trigger and help with the particle separation via time-of-flight (TOF) measurements. This requires high detection efficiency for the particles of interest and excellent timing resolution.

The Experimental Nuclear Physics Group at USC is committed to build the scattered-particle scintillators for the preset experiment. The group has extensive experience in assembling large time-of-flight detectors. It has also designed and prototyped the new FToF12 detector for the upgraded CLAS12 at Jefferson Lab. During the next three years all scintillators will be built, tested at USC, then mounted and commissioned at JLab. With only the exception of the thickness of the scintillator bars, we are planning to copy the design and construction procedures of the FToF12 bars. Figure 40 shows CLAS12 FToF scintillation bars in a cosmic-ray test. The FToF12 scintillation bars are rectangular in

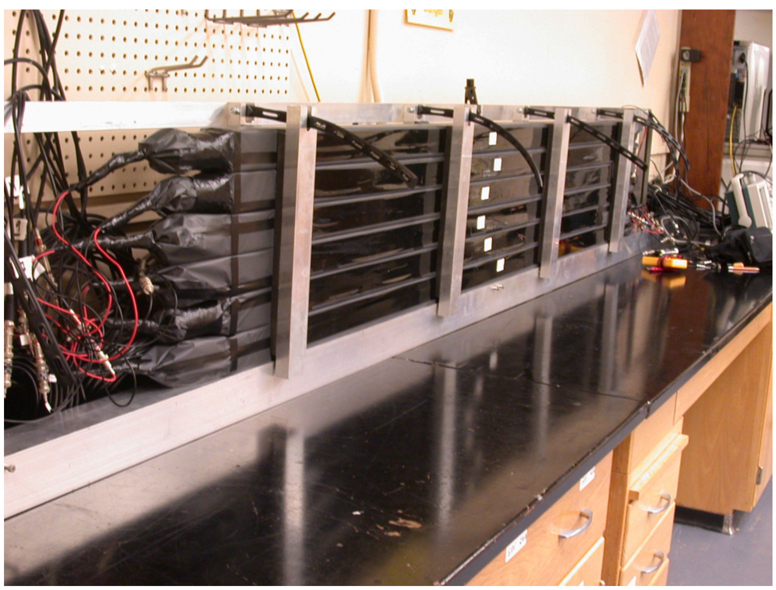

FIG. 40. CLAS12 FToF scintillation bars undergoing cosmic ray testing at USC.

shape with a cross sectional area of 6 cm $\times$ 6 cm. Position-dependent time resolutions have been measured in cosmic tests for scintillator bars of various lengths; see Figure 41.

Average time resolutions of $\sigma_{avg} = 34$ ps and $\sigma_{avg} = 51$ ps for the 69-cm long and 203-cm

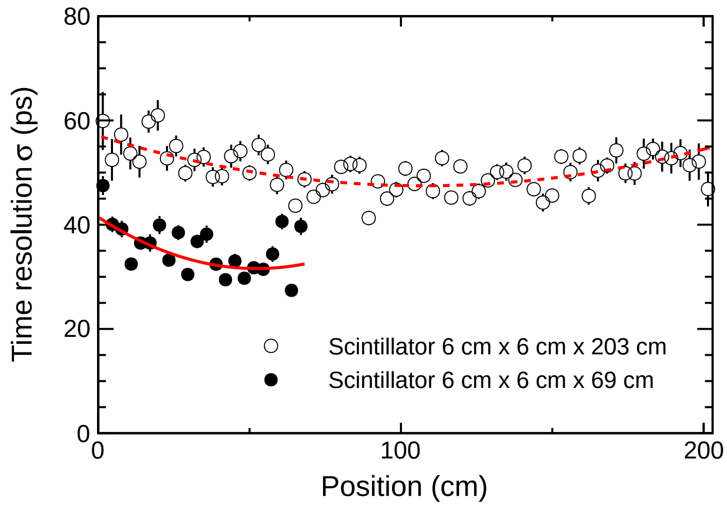

FIG. 41. Position-dependent time resolution for two CLAS12 203-cm and 69-cm long scintillator bars after calibration, event selection, and time-walk correction. The average time resolution is $\sigma_{avg} = 51$ ps for the 203-cm bar and $\sigma_{avg} = 34$ ps for the 69-cm bar, respectively [46].

long bars, respectively, were achieved.

The detector will be made of Saint-Gobain BC-404 plastic scintillators, which have a high light output and fast rise time. Each end of the scintillator is fitted with black tape, which masks the corners while leaving a circular window that extends one millimeter into the area that will be covered by the photocathode. The corner blocking reduces the amount of reflected light contributing to the leading edge of the PMT signal. Hamamatsu R9779 PMTs are then glued to each end of the scintillator. The bare counter is wrapped with precision-cut aluminized Mylar and DuPont$^{\text{TM}}$Tedlar. The Tedlar film extends beyond each PMT onto the anode, dynode, and high-voltage cables, providing a single light-tight casing for the entire counter. Details about the construction process and system tests for quality assurance can be found in Ref. [46]. Table X lists the design parameters for the scintillator walls. The front wall is square and covers at least a horizontal angular range from 20° to 100° from all points within the target. The back wall is also square with an increased angular acceptance to account for particles which scatter in the front wall material.

We have studied the performance of the proposed scattered-particle scintillators with

TABLE X. Design parameters for the scintillator walls.

	Front wall	Back wall
Number of scintillator bars	17	27
Scintillator cross section	6 cm × 2 cm	6 cm × 6 cm
Scintillator length	103 cm	163 cm
Target to front-face distance	50 cm	73 cm
Gap between scintillator bars	0.02 cm	0.02 cm
Scintillation material	BC–404	BC–404
Photomultiplier	Hamamatsu R9779	Hamamatsu R9779

Geant4 simulations of the proposed setup. The particle interactions and their energy deposition within the scintillators have been calculated. Figure 42 shows examples of such interactions. Panel (b) shows a relatively rare event which also includes a particle decay, $\mu^- \to e^- \bar{\nu}_e \nu_\mu$. Scintillator bars with energy depositions are marked in red.

Figure 43 shows a measured energy distribution with cosmic rays in units of ADC channels for one FToF12 6 cm × 6 cm scintillator. The energy deposited by particles whose paths do not traverse at least the full thickness of the scintillator is lower than the energy of the lower edge of the Landau-like portion of the energy distribution. Simulated energy distributions for the 6 cm × 2 cm and 6 cm × 6 cm scintillator bars are shown in Figure 44 for scattered electrons, panel (a), and muons, panel (b), at various beam momenta p_{in}. The set of curves with low energy deposition is for the front wall; the set of curves with high energy deposition is for the thicker back wall. In the studied range, the energy depositions for $e^{\pm}$ are independent of the beam momentum. The simulation shows for each event the maximum energy deposition in any front- or back-wall bar. Very nearly all events have energy depositions above threshold, $E_{th} = 2$ MeV, in (at least) one bar. The detection efficiency is indeed very high.

A detailed view of the particle detection efficiencies for the scattered-particle scintillator walls is shown in Figure 45 as a function of the particle scattering angle. All panels are for the same detection threshold of $E_{th} = 2$ MeV but various particles and beam momenta.

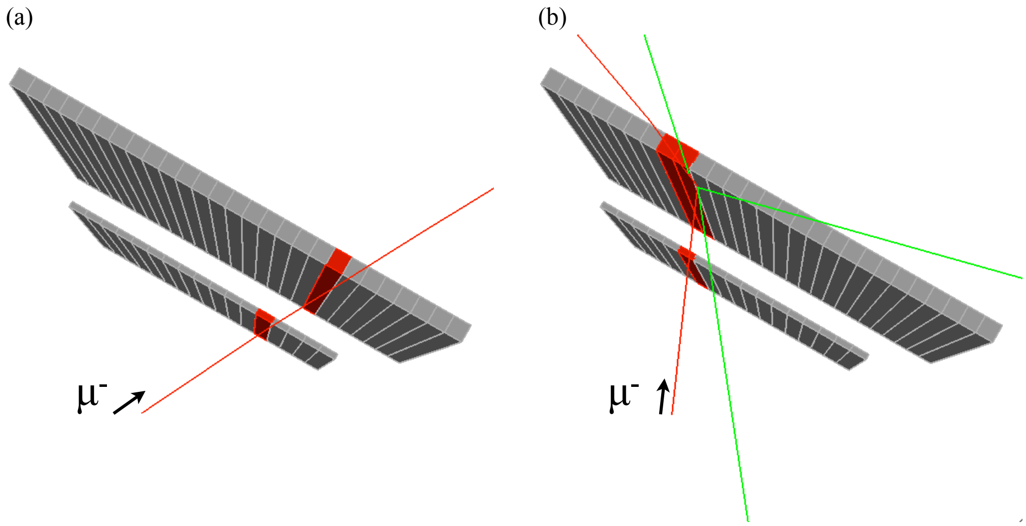

FIG. 42. Geant4 simulation of μ^- interacting with the two scintillator planes: Panel (a) shows a common event with a μ^- depositing energy in one paddle in the first and one paddle in the second plane; $p_\mu = 150$ MeV/c. Panel (b) shows a rarer event of an incoming μ^- particle with 100 MeV/c momentum which interacts in a paddle in the first plane, and subsequently deposits energy in three paddles in the second plane. Some neutral particles are produced (green tracks).

The solid dots give the ratio of events with an above-threshold hit in the front plane per incident particle. Particles were incident on the 'active' area of the scintillator plane; the physical size of the plane is slightly larger. The overall geometrical acceptance for the 'active' area is shown in Figure 46.

This one-plane efficiency is practically 100%. The two-plane coincidence requires above-threshold hits in both, the front and back planes. It is in all cases well above 99.5%, except for e^+. The 'directional cut' utilizes the fact that scattered particles, which originate in the target, deposit energy mostly in certain combinations of front- and back-wall scintillators. For an event to pass this cut, each hit in a scintillator bar of the back wall must coincide with hits in up to three corresponding neighboring scintillators in the front. This directional cut does not affect the efficiency much but helps to suppress triggers from background events which do not originate within the target. Figure 47 illustrates this correlation of scintillator-bar numbers for various particles with different momenta originating in the target volume.

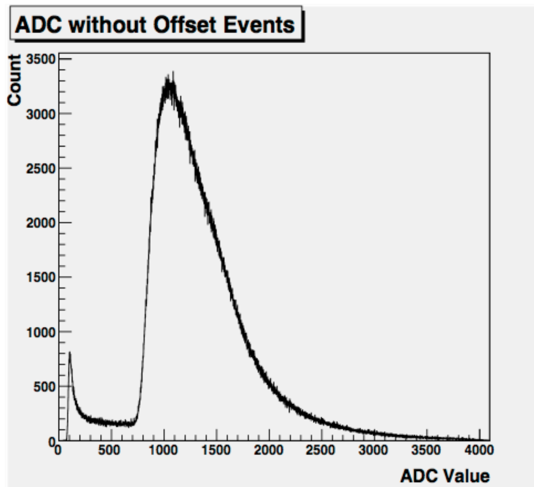

FIG. 43. Measured deposited energy for cosmic rays passing through a FToF12 6 cm × 6 cm scintillator bar [46].

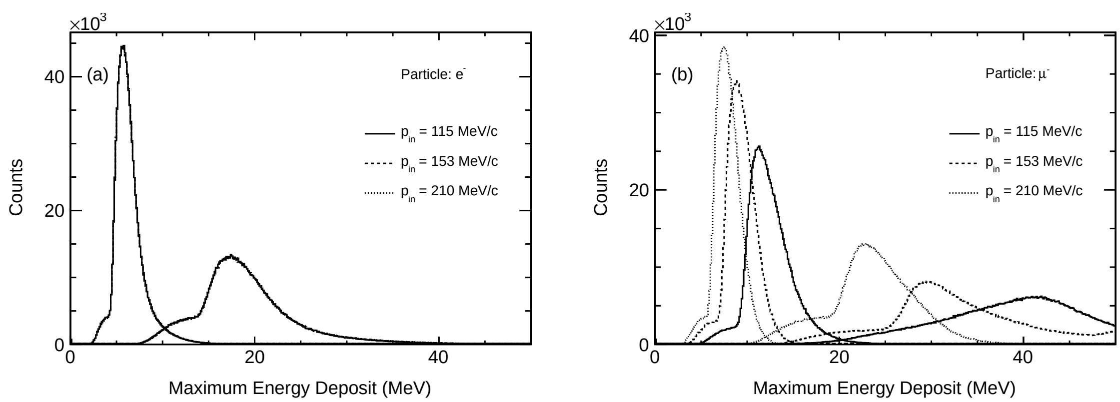

FIG. 44. Simulated energy deposition for scattered electrons, (a), and muons, (b), traversing the 6 cm × 2 cm bars of the front and 6 cm × 6 cm bars of the back scattered-particle scintillator wall, respectively. The simulation recorded for each event the maximum energy deposition in a scintillator of a given plane.

Table XI summarizes the result of our efficiency estimates. While the μ detection efficiency remains well above 99% for all momenta, the e efficiency starts to decrease at thresholds larger than 2 MeV.

Figure 49 shows a simulation of the reconstructed reaction vertex along the beam line, $x = y = 0$, where the reconstruction only uses the position of hit bars and their geometrical position on the lab. Events shown have above-threshold hits in the front and

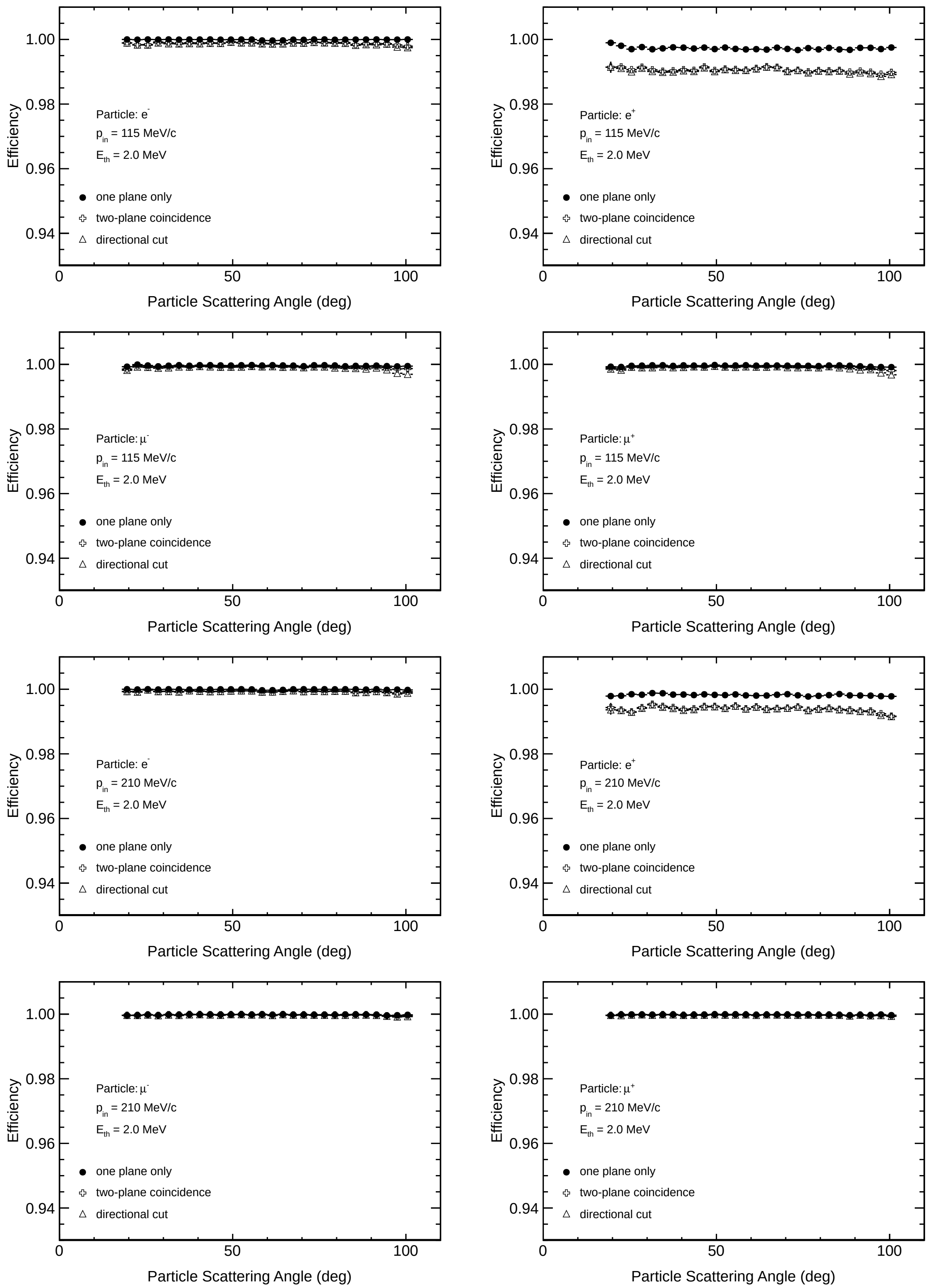

FIG. 45. Estimated detection efficiency as a function of particle scattering angle for e^+, e^-, μ^+, and μ^- and beam momenta of 115 MeV/c and 210 MeV/c. The change of momentum of the scattered particle with scattering angle is taken into account.

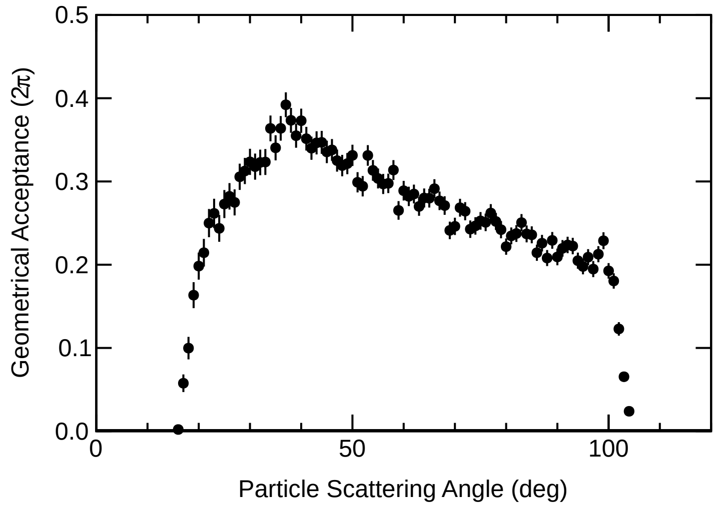

FIG. 46. Estimate of the geometrical acceptance of one scintillator wall as the fraction of high-energy muons originating from the target and uniformly distribution which hit the wall.

back scintillators walls which fulfill an additional directional cut. The figure shows the effectiveness of the directional cut.

We have estimated background rates in the scattered-particle detectors. Beam particles, $\pi^{\pm}$, $\mu^{\pm}$, and $e^{\pm}$, at a rate of 1 MHz with momenta of 115, 153, and 210 MeV/c, respectively, were sent in the $+z$ direction and allowed to decay, to scatter off air, or off the target. The resulting raw rates in one set of the scattered-particle detector planes are summarized in Table XII and do not include trigger-level or offline analysis cuts other than the detection threshold and scintillator-bar coincidence requirement as indicated. The background rate from pion beam particles is dominated by their decay products and can be separated from the events of interest by time-of-flight measurements. The background events can be largely suppressed on the analysis level also. For example, the electron induced coincidence rate in one scattered-particle detector for a beam momentum of 115 MeV/c is about 336 Hz for 1 MHz incident electrons. Requiring a z-vertex reconstruction within the target volume reduces this rate to 33 Hz. As all of these particles are of low momentum the background can be further reduced by a cut on the energy deposition in the second, thick, scintillator plane. Figure 44 shows that practically all electrons from the events of interest deposit at least 7 MeV in that plane; requiring a signal of at least 6 MeV reduces the above coincidence rate from 33 Hz to about 5 Hz.

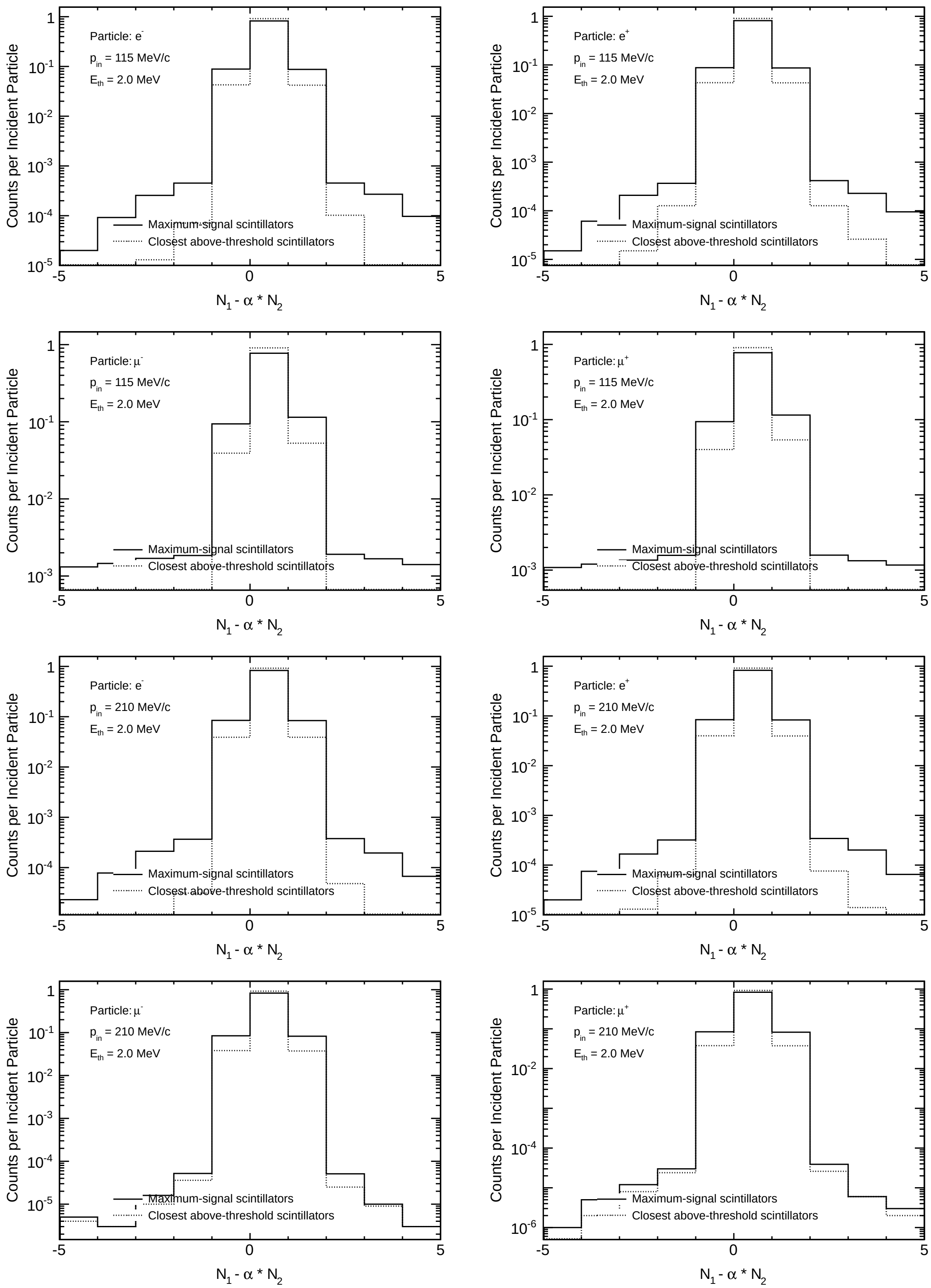

FIG. 47. Paddle number correlation between paddle numbers N_1 and N_2 from the front- and back-wall scintillators, respectively. The factor α is the ratio of the distances from to the target to the scintillator-wall mid-planes. The beam momenta are 115 MeV/c and 210 MeV/c.

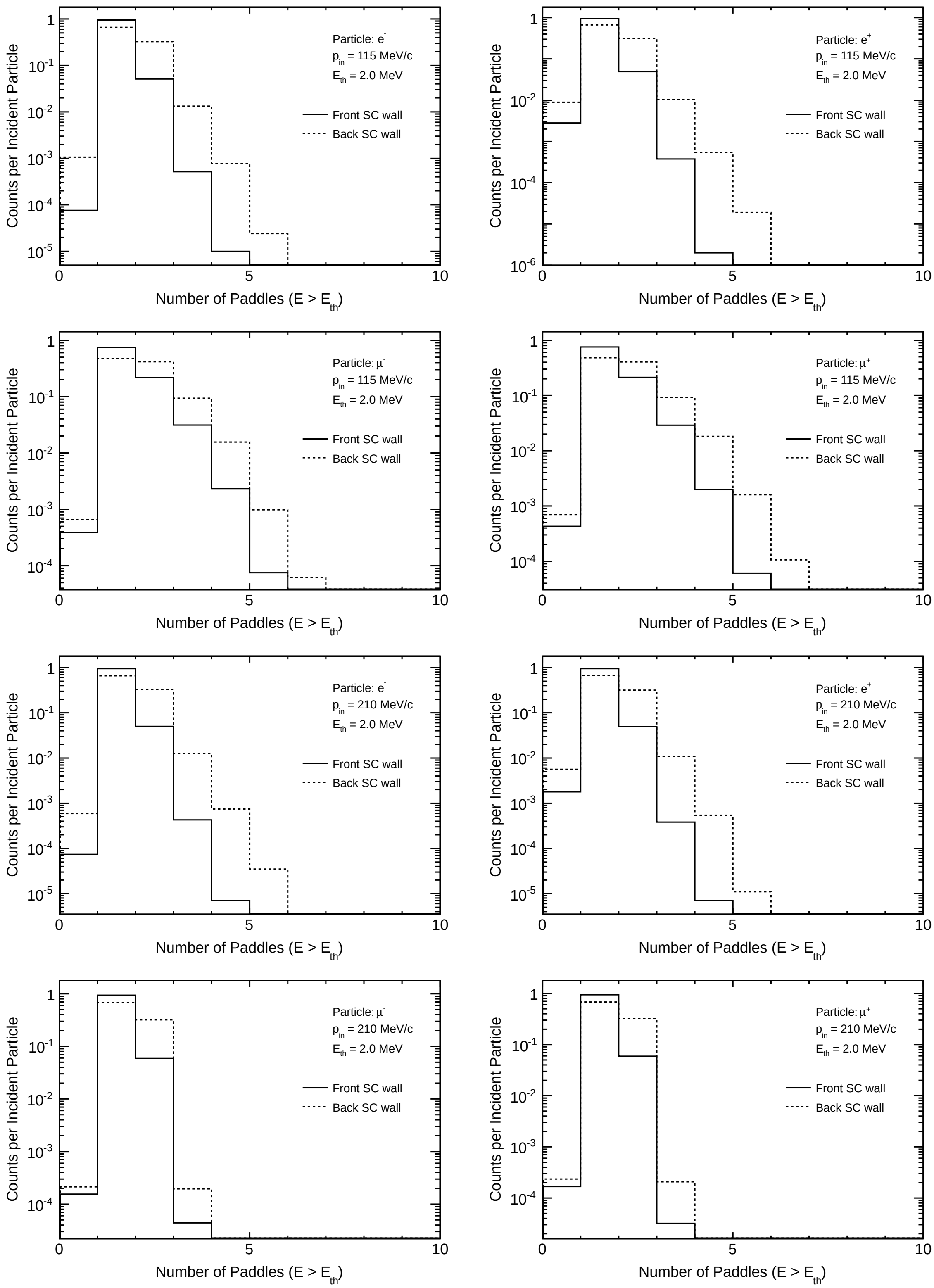

FIG. 48. Multiplicity of scintillator paddle hits in the front- and back-wall scintillators, respectively. The beam momenta are 115 MeV/c and 210 MeV/c.

TABLE XI. Expected average detection efficiency for scattered particles detected in coincidence between the front and back scintillator walls and requiring a three-bar directional cut.

Particle	Beam Momentum	Coincidence efficiency for various signal thresholds			
	(MeV/c)	0 MeV	1 MeV	2 MeV	3 MeV
e^+	115	0.9944	0.9918	0.9902	0.9833
	153	0.9955	0.9934	0.9920	0.9852
	210	0.9964	0.9948	0.9939	0.9874
e^-	115	0.9992	0.9989	0.9987	0.9929
	153	0.9994	0.9992	0.9990	0.9933
	210	0.9996	0.9994	0.9993	0.9937
μ^+	115	0.9991	0.9990	0.9989	0.9989
	153	0.9996	0.9995	0.9995	0.9994
	210	0.9997	0.9997	0.9997	0.9995
μ^-	115	0.9991	0.9990	0.9990	0.9989
	153	0.9995	0.9995	0.9994	0.9994
	210	0.9997	0.9997	0.9997	0.9995

One background that we are continuing to study at this point in time is low energy (10 - 20 MeV) electron recoils at forward angles, $<25°$ that might generate triggers. The rate of these is not large, but they have to be rejected at the analysis level. Most, but not all, of these events reconstruct to positions upstream of the target. Because of the large statistical variations in the energy deposited in materials – see Figure 44 – additional information that allows these events to be rejected is desirable. These events appear to typically have a forward going "high" momentum beam particle that continues into the high-precision beam scintillators after the target, which might by itself be sufficient to remove these events from the analysis. We are also considering a partial third scintillator plane for the most forward part of the acceptance, as these low-energy recoils will be ranged out before the third plane.

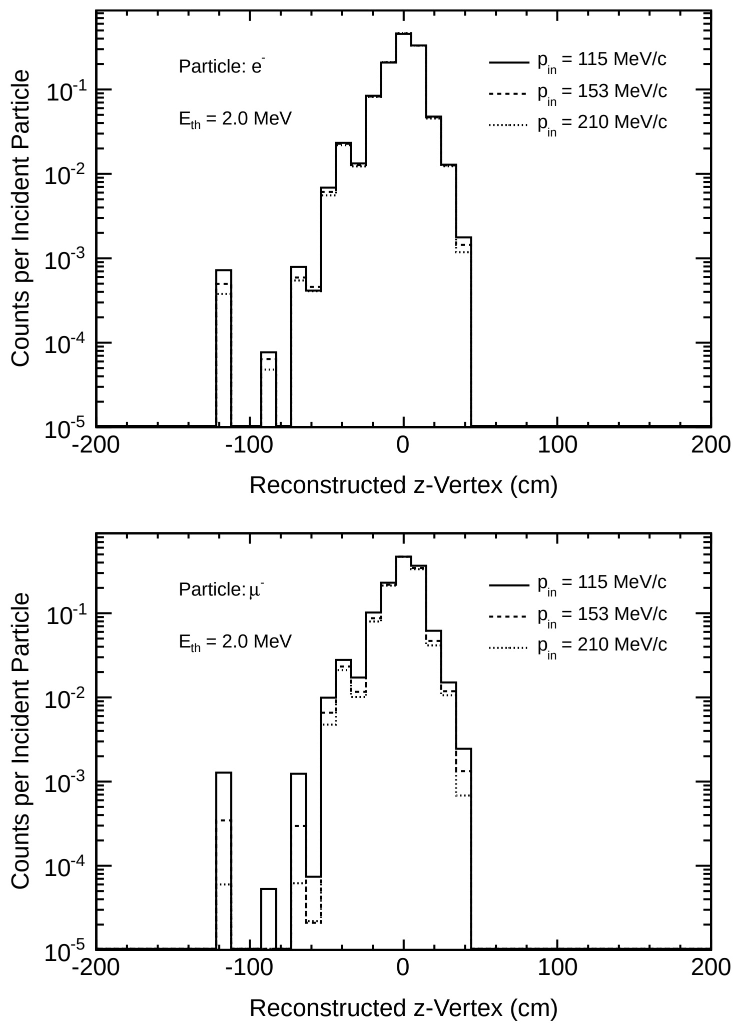

FIG. 49. Simulation of the reconstructed reaction vertex along the beam line, $x = y = 0$, using only the scintillator bars for scattered e^- (upper panel) and μ^- (lower panel), respectively. The distributions are similar for positively charged leptons. Included are all front- and back-wall scintillator paddles with a signal larger than the threshold.

If uncorrected, detection inefficiencies in the scattered-particle detector will lead to errors in the measured cross sections. The average corrections for detector inefficiencies are of the order of 0.1% for $\mu^\pm$ and e^- and is of the order of 0.4% to 0.9% for e^+; see Table XI. These values require a threshold of $E_{th} = 2$ MeV. The positron efficiency is reduced due to possible annihilation processes. The detector inefficiencies show some angular dependence at low scattered particle momentum (backward angles at 115 MeV/c beam momentum);

TABLE XII. Expected rate in *one* set of scintillator walls from beam-particle target-scattering and decay in flight from $z = -1.5$ m before the target to 5 m after the target. Scattering off the target and the effect of shielding as indicated in Figure 4 have been included. Values are given in above-threshold scintillator rate per 1 MHz beam-particle rate with a threshold energy of $E_{th} = 2$ MeV. The coincidence rate includes a three-bar directional cut.

Beam Particle	Beam Momentum	Front Wall (Hz)		Back Wall (Hz)		Coincidence Rate
	(MeV/c)	1^{st} bar	any bar	1^{st} bar	any bar	(Hz)
π^+	115	12996	49468	13637	46797	29467
	153	10920	30910	12637	33259	26446
	210	7255	15739	10022	16778	14470
π^-	115	12972	49336	13604	46787	29468
	153	10958	30901	12683	33330	26483
	210	7368	15913	10118	16921	14598
μ^+	115	95	578	137	819	376
	153	66	413	103	578	276
	210	225	933	203	619	195
μ^-	115	102	575	133	802	387
	153	63	410	95	561	280
	210	218	935	197	618	204
e^+	115	1111	4891	794	1533	254
	153	1133	5019	784	1552	260
	210	1162	5148	828	1641	277
e^-	115	1259	5371	918	1770	336
	153	1262	5408	916	1760	324
	210	1232	5389	904	1760	326

see Figure 45. After correction for these effects, we expect the contribution from the scattered-particle detector to the systematic uncertainties of the absolute cross section to be less than 0.1%. The uncertainty is larger for $e^{\pm}$ cross sections if the threshold can not be kept stable. Because of their very similar detector response we expect the contributions to the systematic uncertainties of relative cross sections for μ^{+} and μ^{-} to be negligible. Also the $\mu^{\pm}$ and e^{-} relative cross section uncertainties should be much smaller than 0.1%.

X. WIRE CHAMBERS

The wire chambers must provide, neglecting multiple scattering, position resolutions of $\approx$100 μm and angle resolutions of $\approx$1 mr, and be aligned to determine the absolute scattering angle to at least 1 mr. They must be able to operate at singles rates of a few hundred kHz, and efficiently detect and track particles that are close to minimum ionizing. Chambers with these capabilities have existed for a few decades.

The construction of the chambers will be led by the MIT group, which has built numerous chambers in the past. The design will be based on the Jefferson Lab Hall A Bigbite wire chambers [47, 48]. The Bigbite chamber construction was led by N. Liyanage of UVa, who initially learned to build chambers as a graduate student with the MIT group.

The Bigbite chambers have been operated in a large acceptance spectrometer with an open geometry at an experiment luminosity of $\approx 5\times10^{36}$/cm^2/s, leading to counting rates of up to 40 MHz/m^2, several times the rates expected in this experiment, while achieving a position resolution $\sigma \approx 100$ μm and a track-finding efficiency of 98%. Figure 50 shows a relatively clean sample event from one of the Bigbite experiments.

These wire chambers consist of three sets of chambers containing more than 3200 wires. The active area of the front chamber is 140 cm $\times$ 35 cm, whereas the active area of the second and third chambers is 200 cm $\times$ 50 cm. Each wire chamber contains six wire planes that are divided into three groups: U, U$'$, V, V$'$, and X, X$'$ wires oriented at +60°, -60°, and +90° to the dispersive direction of the Bigbite magnet. Each chamber plane consists of alternating sense and field wires spaced 5 mm apart, with parallel planes offset by 5 mm. Shifting the second plane by half of the wire spacing helps to remove the left-right ambiguity in the track reconstruction, while having wires in three orientations helps both to remove ambiguities in the case of multiple tracks and to determine a position even if a

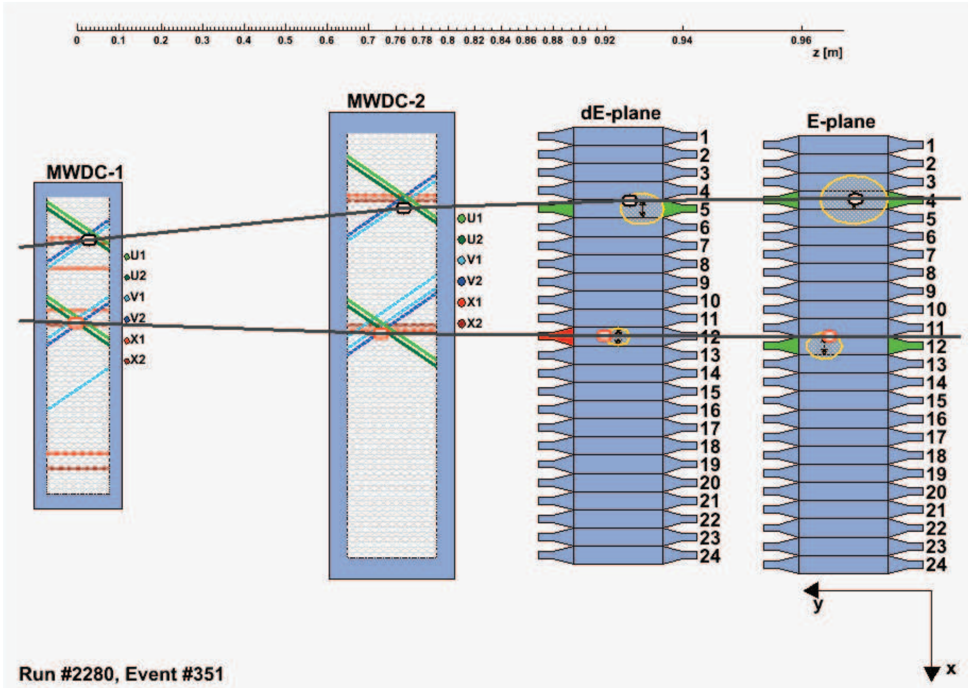

FIG. 50. Event display showing the Bigbite wire chambers and dE and E scintillator planes. In this event two tracks can be seen that fire U, V, and X wires in both chambers shown as well as scintillators in both planes. The scintillator paddle hits are used in the analysis to help determine tracks of interest and reject backgrounds. Several noise hits can also been seen, possibly induced by neutrals due to the large luminosity and open geometry.

wire is inefficient. Cathode planes were placed between the sense-field wire planes, leading to a cell size of 10 mm wide by 6 mm deep.

The chambers were constructed by placing wires on printed circuit boards using precision positioning jigs. Wire positions were confirmed with an optical surveying system using a camera with position controlled by a precision stepper motor (0.5 μm). The resolution of the camera was determined to be $\approx$35 μm.

The Bigbite chambers were operated with a mixture of 50% Argon and 50% ethane bubbled through alcohol. All chambers ran at –1600 V and were read out using new ASIC ("MAD-Chip") amplifier/discriminator (A/D) cards developed by the INFN Padua group, which allows operating the chambers at lower voltages and thresholds compared to old commercial chamber cards from LeCroy and Nanometric. The LVDS outputs of these cards were sent to level translators, which transformed the signal from the A/D cards to the standard ECL format. These signal were then input to conventional LeCroy 1877 Fastbus TDCs.

The wire chambers for the proposed experiment at PSI will consist of three chambers containing UU′VV′XX′ wires, following the Bigbite chamber design. With three chambers in the Bigbite operating conditions, we have found that the hardware tracking efficiency is about 98% from an average wire hit efficiency per plane of about 0.98. This high tracking efficiency is required for the planned precision cross-section measurements and will be monitored throughout the experimental run period. The front chamber will be centered about 25 cm from the pivot with a size of about 40 cm $\times$ 35 cm. The third chamber will be centered about 45 cm from the pivot, so that it is just in front of the first scintillator plane, and will be about 60 cm $\times$ 50 cm. The second, middle, chamber will be positioned about halfway between the other two. Assuming a resolution of 100 μm, and with 20 cm between planes in the first and third chambers, we have at least an intrinsic 0.7 mr angle determination. It is improved by having more than the minimal four planes needed to resolve left/right ambiguities, but ultimately limited on an event-by-event basis by multiple scattering.

The determination of the relative positions of the chambers and the scattering angle via our plan to use the GEM chambers will be discussed in Section XVII.

XI. TRIGGER AND DAQ

A. Trigger

The goal of the trigger system is to efficiently identify and read out scattered e's and μ's, while suppressing backgrounds such as π-induced events, cosmic rays, μ decays in flight, low-energy $e^{\pm}$ from δ rays and Bhabha and Moller scattering, and accidental coincidences.

The main trigger requires both that there is a beam e or μ and a scattered particle signal in the scintillators. The beam PID system described in Section IV identifies efficiently whether there is a beam e or μ. The beam-particle identification strongly suppresses the π background, as discussed in Section II B. A related concern is accidental coincidences. For π-induced backgrounds, the π signal from the beam PID system can limit background read out rates; our intent is to not readout events in which there is both a π and μ or e in the same RF pulse.

We plan to implement the trigger with a commercial FPGA system, the CAEN v1495, since this is a system with which we are familiar from working on its development for the Fermilab E906 experiment; it is also being used for a number of Jefferson Lab experiments. In the Fermilab experiment, the v1495 system is designed for rough tracking through 8 planes of at least 32 scintillator hodoscopes, to determine if there is a high transverse momentum $\mu^+\mu^-$ pair from a Drell-Yan (or J/ψ) event. (Here the trigger is much simpler, as described below.) The v1495 is a VME 6U board. The FPGA has $\approx$20,000 logic elements. It comes with 64 dedicated LVDS/ECL input channels, 32 dedicated LVDS output channels, 2 LEMO I/O channels, and 3 expansion slots for up to 96 additional channels. All channels operate up to at least 200 MHz.

As shown in Section IX, we have two essentially independent experiments, LEFT and RIGHT, each with two planes of scintillators, 17 in the front plane and 27 in the rear plane. With phototubes at each end, we have 176 total signals – roughly half the number of the Fermilab experiment. We plan to use two v1495s, one for LEFT and one for RIGHT, using one expansion slot of each to cover the 88 scintillator inputs, along with the e, μ, and π beam PID signal.

For our main trigger, to identify a scattered particle event we require hits in paddles in both front and rear planes. Identifying a hit requires that the phototubes at both ends of the scintillator fire. The two-plane requirement is because, while a single plane trigger is $\approx$100% efficient, it can misidentify backgrounds such as cosmic rays or low energy particles as valid scattering events. Furthermore, as discussed in Section IX, we can ensure that the particle tracks at least crudely point back to the target by requiring that for a given paddle hit in the first layer the paddle hit in the second layer is one of the three, or perhaps five, directly behind it.

Many needed efficiency studies can be accomplised using accidental coindences with a triggering event. We still expect to have a variety of secondary efficiency triggers including one plane hit which will be read out on a prescaled basis, to keep dead times small. We do not intend to do any particle identification for the scattered particle at the trigger level other than rough time of flight cuts, since all PID at the trigger level can have efficiency issues that might make precise cross sections difficult.

Let us consider the trigger timing in a little more detail. We take as an example the 153 MeV/c setting. The IFP SciFi determines whether a particle is an e, μ or π from its RF time. The particle arrives at the target SciFi about 37, 45, or 50 ns later. A second RF time measurement again determines particle type. The particle after scattering from the target reaches the scintillator planes in another 6, 7, or 8 ns for horizontal scattering, with about ± 2 ns variations depending on scattering angles. While the SciFis have a small active area and only fraction of ns time variations, the rear scintillator paddles are about 2 m long, so light propagation time variations cause the trigger pulse to vary by about ± 3.5 ns. Thus, in the triggering, if we consider for example timing relative to the top rear scintillator phototubes, other scintillator phototubes vary by ± 3.5 ns, and the beam PID signals vary by ± 5.5 ns, with additional 1 ns offsets between e and μ signals from the target SciFi and 8 ns offsets between e and μ signals from the IFP SciFi. These estimates neglect statistical variations in the rise times, which add another ns of time variation to the system – mainly from the SciFi's. Since the SciFi e and μ signals will be input to the trigger on different channels, and the offsets vary with beam momentum, it is simplest to adjust for them in FPGA programming rather then by changing cables. With these timing variations totaling about 2/3 of an RF period, it should not be a problem at the trigger level for each e or μ event to only be sensitive to one π RF bucket being in accidental coincidence.

While only a small fraction ($<10^{-4}$) of the e's and μ's scatter from the target, there is an e or μ in the beam in $\approx$3% - 17% of beam RF buckets. Thus a concern of the experiment is accidental coincidences of background events giving signals in the scattered particle scintillators with beam e's or μ's. These events can all be efficiently rejected at the analysis level, but have the potential to lead to large DAQ dead times at the trigger level, reducing the statistical precision of the experiment. Thus we have decided to veto events which also have a beam π in the same RF bucket. Estimated rates for accidental coincidences leading to read out of processes such as decays in flight, cosmic rays, or π scattering were summarized in Table III.

A μ or e beam particle could give a proper beam signal in coincidence with a cosmic ray through the detector. The cosmic ray rate in vertical scintillator paddles has been measured to be ≈10 Hz, for a total rate in the system of about 1 kHz. This is an overestimate, as a good fraction of the cosmic events are showers which will fire several paddles. A 1 kHz cosmic rate has accidental coincidences with the 1.4 → 8.5 MHz total of e's and μ's at a ≈28 → 170 Hz rate. The actual trigger rate will be smaller than this. The cosmic background is largely single high-energy muons that do not go through both scintillator planes. Cosmic muons that do go through two scintillator planes might not hit paddles that point towards the target. If in practice it is desirable to reduce the cosmic background rate even further, we will study using a multiplicity counter to veto events in which too many scintillator paddles fire, indicative of a cosmic shower. It should be easy to set this up by comparing multiplicity distributions with the beam on and off. Any cosmics read out will be easily rejected at the analysis level: typically they have no track, or it does not point to the target, or the time between the first and second plane of scintillators is backward, etc.

The use of beam PID to veto π-induced events was discussed in Section II A.

Although the trigger described here is relatively simple, as with any complicated trigger its efficiency will need to be evaluated. Its performance can be directly studied using test pulses with various timings to simulate the signals arriving under experimental conditions. Time offsets between various channels can affect the efficiency, but we plan to adopt the approach of E906 and dedicate some of the logic to allow the FPGA to fine tune the input signal timing. Time offsets can be calibrated with data, particularly with electrons at low momenta, as the electron timing does not vary and electrons are dominant at low momenta.

B. Data Acquisition

As discussed earlier concerning the rates shown in Table II, the nominal DAQ rates for this experiment range from about 700 Hz → 5.5 kHz. This rate is high enough that reduced read out rates and statistics from DAQ dead time are a concern. Here we plan to decrease the demands on the DAQ system with two easily implemented techniques, so that the dead times are small and the muon statistics do not suffer.

First, a dual DAQ system would use two separate systems reading out the two detector arms, doubling the rate capability. This has been a common solution we have used for Jefferson Lab experiments with similar issues - two arms both with high rates that we wish to have take data for the same period, with reduced dead time. The dual DAQ is implemented with one DAQ providing a gate needed by the second for the second to take data. The second DAQ is started first, but scalers do not count and triggers are not accepted until the gate from the first DAQ is presented. At the end of a run, the first DAQ is turned off first. As a result, the two DAQs take data for essentially the same amount of time, although offset by a few tens of ns in an of order 1000 s long run. The difference is negligible. In this system, scaler signals can be sent to one system or both; sending them to both systems provides a nice check of systematics.

The second technique involves prescaling certain trigger types. Rates of both scattering events of interest and backgrounds are highest in the forward direction. Since the forward-angle statistics are greater than needed, forward-angle events can be prescaled. Also, the electron rate is generally much higher than the muon rate. Thus we can prescale down the electron triggers and still have better statistics for electrons than for muons. Except for 210 MeV/c, where the electron rate is about 1.5$\times$ the muon rate but the trigger rate is below 1 kHz, the electron elastic scattering rate is 3 - 50 times the μ elastic scattering rate. Thus we can prescale the electron rate by a factor of two or more so that the total trigger rate is no more than 1 - 1.5 kHz, and the number of electron scattering events read out remains a factor of 2 - 10 times the number of μ elastic scattering events read out.

As the collaboration has largely been active within the Jefferson Lab program, and this experiment is similar in many respects to Jefferson Lab experiments, the implementation of the fast DAQ of this experiment with JLab CODA would be fairly easy. However, it appears more difficult to port both CODA and the EPICS slow controls system to PSI than it is for the collaboration to learn and implement the PSI MIDAS system, which already supports the slow controls and standard data acquisition modules. Thus, the collaboration has decided to learn and use MIDAS for the DAQ system.

C. Readout

The needed readout channels for the experiment are:

- The scattered particle scintillators consist of 88 double-ended paddles, leading to 176 bases and TDC and ADC channels. Adding in the beam scintillators we require 180 high-precision TDC channels and 180 ADC channels. Since these scintillators have ≈50 ps resolution, ≈25 ps TDCs are needed.

- The beam SciFi detectors have 256 fibers at the IFP and 85 fibers at the target, leading to 682 channels of ADC and TDC. The SciFi resolution is ≈1 ns, so 0.5-ns level TDCs are sufficient.

- The GEM chambers have their own standalone DAQ system, which exists. It will be necessary to implement readout of the GEM data into the data stream.

- The scattered particle wire chambers have a total of about 2500 wires, requiring the same number of TDC channels with ns-level resolution.

In a semi-modern DAQ system with 32 channels per module, we would require 6 high-precision TDCs, 100 low precision TDCs, and about 27 ADCs, plus some spare modules. These modules could be housed in 7 - 10 crates.

A perfectly clean 100% efficient event would have 10 hits from the 5 SciFi planes, 18 hits from the 18 wire chamber planes, and 4 hits from the two planes of scattered particle scintillators, leading to 32 TDC signals and 14 ADC signals. With ≈100 ns gates for ADCs and TDCs, there is typically 1 background beam particle, which typically neither scatters nor decays – the total rate of scattered particles is only a few percent of the beam rate – leading to 10 more ADC and 10 more TDC signals. Thus it appears that with zero suppression event sizes are less than 1 kB, and the data rate will be of order 1 MB/s. This data rate is small for any modern data acquisition system, and not a problem to record with modern networks, computers, and disk drives.

The anticipated trigger rate is of order 1 kHz. Since the event sizes are small, the dead time associated with this trigger rate is hard to determine at present; it depends mainly on the conversion and readout times of the electronics modules used in the DAQ, which have not yet been identified - we hope to loan spare electronics rather than purchase or construct new modules, and the available electronics will depend on when the experiment runs.

In addition to the event readout, it is necessary to have scaler channels to count the number of pulses in the scintillator phototubes. This is useful for the 180 channels of scattered particle scintillators and downstream beam monitors, and necessary for beam normalization with the 682 channels of beam SciFi. In addition, a small number of channels are needed for counting ORs of the plane-by-plane SciFi response, the beam PID system outputs, and the various trigger types. Assuming 32 channel scalers, 28 are needed. Scalers do not need to be read out often, and increase the total data rate very little.

Consequent with the relatively modest DAQ requirements which can be met with fairly straightforward techniques, the collaboration has not to date focused on details of the DAQ system. Our intent is to develop more detailed plans during fall 2012 as we work on test measurements at the πM1 channel.

XII. RUN PLAN

After the initial installation and commissioning of equipment, described in Section XVII, data taking can commence. We plan on a series of data runs interspersed with various calibrations, described in Section XVII C.

Based on estimated beam fluxes, cross sections, and efficiencies, the run requires about 6 months of beam time. Because of uncertainties in the beam fluxes, we have not at this point tried to optimize the division of time between the various measurements, we have instead simply opted for 1 month of time at each of the 6 settings: 3 beam energies $\times$ 2 beam polarities. Once the fluxes and background rates are better established, the optimal division of beam time can be established.

Because we are attempting a high-precision cross section measurement, it is possible that issues will arise that require some modifications in our approach. As a result our plan is to perform one of the six kinematic settings in one month of beam time, and to extensively analyze the data during a 1-2 month period before continuing the experiment. The order of the kinematic settings will be decided after the fluxes are determined in the fall 2012 test run.

XIII. DATA ANALYSIS

Here we discuss various steps in the data analysis leading to the raw cross sections. The data analysis will have as input the various ADC and TDC signals from the detector along with trigger and beam PID information determined at the hardware level. From these raw data, we will do the following:

- The IFP SciFi timing will be analyzed with ADC corrections to the TDC values. Generally both planes should fire so the IFP timing is improved by more than a factor of $\sqrt{2}$ over the hardware result. With multihit TDCs, it will be possible to determine the PID and momentum of the triggering particle and background particles, as long as the background particles are from other RF buckets.

- The target SciFi TDCs will be similarly analyzed to the IFP TDCs. In addition for each particle a position in the target SciFi array will be determined. The three planes of the target SciFi will allow an improvement in timing of around $\sqrt{3}$.

- The combination of IFP and target SciFi's will allow the time of flight of the beam particles to be determined. The e-μ time differences range from 4.3 - 13.0 ns at the three beam momenta, while the μ-π time differences range from 3.0 - 8.0 ns.

- The GEM data will be analyzed to find the real tracks between the three chambers and remove ghost tracks. The GEM data also provide crude timing information. The GEM tracks will point to positions at the target SciFi array and at the target.

- The GEM and target SciFi comparison of times and positions allows the triggering trajectory to be determined.

- The downstream high-precision scintillator will record accidental coincidence hits from non-triggering beam particles. These will generally be offset from other RF buckets. These data will be used to build up an RF time spectrum that will allow continuous monitoring of the beam momentum and / or RF time changes.

- The scattered particle scintillators will be analyzed similarly to the SciFi array. The analysis is basically the same, though much higher in precision. The analysis also determines a position along the paddle from the difference in time between the phototubes at the ends of the bars. Spectra of ADCs and paddle differences between the two planes will allow simulations to be checked. The position in the scintillators allows a consistency check with the wire chamber track.

- The wire chamber TDC data will be corrected for offsets, used to determined drift distances, and used to generate a track. There are sufficient extra planes that the track can be found even if some hits are missing, allowing the wire efficiencies to be determined. The track found will project to the target and to the scintillators. The projection to the scintillators can confirm the consistency of the trigger with the generated track.

- The GEM and chamber tracks combined determine the target interaction position, the scattering angle, and also a distance of closest approach - generally the two tracks do not actually intersect. Cuts can be applied on these quantities to remove nearly all the events from particle decays in flight, or scattering from the last GEM, for example.

- The RF time determined from the scintillators can now be corrected for the flight path.

At this point relevant quantities have been determined, cuts can be applied, and counts can be summed up.

A. Removing Backgrounds

The estimated rates of the desired elastic scattering and background processes were estimated earlier and summarized in Table II. Backgrounds are mainly removed through target reconstruction cuts and timing cuts. The timing cuts are enhanced by considering path length corrections using trajectories measured in the wire chambers and taking into account the momentum of the beam particle measured at the IFP, which leads to measurable changes in β and RF time. In principle dE/dx cuts are possible – and they are of course made in setting scintillator thresholds – but the π's, μ's and e's in this

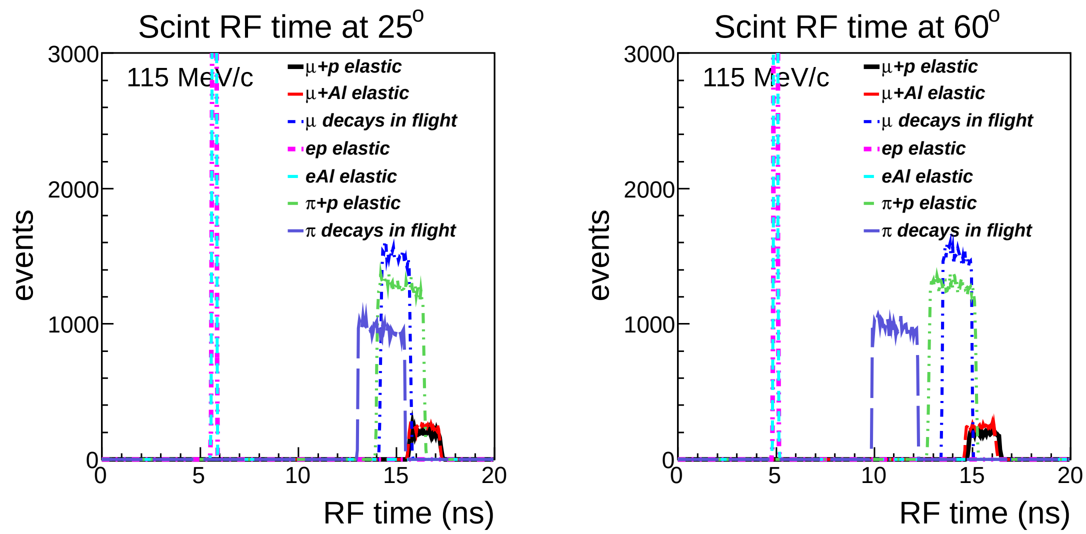

FIG. 51. RF time distributions at the scattered particle scintillator for a beam momentum of 115 MeV/c. Results are for particles from the region of the target, and are shown for two choices of the angle as the path length and thus RF time vary with angle.

experiment are all close to minimum ionizing, and will not be resolved with dE/dx cuts alone. Finally, residual backgrounds can be subtracted by measuring and subtracting the background rates.

1. *RF Timing Cuts*

Previously, we studied the ability to identify particles at the trigger / hardware level using the RF timing in the beam IFP and target SciFi arrays. The results were shown in Figures 16, 17, and 18, and the statistics of particle identification were summarized in Table V. These results were based on a signal from a single plane of the two in the IFP SciFI array and of the three in the target SciFi array. At the analysis level, the beam RF timing is improved by roughly a factor of $\sqrt{2}$, and consequently the beam SciFi detectors provide improved beam particle identification in the analysis.

In Table II we summarized expected rates for the desired μp and ep elastic scattering reactions as well as for several background reactions. Particles, and to some degree reactions, can be further identified through RF timing with the scattered particle scintillators.

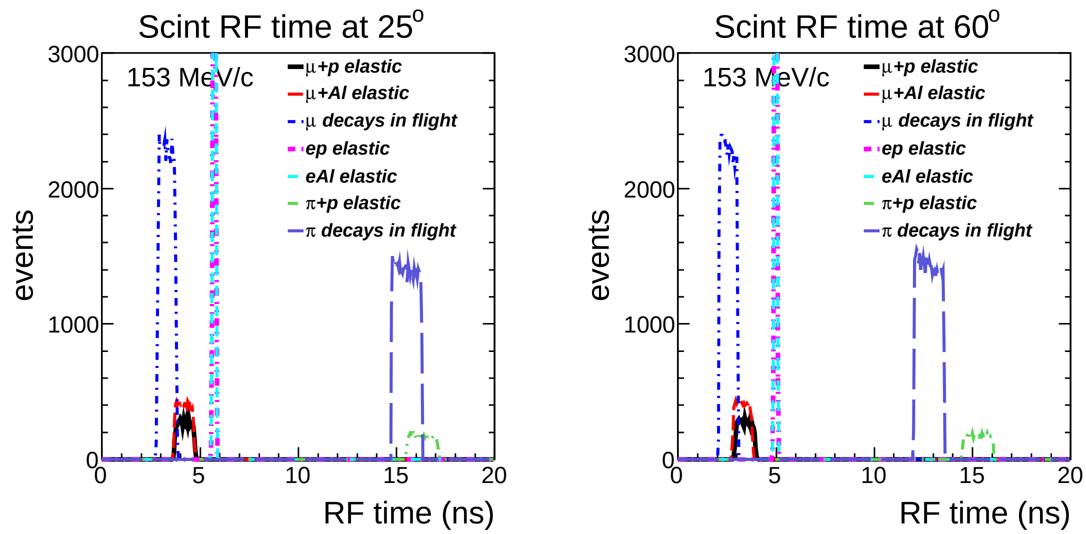

FIG. 52. RF time distributions at the scattered particle scintillator for a beam momentum of 153 MeV/c. Results are for particles from the region of the target, and are shown for two choices of the angle as the path length and thus RF time vary with angle.

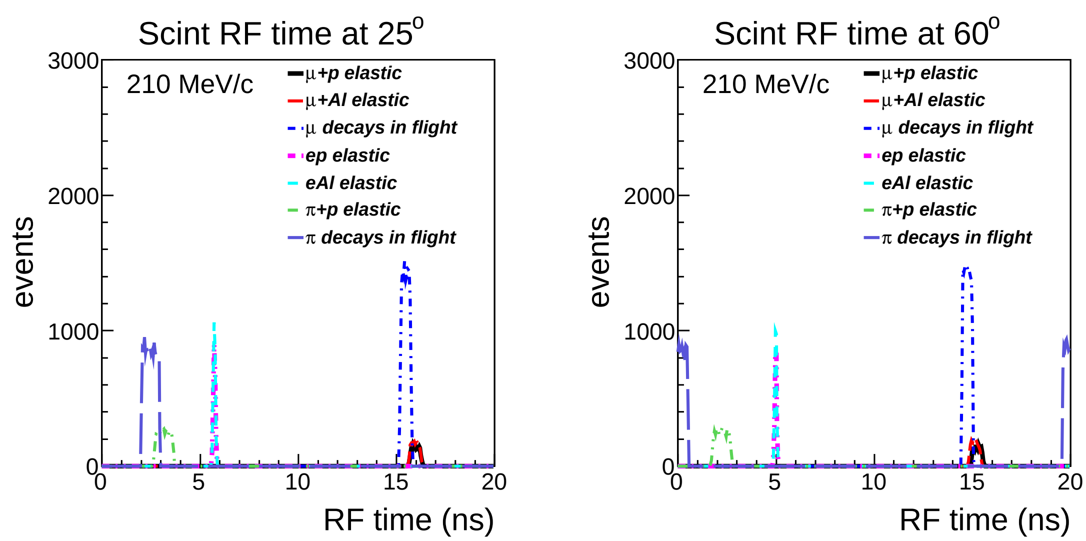

FIG. 53. RF time distributions at the scattered particle scintillator for a beam momentum of 210 MeV/c. Results are for particles from the region of the target, and are shown for two choices of the angle as the path length and thus RF time vary with angle.

Figures 51, 52, and 53 show simulated RF time spectra in the scintillators for the desired μp and ep reactions as well as a number of background reactions. The relative numbers of electron- and muon-induced events are roughly based on the rates given in Table II, while the number of π-induced events is arbitrary. Several conclusions can be made from these spectra.

- Electron events, ep and eAl elastic scattering, can be distinguished from all other events, but all electron events occur at the same time, as $\beta_e \approx 1$. (The $\approx$MeV/c Moller and Bhabha recoils do have $\beta \approx 0.9$.) The widths of these distributions largely reflect the scintillator timing resolution, so the electrons serve to calibrate the scintillator timing.

- The μAl and μp elastic distributions also overlap. The difference in momentum of the scattered muons from the two targets is not sufficient to create a measurable RF time difference, so these reactions cannot be distinguished. The widths of these distributions largely reflect the variations in β_μ due to the 3% momentum bite of the πM1 channel.

- The background decay in flight of μ's, e.g., $\mu^- \rightarrow e^- \overline{\nu}_e \nu_\mu$, leads to a trigger rate about 100 times larger than the elastic scattering rate. Here we show a reduced rate of decays corresponding to decays in the region of the target. Since the decay e has $\beta \approx 1$, the RF time distribution of these events shifts to shorter times. Although the tail of the decay distribution overlaps the μ elastic scattering distribution, the distributions are separated in two-dimensions looking at RF time vs. beam momentum. Figure 54 shows the correlation between beam momentum relative to central channel momentum and RF time in the region of the μ events, to show how the μ decays can be separated. Not shown are the μ decays upstream of the target, which are rejected by reconstructed target position cuts. These events have a shorter flight path to the scintillators, so their RF time distribution is shifted further.

- The πp elastic backgrounds are largely suppressed by the beam SciFi RF timing. Any residual events are largely well separated by the beam scintillator RF timing, although again a 2-dimensional cut on RF time vs. beam momentum is needed at

115 MeV/c, as shown in Figure 55. Although the μ elastics and π decays can be well separated, the π elastic scattering and μ decay backgrounds run into each other due to the different slopes of β vs. momentum. It is only needed to reject both, so this is not an issue.

- The decay of π's, e.g. $\pi^+ \to \mu^+\nu_\mu$, is shifted compared to πp elastic scattering to earlier times. The shift grows larger as the scattering angle increases. The difference is largely due to geometry as $\beta_{decay\,\mu} \approx \beta_\pi$. The maximum angle for the decay μ's relative to the π's in the beam is about 20°, 15°, and 11° for the three beam momenta of 115, 153, and 210 MeV/c, respectively. Thus the decay μ's going into the scintillators come from π decays far upstream that have shorter flight paths to the scintillators. The minimum distances upstream, corresponding to the maximum angle decays, are given in Table XIII. All of the π decays lead to tracks in the chambers that do not point back to the target, and the decays at higher energies or into larger angle detectors occur far upstream of the target, so that they do not give signals in the target SciFi detector or GEM chambers. These results suggest that shielding around the beam line can dramatically reduce the rate of μ's from π decays in the detectors.

TABLE XIII. The minimum distance upstream of the target that a π must decay to lead to a decay μ in selected scintillator paddles.

Momentum (MeV/c)	115	153	210
Minimum distance (m) for 25° scintillator	0.5	1.0	1.7
Minimum distance (m) for 60° scintillator	2.1	3.0	4.3

To summarize, we have demonstrated that with the 50 ps (σ) resolution of the South Carolina scintillators, it should be possible to uniquely identify elastic electron and muon scattering events from the target. This result is largely independent of information from any other detectors, though the beam SciFi detectors also identify beam particle types.

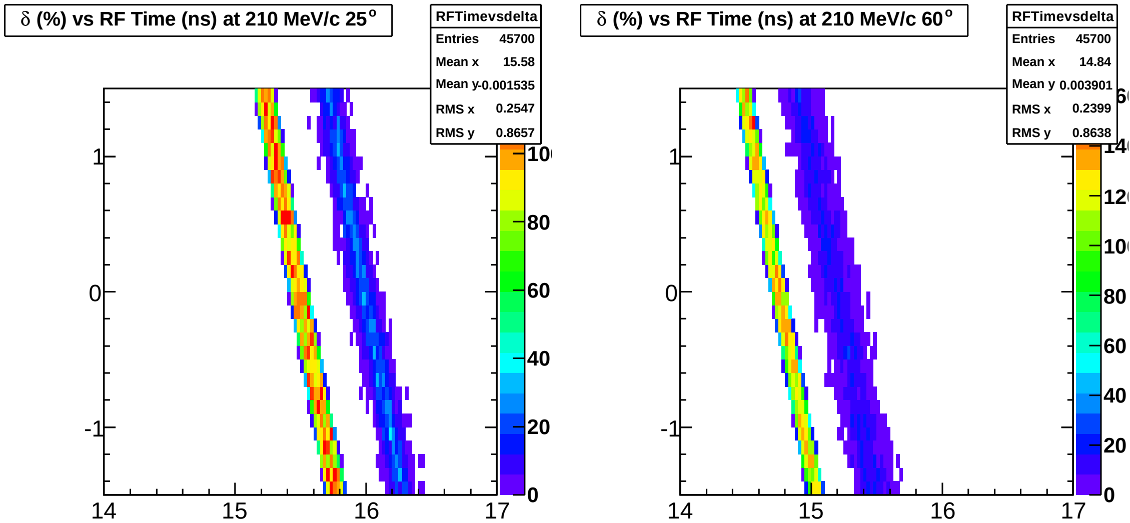

FIG. 54. Momentum vs RF time correlation for two angles at a beam momentum of 210 MeV/c, focusing in on the RF time region of μ decays in flight (left band) and μ elastic scattering (right band).

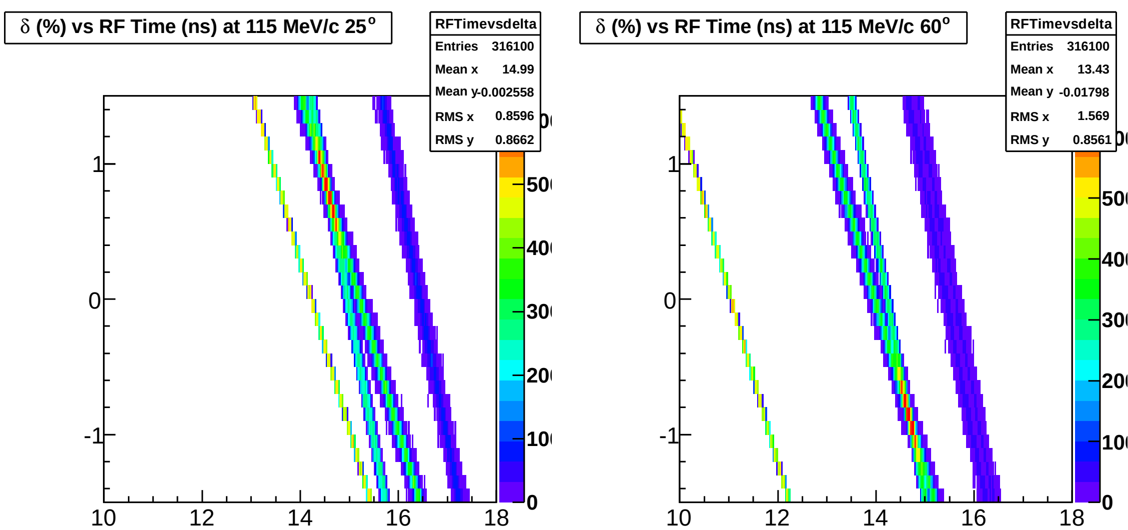

FIG. 55. Momentum vs RF time correlation for two angles at a beam momentum of 115 MeV/c, focusing in on the RF time region of μ and π interactions. The left band is π decays in flight, the right band in μ elastic scattering, and the crossed bands in the center are μ decays in flight and π elastic scattering.

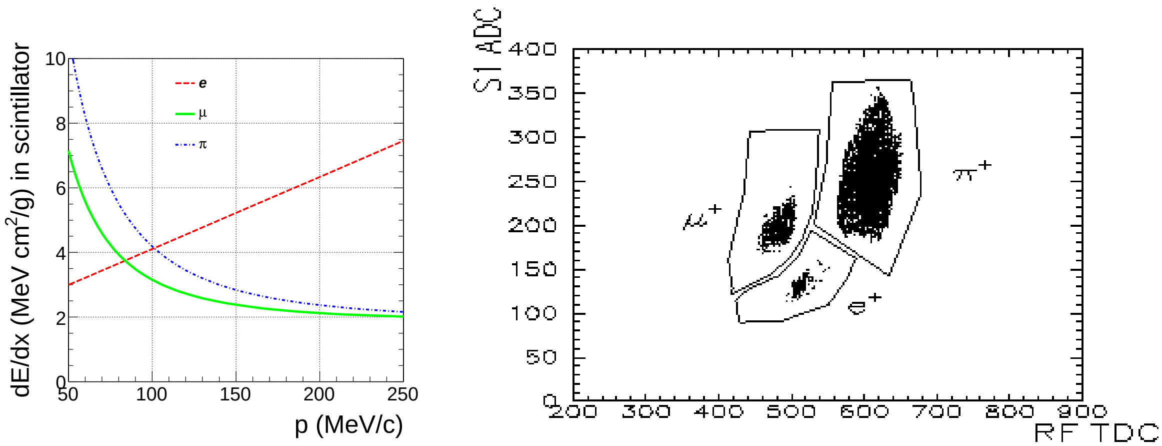

FIG. 56. (Left) Calculated energy losses of particles in scintillator as a function of momentum. (Right) ADC signal (energy loss in scintillator) vs RF time from the PSI PIBETA experiment. The measurement was done in the mid 1990s with a 3 mm thick scintillator and 116 MeV/c beam in the πE1 channel. This figure was taken from the PIBETA webpages at `http://pibeta.web.psi.ch/docs/publications/ketevi_diss/node19.html`. While the calculated and observed ratios of π to μ energy loss agree well, the electron is calculated to have ≈20% more energy loss than the π, but instead has ≈50% less.

2. Energy Loss Cuts

Determining energy loss in thin scintillators is an established technique for particle identification. However, the statistical variations in energy loss prevent it from being a clean method of identification. Figure 56 shows calculations of energy losses in scintillator along with an experimental result taken at a beam momentum very close to our lowest beam momentum. The calculated energy losses are based on the NIST ESTAR and PSTAR range and energy loss tables at `http://physics.nist.gov/PhysRefData/Star/Text/ESTAR.html` and `http://physics.nist.gov/PhysRefData/Star/Text/PSTAR.html`.

As discussed above, particle identification with RF timing appears entirely adequate for this experiment. Scintillator pulse height measurements are not needed for particle identification, though they are needed for corrections to the RF timing determination, are useful to monitor consistency of performance, and might be of some help if there are unanticipated backgrounds. (We expect to study our understanding of backgrounds during the planned fall 2012 tests.)

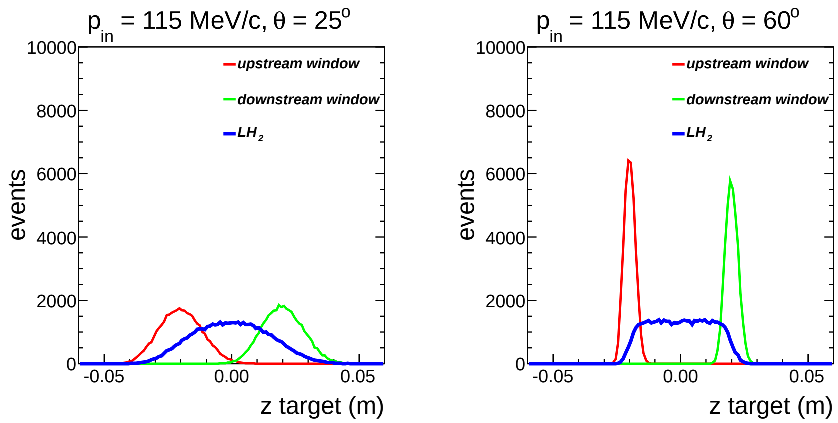

FIG. 57. Reconstructed interaction position along the beam line for two angles at a beam momentum of 115 MeV/c.

3. Target Reconstruction Cuts

Determining the interaction point suppresses backgrounds that do not come from the target. Figures 57 and 58 show a simulated reconstructed image of the target along the beam line. In these plots the relative numbers of events are from Table II, but the absolute numbers are arbitrary. The simulation included multiple scattering in the final GEM chamber, the vacuum and target entrance windows, the liquid hydrogen, the target and vacuum exit windows, and an estimated resolution (including multiple scattering) of the wire chambers. The simulation uses a target cell 4-cm long by 4-cm diameter, with a 0.125 mm kapton wall and 0.1 mm of superinsulation. The interaction position is found from the "intersection" of the incoming ray measured by the GEM chambers with the outgoing ray measured by the scattered particle chambers. We use the technique common to proton polarimetry measurements [49] of using the center point of the common perpendicular to the two rays as the interaction position – in general the two rays do not intersect, but the common perpendicular is the closest to intersection. The simulation does not include the effects of energy slightly increasing multiple scattering as the particles propagate through the detectors and target, or the curvature of the target windows.

The results shown in Figures 57 and 58 indicate a strong angle dependence to the target reconstruction but a weaker beam momentum dependence. The distance of closest

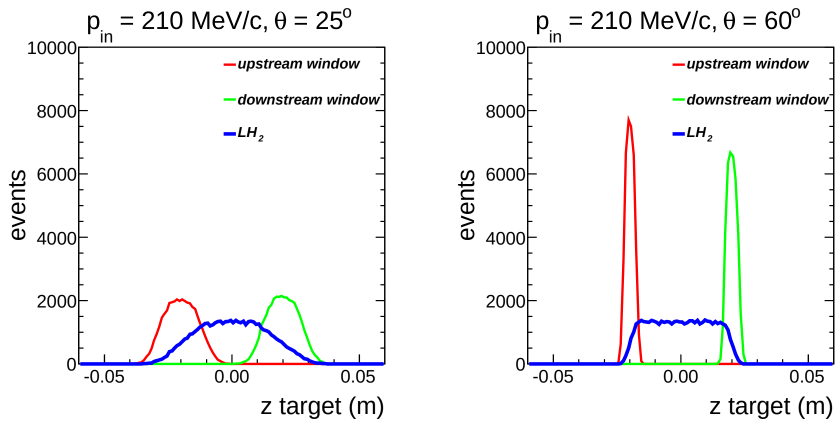

FIG. 58. Reconstructed interaction position along the beam line for two angles at a beam momentum of 210 MeV/c.

approach of the two rays appears to be angle independent, so the angle dependence largely results from the sinθ apparent shortening of the length of the target rather than any significant difference in the multiple scattering with angle. At smaller angles, it will be necessary to measure the scattering rates from a dummy target and perform subtractions of the elastic end-window scattering events. At larger angles, it might be possible to achieve a smaller total uncertainty with z-target cuts, to limit the number of end window events that need to be subtracted, but here we simply assume that these subtractions will be done.

Having to measure and subtract backgrounds increases the statistical uncertainty about a factor of two. It is conventional to use a dummy target with thicker foils than in the actual target, to match the thickness of the dummy in radiation lengths to the thickness of the target. For the 4-cm target with 0.125 mm windows, this leads to dummy foils about 6 times thicker than the target walls. As shown in Figure 6, the background carbon elastic scattering rate averages about 0.3 times the signal H elastic scattering rate and decreases with increasing scattering angle. With this ratio, uncertainties are optimized by measuring the signal + background for ≈75% of the beam time, and the background for ≈25% of the beam time. The optimization shows a shallow minimum, and the uncertainty increases by roughly a factor of 1.4 at all angles, for constant beam time.

The background subtraction can be based on absolute luminosities. It can be cross checked particularly at the larger angles through the z-target distribution shape, as the hydrogen is about flat near the center of the target and the window peaks are clearly visible.

XIV. RADIATIVE CORRECTIONS

Radiative corrections procedures for electron-proton scattering are well established. However, there are several issues that must be accounted for in this experiment.

- The large mass of the muon compared to the electron significantly reduces the bremsstrahlung corrections, which yield the largest correction. However, many implementations of radiative corrections work in the ultra-relativistic limit, where the lepton mass is considered to be negligible compared to Q^2, and this is a poor approximation for muon scattering. However, the formalism commonly used in radiative corrections at Jefferson Lab [50] does not make this approximation, and is well suited to muon scattering.

- The peaking and extended peaking approximations, where radiated photons are assumed to be emitted only in the direction of one of the charged particles, is also not as appropriate for the low energies of the proposed measurements. Ingo Sick provided and tested a version of the radiative correction procedure used in our simulation that does not apply the peaking or extended peaking approximations [51]. Afanasev *et al.* [52] provided a calculation that was previously used in the analyses of polarized electron scattering at Jefferson Lab. Their calculation does not use the peaking approximation or soft-photon approximation.

- Coulomb corrections and hard two-photon exchange (TPE) contributions cannot be calculated with the same level of precision as the other contributions. While bremsstrahlung by electrons is enhanced due to a small electron mass, two-photon exchange is independent on the lepton mass in an ultra-relativistic case. For lower energies considered in this experiment, terms that do not conserve lepton helicity become important in the scattering amplitude, especially for the muons. To date, there has not been sufficient low Q^2 data with enough precision to require that the full structure of the amplitude of lepton-proton elastic scattering be considered, with the data analyzed in terms of six generalized form factors (instead of the three form factors used in phenomenological analysis of TPE corrections in ultrarelativistic electron scattering). This issue will again need to be studied in this experiment. Some information about these lepton-helicity-violating amplitudes can be obtained from single-spin transverse beam asymmetries at small Q^2 – see the QWeak report at `http://www.jlab.org/conferences/ugm/Tuesday/wdeconinck_qweak_ugm2012.pdf`.

- At very low Q^2, calculations within a hadronic framework [39, 40, 53] are typically expected to be more reliable, and are in good agreement with a low Q^2 TPE expansion [54], which is expected to be valid up to Q^2=0.1 GeV^2 and so covers our entire Q^2 range. However, even at low Q^2 the loop integral is over infinite momentum range and two-photon exchange is not precisely understood. Theoretical models show the trend that TPE has a smaller effect at lower Q^2. It can be understood since hard TPE amplitudes do not have a $1/Q^2$ Coulomb singularity, as opposed to the Born amplitude.

- TPE corrections for muon scattering are being performed, and the comparison of the positive and negative leptons will allow for a test of the TPE calculations for both electrons and muons, while the average of the different-signed lepton results will allow for an extraction of the electron and muon scattering cross sections where all charge-dependent corrections cancel.

To summarize, while radiative corrections are standard and well-established in electron scattering, care must be taken in this experiment that the radiative correction calculations are correctly implemented without invalid approximations. Parts of the radiative corrections are expected to be suppressed for muons due to the larger muon mass. Two-photon exchange corrections are generally expected to be small, and should be similar for electrons and muons. However, two-photon exchange remains more poorly understood than one would like.

XV. SYSTEMATICS

In this section we summarize the systematic uncertainties.

The cross section depends on knowing the numbers of beam particles, target nuclei, and scattered particles. To know these numbers we also have to know detector efficiencies, trigger efficiencies, DAQ live time, and analysis efficiency (cuts, particle identification, and track reconstructions). We need to know / study possible kinematic offsets and their effects. Finally, we need to understand theoretical corrections such as Coulomb and radiative corrections. We also need to consider absolute vs. relative efficiencies.

Counting the beam particles with the SciFi arrays and FPGA system was discussed in Section IV. The efficiencies for determining the numbers of electrons and muons are high, and the probability of misidentifying a particle as an electron or muon is very small, as summarized in Table V. With the expected beam fluxes, the estimated contribution of misidentified particles is at most at the level of a few tenths of a percent. As discussed, these probabilities can be calibrated, and the measured fluxes can be corrected. The important thing is that the beam PID signals sent to the scalers to be counted are also the signals sent to the trigger to enable taking events; in this case any inefficiencies cancel. As a result, we estimate that the relevant fluxes can be determined to the 0.1% level absolute. There is no uncertainty for a given angular distribution, but the 0.1% is also a reasonable estimate for the relative uncertainty for different polarities or beam momenta.

The GEM chamber efficiency must be known, as the flux of incident particles is determined by the SciFi array, but if the particles are not tracked by the GEMs they cannot be analyzed, changing the cross section. But the GEM chamber efficiency can be well determined with high statistics from accidentals in the data. With 10 MHz beam we expect in a $\approx$100 ns window about 1 background beam particle in each event. Generally the background particle will give a signal in the target SciFi array and the downstream high-precision scintillator, hence it must have passed through the GEMs. These background particles will be tracked by the GEMs, and the GEM efficiency will be precisely determined. Similarly, it will be necessary to put fiducial cuts on trajectories of particles in the tails of the beam that are heading near the target cell side walls. But these events are counted in the scalers as contributing to the beam flux. The analysis of accidental coincidences will allow us to determine for each particle type the fraction of the beam that does not pass the fiducial cuts, and allows us to correct the beam flux for these events.

The systematic uncertainties concerning the target thickness were discussed in Section VIII. The relative uncertainties in the target thickness should be small, ≈0.1%, as long as the target cools for several hours before use to convert to the para spin configuration and as long as its operational temperature and pressure are about constant. Operational data will be needed to estimate this uncertainty. There will be an absolute uncertainty of up to ≈1% related to knowledge of the target length, which is affected by the target position and the beam distribution over the target as well as the length and equation of state. If the beam conditions vary with time, or the beam distribution over the target varies with polarity or momentum or type of particle, the relative systematic uncertainty between these settings could be larger than ≈0.1%; this will require data to evaluate.

The number of scattered particles depends on knowing the efficiencies of the scattered particle scintillators and wire chambers well. Scintillator efficiency simulations were discussed in Section IX. The scintillator efficiencies were large, with only a few tenths of a percent inefficiencies for most particles, but about 1% inefficiencies for positrons. Energy and angle variations are mild. We have not evaluated uncertainties in the simulation, but the agreement between the energy losses observed in cosmic tests and the simulated energy losses suggests the absolute and relative uncertainties are small, as long as the discriminator threshold is under control. We do propose in Section XVII a direct test of the scintillator efficiencies with the beam.

Associated with the scintillator efficiency are uncertainties from dead time at the hardware level. The highest rate in any scintillator paddle, based on the simulations shown in Table XII, is about 100 kHz in the most forward paddle. Rates in other scintillators are less. This leads to a dead time of 0.2% or less, and consequently a small uncertainty on the correction.

The wire chamber efficiencies were estimated to be 98% for individual wires and 98% for track reconstruction. The individual wire efficiencies can be monitored from the events in which tracks are found. Determining the tracking efficiency from the data is more of an issue since some triggers will not come from particles passing through the chambers.

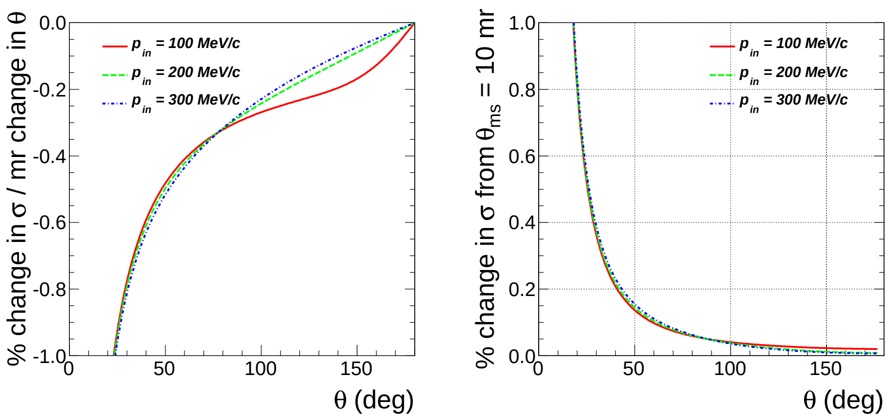

FIG. 59. Left: change in cross section from a +1 mr offset in the scattering angle. Right: change in the cross section from multiple scattering. Estimates were done with the Kelly form factors.

In Section XVII, we indicate how the chamber efficiency can be quantified during the calibration period. As indicated in Section II A, the rates in the chamber are modest, and as long as high voltage and gas mix are stable the chamber performance should be highly efficient and stable as well. Thus, we expect that the systematics of wire chamber efficiencies are minimal.

The beam momentum was presented in Figure 20. As discussed in Section V, we expect to be able to determine the particle momenta distribution to better than 0.1% in calibrations with material put at the IFP, but slightly worse than this with the actual detectors in place. Averaging over the distribution of incoming momenta has a relatively small effect, and the angle-to-angle variation is small.

The angle sensitivity due to offsets and multiple scattering were presented in the proposal. Figure 59 shows how the cross section changes from offsets in the central angle and from multiple scattering leading to averaging over scattering angles. The effects are similar in magnitude. The estimated precision in the central angle determination is 0.5 mr – see Section XVII. Further study is needed to determine if this can be improved using the overlap of data at difference beam momenta. Since the multiple scattering effect is similar at all energies, we should be able to correct the data for it. However, for our purposes here we conservatively estimate each of these effects leads to a 0.5% overall systematic and a

0.3% point-to-point uncertainty.

In determining the number of counts it is also important to – here we adopt a simple viewpoint - determine the acceptance of each kinematic bin. The bins are determined by the wire chamber reconstructions. By putting the cuts for the analyzed data within the active area of the chamber, in leading order the number of events in- vs. out-scattering – perhaps we should say mis-reconstructing – cancels. The major effect is the multiple scattering effect from the strong variation of cross section vs. angle, which we have accounted for. Thus the main question here is the precision of knowing the size and position of the chambers. The accuracy of wire position is at the level of 35 μm at a chamber to target distance of order 30 cm. This corresponds to an solid angle uncertainty at the level of $2{\times}10^{-4}$, or 0.02%. The uncertainty in distance of the chamber from the pivot point is determined by manufacturing of the chamber and the table on which it and the GEMs are mounted – since it is really the GEm vs. chamber positioning that is important. These distances should be at the level of 100 μm out of 30 cm, for a solid angle uncertainty of about $7{\times}10^{-4}$, or 0.07%. The point-to-point uncertainty will be smaller.

The uncertainties on the radiative corrections need to be more closely studied before we can confidently quote a systematic uncertainty. It will require re-examining the codes to make sure that neither of the usual approximations, the high-energy limit $Q^2 >> m^2$ or the low energy limit $m^2 >> Q^2$, is present in the codes to be certain the limits are correct. Even so, for the time being we estimate the uncertainty as 0.5% for both relative and absolute uncertainty, and this uncertainty largely comes from the two-photon exchange mechanism. According to current theoretical estimates, there are negligible differences between two-photon exchange for e's and μ's – this will be tested in the measurements – so in the ep to μp comparison the radiative correction uncertainty is very conservative.

The uncertainties described above are summarized in Table XIV.

There are additional effects that are hard to evaluate at present, but which will affect the ultimate systematic uncertainty. One is the stability of the results with time. Unstable power supplies and varying electronics temperature for example can lead to efficiency variations. While many parameters can be monitored by slow controls, we cannot be sure there are no issues until we see in the data that there are only normal statistical fluctuations. A second effect is the sensitivity of the analysis to cuts. We have argued

TABLE XIV. Summary of systematic uncertainties on the cross section. The Total uncertainties result from adding the individual uncertainties in quadrature.

Systematic	Relative Uncertainty (%)	Absolute Uncertainty (%)
beam flux	0.1	0.1
GEM efficiency	<0.1	<0.1
target thickness	0.1	1.0
scintillator efficiency	0.1	0.1
wire chamber efficiency	0.1	0.1
beam momentum sensitivity	0.1	0.2
angle determination	0.3	0.5
multiple scattering	0.3	0.5
solid angle	0.1	0.1
radiative corrections	0.5	0.5
Total	0.7	1.4

in this report that backgrounds are small, and assuming Gaussian variations we find for example that timing peaks of particles are well separated, and cuts can be cleanly done. But often in practice there are non-Gaussian tails, and their effects must be evaluated from the data.

XVI. RADIUS EXTRACTION

Here we provide projections for the extraction of the proton charge radius based on the run plan, statistics, and systematic uncertainties presented in this report. The run plan will be further optimized once we have detailed information on the rates and beam characteristics for the different beam momentum settings.

The counting statistics are based on the following:

- Beam e and π fluxes were taken from πM1 beam line measurements [38]. The μ flux is a crude estimate based on πM1 measurements for positive polarity at 160 MeV/c and for negative polarity at 270 MeV/c. Total beam flux is limited to 10 MHz.

- The liquid hydrogen is a 4-cm long cylinder, with a density of about 0.07 g/cm^3.

The Kelly form factors [26] were used to estimate the scattering cross section.

- Target entrance and exit windows total 250 μm of kapton. Elastic cross sections were calculated with a parameterization of the *carbon* form factor used in [55] – the chemical formula for kapton is $C_{22}H_{10}N_2O_5$, so we expect that carbon elastic scattering is the dominant contribution. The oxygen form factor is roughly similar in shape to the carbon form factor, but falls faster with Q^2, while the hydrogen in the kapton foil amount to about 0.3% of the hydrogen in the cryotarget. Quasifree scattering rates were estimated from the number of protons in the kapton, assuming equality of free and quasifree cross sections, and neglecting the neutron since G_E^n is small at low Q^2.

- Beam time is 1 month for each momentum at each polarity. Statistical uncertainties are scaled up by a factor of 1.4, to account for the loss of statistical precision associated with measuring and subtracting scattering from the kapton walls, as discussed in Section XIII A 3. The factor of 1.4 over the simple estimate results from dividing the beam time optimally, with about 1/4 of the time spent determining the wall background with a dummy cell with 6x thicker walls, to match the radiation lengths of the target. The factor accounts for the loss of beam time on the hydrogen target and the increase in statistical uncertainty from the subtraction of the endcap contributions.

- The efficiency from trigger through analysis is taken to be 70%. This accounts for dead time, detector efficiency, PID cuts, and not triggering on events with a π beam particle within a 20 ns window.

To extract the radius, we combine measurements from all three beam momenta, and fit the extracted charge form factor with a quadratic polynomial in Q^2. A simple linear fit provides a more precise measure of the slope, but because the form factor is not linear over the full Q^2 range of the measurement, it yields a systematic offset in the value. We estimate this 'truncation' uncertainty in the fit by performing a linear fit to data which follow the standard dipole form for G_E, and using the error made in the radius extraction as a one-sigma estimate for the error associated with truncating the fit after the linear or quadratic terms. For the Q^2 range of this measurement, the truncation error is 0.0236 fm for a linear fit and 0.0040 fm for the quadratic fit. Since the latter is smaller than the uncertainties associated with the statistics and systematic uncertainties, we perform a quadratic fit for the primary extraction.

In the extraction of the radius, we also include an independent normalization factor for each of the three beam momentum settings. This increases the uncertainty on the extracted slope, but accounts for the possibility of any small changes in the normalization of the extracted cross sections for the three different beam energies. For the quadratic fit with three floating normalization factors, the counting statistics (after scaling down to account for the endcap subtraction) yield an uncertainty of 0.0080 fm on the radius for μ^+ and μ^- measurements. The positron measurements should have a statistical uncertainty 20-30% smaller, while the electron measurements have more than 10 times the muon count rate, and so will yield an uncertainty of approximately 0.0030 fm. The estimated point-to-point systematic uncertainties of 0.55% yields an uncertainty of 0.0100 fm in the fit. Combining the statistical, experimental systematic, and truncation uncertainties, we obtain a combined uncertainty on the extracted radius of 0.0140 fm for $\mu+$ and μ^-, 0.0130 fm for e^+, and 0.0110 fm for e^- measurements. Combining the μ^+ and μ^- extractions will allow for improved statistics, but only a slight reduction in the systematic uncertainties, yielding a combined muon scattering extraction uncertainty of δ_R=0.0110 fm, a better than 1.5% measurement of the charge radius.

Note that the lowest momentum setting does not add much to this combined result, as the two higher settings have a greater lever arm in Q^2, while also reaching very low Q^2 values which minimizes the uncertainty in the extrapolation to the known value at $Q^2 = 0$. If the low momentum setting data is analyzed by itself, the range in Q^2 is small enough that the truncation error is not unreasonable, even for a liner fit. In this case, the relative slope of the data within this single setting is sufficient, and the normalization does not have to be determined. By itself, the low momentum setting yields a statistical uncertainty of 0.0080 fm, a systematic uncertainty of 0.0070 fm, and a truncation uncertainty of 0.0100 fm, for a combined uncertainty of 0.0150 fm, comparable to the uncertainty from the μ^+ and μ^- extractions from the higher Q^2 data sets. This yields another extraction of the radius to be compared to the higher momentum data, although because the uncertainty

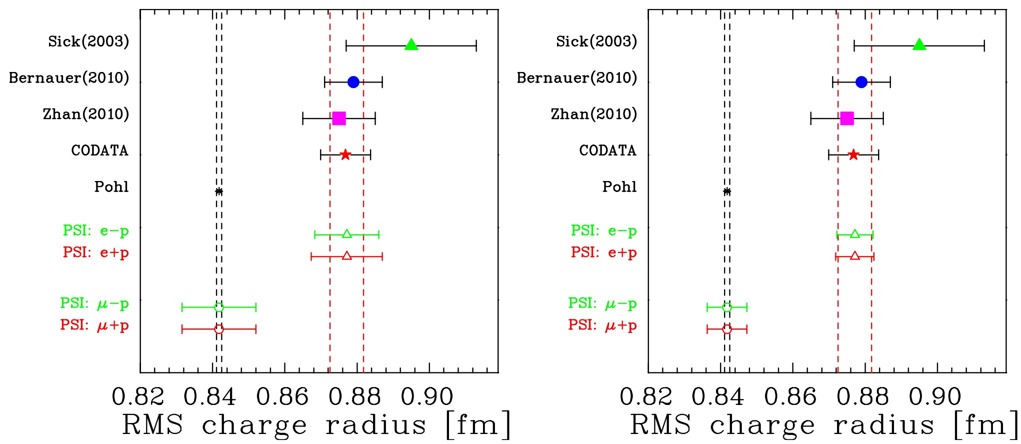

FIG. 60. (Left) Recent extractions of the proton radius from electron and muon based measurements, along with the projected uncertainties from the proposed measurements. (Right) The same recent proton radius results, but with projections for the *relative* uncertainties for the proposed measurements. See text for details.

is not dominated by the statistics, combining the μ^+ and μ^- data does not improve the combined result significantly. The combined results from the extractions using the low momentum data set and the higher momentum data sets yield uncertainties near 0.0100 fm.

Figure 60 shows the existing extractions along with the projections for our proposed measurements. We show results for e^+, e^-, μ^+, and μ^- separately, where we combine the radius extractions from the lowest beam momentum setting and the analysis from the high beam momentum settings. The left panel presents estimates of the absolute radius determined independently in each case. However, certain uncertainties are common to all of our data, particularly the target thickness, so the *relative* uncertainties are significantly smaller than the absolute uncertainties. Thus Figure 60 also shows a determination of the *relative* radius from the different polarities and for e vs. μ. The projected relative uncertainties are close to a factor of two better than the projected absolute uncertainties; this is discussed further below.

Note that the fits tend to be more stable when additional parameters are included when using the continued fraction (CF) form [2], rather than the polynomial expansion, or when using the z-pole expansion [56]. Thus, the truncation uncertainties estimated above are likely to be significant overestimates, making the stand-alone analysis of the lowest energy setting significantly more powerful.

As mentioned above, combining the radius extractions from the $\mu^{\pm}$ and $e^{\pm}$ measurements improves the statistical uncertainty, but has little impact on the systematic uncertainty because many of the contributions (e.g. from any small angle offset or beam energy uncertainty) have a similar or identical effect for all of the different lepton beams. However, this means that in comparison of the different data sets, many of these systematics partially or completely cancel. So in the two-photon exchange extraction from the comparison of e^{+} vs. e^{-} or μ^{+} vs. μ^{-}, or in the direct comparison of electron and muon scattering results, these uncertainties are significantly smaller. In addition, if we are making a comparison of two sets of measurements, rather than an extraction of the absolute charge radius, then the truncation error we make by performing a linear fit is not important. If the electron and muon data both give the same form factor, then the truncation error made in a linear fit will be in both the cases, and will not modify the comparison. There will be a very small difference in this effect, due to the slightly different distribution of the statistics in Q^2 for electrons and muons, but this difference is rather small.

So in the two-photon exchange or lepton universality tests, one can perform the simple linear fit of the entire data set to extract the radius. This yields a statistical uncertainty of 0.0045 fm, a systematic uncertainty below 0.0040 fm (as this number does not account for the cancellation of some systematics), and no truncation error. Thus, for comparisons of the different running conditions, a relative measurement of the proton radius with uncertainty better than 0.0055 fm (0.6%) can be achieved. This is a factor of six smaller than the discrepancy between the values from current electron- and muon-based extractions of the proton charge radius.

XVII. COMMISSIONING AND CALIBRATION

Running the experiment successfully will require that the beam line and detectors be thoroughly and precisely understood. These measurements will be done in three parts. First, we will undertake a series of commissioning measurements during the fall of 2012 to check our understanding of the beam line properties, especially to better determine the muon rates. Second, at the start of the experiment, there will be a period of system commissioning that includes ensuring the equipment is operating properly. Third, during the course of the experiment, particularly as we go to new beam energies, there will be an ongoing series of systematics checks. Some parts of these measurements have been discussed previously.

A. Fall 2012 Measurements

The intent of the planned sequence of measurements for fall 2012 is to determine properties of the μ beam and confirm that planned detector and target designs are sufficient for the experiment.

The sequence of measurements planned is as follows:

- *Commissioning.* Set up data acquisition with a high resolution scintillator positioned approximately at the target position.

- *F12-1: Determine central beam momentum.* This measurement is done with negative polarity beam, and flux reduced by closing the FS11 jaws. The scintillator RF time measurements allow the π and μ momenta to be determined from time differences with the electron peak. As indicated in Table VII, the momentum is measured with 0.1% $\rightarrow$ 0.4% resolution, so the central momentum can be determined to better than 0.1%. This measurement determines the beam e, μ, and π composition at the same time. The measurement will be done both with reduced FS12 jaws, to narrow the beam momentum spread as a check of resolution, and with the full channel momentum acceptance of 3%.

- *F12-2: Determine channel dispersion for muons.* The channel dispersion for π's at DR8 is 7 cm/%, with a resolution of 0.1%. Due to the different production mechanism for μ's, we might expect that the resolution is degraded even though the dispersion should be the same. To confirm the position-momentum correlation and resolution for π's, μ's, and e's, the *F12-1* measurements will be repeated with collimators at the intermediate focal position, DR8. As shown in Figure 21, 3 slits at positions of $\delta p = 0\%$, $\pm1.3\%$ with widths of 0.1% are resolvable at all planned momenta. Thus we plan on a sieve slit with 3 slots, each 7 mm wide, and adjacent slots separated by 9.1 cm, center to center. The collimator needs to be about 3 cm thick to generally ensure that particles going through it lose enough energy to fall outside the channel acceptance, and thus do not overlap the -δ peak. At this point we will also determine the vertical limits of the muons at DR8 that can reach the target position, by blocking off the central region of the beam until no muons reach the target.

- *F12-3: Determine channel dispersion with and energy loss in DR8 detector.* Using the same channel setting with the DR8 scintillating fiber detector installed will lead to ≈1 MeV dE/dx for all particle types and a corresponding shift in the timing spectrum. The detector will have to be commissioned first, confirming that all channels are operational and efficient at the high-voltage settings. This measurement is intended to confirm the dE/dx spectrum resulting from the detector. Because the detector has double ended readout, this measurement will also allow the vertical extent of the beam at the IFP to be confirmed.

- *F12-4: Determine beam size and divergence.* We expect to have two UVa GEMs available for measurements of the size and divergence of the beam in the target region. While the π beam is well measured, the uncertainty here is whether the μ beam has significantly different properties from the π beam. The μ's from decays in flight after the channel do, but we expect that the μ's from the production target are not significantly different.

- *F12-5: Determine target energy spectrum.* We will repeat the measurements of F12-4 with an added thickness of material corresponding to the thickness of all beam detectors placed at the IFP. This is intended as a measurement of the spectrum incident on the target. (These measurements will entail mismatching the channel dipoles to determine the lower energy part of the spectrum.)

- *F12-6: Proton absorber measurements.* While the channel should be symmetric between ± polarities, the proton background is not. The high rates of protons in the channel can be eliminated with an estimated 0.6 – 4.8 mm of plastic absorber, keeping rates in the DR8 scintillating fiber detector low. But since energy losses are statistical, we will vary the thickness of plastic absorber to confirm the minimum amount needed to keep the background proton rate sufficiently small. Note that as this measurement is being done, in each case we are also determining the beam properties at the target, and whether multiple scattering has a significant effect. We do not expect one, as multiple scattering is small compared to the beam divergence.

- *F12-7: Study beam halo.* The beam halo arises from the decay of beam π's and μ's, and should be well simulated, except for some uncertainty from particles decaying in the region of the last magnetic elements of the channel. Here we plan to use the configuration of F12-3 for the channel, but put the target scintillator in various positions where the scattered particle scintillators and wire chambers will go, to sample the background rates of μ's from π decays in flight and e's from μ decays in flight. As part of this measurement we will test reducing the background rates using a shielding wall.

- *F12-8: Target backgrounds.* We will do a simple study of target backgrounds using a thin CH_2 target, the GEM chambers, and the scintillator to check our estimates of the Moller, Bhabha, and δ-ray backgrounds.

Our approach here is that it is valuable in attempting a high-precision experiment to be able to confirm systematic effects with data in the actual experimental conditions, even though much of what we hope to determine can be done through simulations. In addition, adequate statistics for all these measurements can be taken in a short time. The overhead of getting the measurements set up and the system working, plus changing configurations, dominates. The statistics in sampling the beam can be made equal to the proposed statistics of the cross section measurement in data acquisition times of about 1 hour.

B. Commissioning at the Start of the Experiment

Immediately preceding the start of the experiment, there will be a period of installing equipment and performing basic commissioning tasks to ensure its functionality. An example is installation and cabling of scintillators, plateauing of high voltage, and determination of time offsets. Much of this work can be done without the use of the πM1 beam, but brief periods of beam would be useful. It is typical for an experiment of this size to take several weeks to install and commission the basic functioning of the detectors.

The beam tests described above for the fall 2012 period largely do not have to be redone. We do plan during the run to continuously monitor the beam momentum (F12-1) after the target, interspersed with occasional empty-target runs that determine the spectrum incident upon the target. The measurements of the beam energy spectrum (F12-5) will likely be repeated, as the beam line detectors as built will probably be slightly different from our anticipated detectors as of fall 2012. The beam halo studies (F12-7) will be repeated in the as built detector configuration with the installed shielding to determine if there are modifications possible that reduce background rates.

Knowing the scattered particle scintillator efficiencies is crucial to carrying out this experiment. In light of this, it is a useful to run, in advance of the main installation of the experimental equipment, a test with a low-rate beam into a few paddles from the first wall with paddles from the second wall placed behind them, to verify the scintillator efficiency. A loose trigger can be used, and the measured distributions in the second layer can be compared to simulation. It should be sufficient to do this test for three angles of incidence varying the scintillator angles and separations to match the conditions for scattered particles.

An important aspect of the experimental systematics is knowing the scattering angle precisely. Experimentally, this means the relative chamber positions need to be well calibrated. Typically this is a survey problem, but here we outline an approach to determine the position with data. The problem is illustrated in Figure 4. No tracks through the GEM chambers will also directly pass through the scattered particle chambers. (There is a small flux of nearly horizontal cosmic rays that can pass through both scattered particle chambers.) If there were tracks that went directly between the chambers, then these straight-through tracks could be used to calibrate the chamber positions.

The way to calibrate the angles precisely then involves moving the chambers in a precise way so that straight-through tracks allow the relative angles of the GEM and drift chambers to be calculated. Figure 4 suggests how to do this. First, the GEM chambers will be mounted on a platform that allows them to be slid upstream by about 15 cm. Second, the drift chambers are mounted on a rotating table, and will be rotated to several positions, with straight-through tracks aligning the chambers to the GEMs at several angles. The simplest way to implement precise angle changes is through the use of precision dowel holes. The dowel holes can be machined to a precision of ≈10 μm, at a radius of ≈50 cm, leading to relative angle positioning of $\approx \sqrt{2} \times 10$ μm / 50 cm = 0.03 mr. Thus, the determination of the relative angles of the chambers will be determined entirely by limits from the multiple scattering and precision of angle determination of the GEM and drift chambers.

The GEM chambers determine positions at the level of ≈100 μm. Two GEM chambers 40 cm apart then determine the angle to 0.35 mr. However, the GEM chambers are 0.6% L_{rad} thick, and the multiple scattering in the final GEM is what limits knowledge of the track. By using high-momentum pions in the channel for this measurement, multiple scattering can be limited to θ_{ms} ≈1.8 mr.

The drift chambers also have nominal resolutions of ≈100 μm, and the drift chamber should be able to determine angles to ≈0.7 mr, neglecting multiple scattering. Multiple scattering within the chamber adds about 0.5 mr to this, for a total chamber resolution of 0.9 mr.

Finally, the distance between the final GEM chamber and the drift chamber is about 1 m of air, with a multiple scattering of 1.3 mr. This can be reduced to 0.6 mr using a Helium bag instead.

Thus, the resolution for determining the relative angle is 1.8 mr + 0.9 mr + 1.3 mr = 2.4 mr with air, or 2.1 mr with a helium bag. The resolution for determining the transverse chamber position is ≈2 mm. Of course, these are the estimated r.m.s. widths of the distributions that we will measure. Determining the angle or position of the chambers involves determining the centroid of these distributions, which we estimate can be done 5 - 10 times better than the resolution, or to at least 0.5 mr and 0.4 mm. Adding back in the uncertainty in positioning the chambers as we rotate the drift chamber table or slide the GEM chamber table does not significantly affect this. A detail to be concerned with at the mechanical design stage is that the GEM chamber alignment does not change when they are moved from their production data position back upstream to the calibration position.

The determination of the angle of the drift chambers also provides a powerful test of the tracking efficiency of the drift chambers. If at low beam rates there is a track in the GEM chambers pointing into the drift chambers, and a signal from a rear triggering scintillator, then the track passed through the wire chambers. This allows both the wire efficiency and the tracking efficiency to be determined. The same logic also applies to determining the GEM chamber efficiency.

During the commissioning phase it will also be important to determine that backgrounds are under control. An initial measurement can be done of the empty target background; with only air in the beam line and the GEM chambers and target SciFi array out of the beam, all events in the scattered particle wire chambers and scintillators will come from decay particles, scattering from air, background radioactivity including cosmic rays, and scattering from the downstream scintillator. With the beam GEMs and target SciFi in place, background associated with these detectors can be determined. It might be possible to install small additional amounts of shielding to further reduce beam-related backgrounds.

C. Calibrations During the Experiment

The commissioning activities should provide functioning detectors and a working data acquisition system. In addition the alignment of the detectors will be determined. While many of these activities do not need to be repeated, there are additional calibrations that need to be performed at each beam setting, and some that need to be monitored regularly.

Determining the beam momentum was discussed in Section V. This will be a dedicated measurement for each beam momentum setting. Related to the beam momentum calibration is the calibration of the RF timing and the efficiency of the beam particle identification FPGA system. Setting up the FPGA system for each configuration has already been discussed in Section IV B. This is basically the same measurement as the beam momentum determination, setting up the cuts for particle types and varying the incident flux to understand the system efficiencies. Note that because the RF time separation of particles depends on the beam momentum and position of the beam line SciFi detectors, an initial part of these procedures during the actual run will be determining if the beam momentum should be adjusted slightly up or down to optimize the particle identification.

As indicated in Figure 4, we plan to have a high-precision scintillator downstream of the target. This scintillator will allow us to continuously monitor for variations in the beam particle and time / momentum distributions, although it will not provide an absolute measurement due to interactions with the target. If there are indications of changes, it will be necessary to perform another beam momentum and particle identification system calibration. At present, it is believed that there is little variation in the RF time of the particles, except for some variations after some accelerator trips. We will have to study this better in the initial phases of the run with the high-precision scintillators.

Finally, we note that the detectors are in general redundant, which allows efficiencies to be determined from the data. The beam SciFi's have 2 planes at the IFP when 1 is needed, and 3 planes at the target when 2 are needed. There are 3 GEM and chambers instead of the 2 needed, and 3 drift chambers as well in each arm. For the scattered particle scintillators, we do not have additional layers, but based on the simulations we should be able to confirm the efficiency found in the simulations through a comparison of the ADC spectra measured for good events compared to the simulated spectra. Thus the data itself should continuously provide calibrations of the detector efficiencies.

XVIII. COLLABORATION

We summarize the institutional responsibilities for the major components of experimental hardware in Table XV. In addition, Guy Ron of Hebrew University is responsible for coordinating the data acquisition system, John Arrington of Argonne is responsible for analysis and fitting, Katherine Myers of Rutgers University will coordinate simulations, and Andrei Afanasev of George Washington University is responsible for radiative corrections. Ron Gilman is contact person for the experiment, but the collaboration includes a core group of people who have been working together collegially in cases for up to 25 years, and we expect to operate largely by consensus.

TABLE XV. Institutional responsibilities for experimental hardware.

Component	Person	Institution
Beamline and shielding	Konrad Dieters	PSI
Beam SciFi's	Eli Piasetzky	Tel Aviv
GEMs	Michael Kohl	Hampton
GEMs (for fall 2012 tests)	Nilanga Liyanage	UVa
Target	Ron Gilman	Rutgers
Drift chambers	Shalev Gilad	MIT
High precision scintillators	Steffen Strauch	South Carolina

[1] P. J. Mohr, B. N. Taylor, and D. B. Newell, Rev.Mod.Phys. **80**, 633 (2008), arXiv:0801.0028 [physics.atom-ph]

[2] I. Sick, Phys.Lett. **B576**, 62 (2003), arXiv:nucl-ex/0310008 [nucl-ex]

[3] R. Pohl, A. Antognini, F. Nez, F. D. Amaro, F. Biraben, *et al.*, Nature **466**, 213 (2010)

[4] J. Bernauer *et al.* (A1 Collaboration), Phys.Rev.Lett. **105**, 242001 (2010), arXiv:1007.5076 [nucl-ex]

[5] X. Zhan, K. Allada, D. Armstrong, J. Arrington, W. Bertozzi, *et al.*, Phys.Lett. **B705**, 59 (2011), arXiv:1102.0318 [nucl-ex]

[6] B. Batell, D. McKeen, and M. Pospelov, Phys.Rev.Lett. **107**, 011803 (2011), arXiv:1103.0721 [hep-ph]

[7] V. Barger, C.-W. Chiang, W.-Y. Keung, and D. Marfatia, Phys.Rev.Lett. **108**, 081802 (2012), 3 pages, 3 figures. Version to appear in PRL, arXiv:1109.6652 [hep-ph]

[8] G. Miller, A. Thomas, J. Carroll, and J. Rafelski, Phys.Rev. **A84**, 020101 (2011), arXiv:1101.4073 [physics.atom-ph]

[9] J. Carroll, A. Thomas, J. Rafelski, and G. Miller, Phys.Rev. **A84**, 012506 (2011), 11 pages, 1 figure. v2: Enhanced introduction and minor change to concluding numerical value (interpretation unchanged). v3: Minor changes, matches version published in Phys. Rev. A, arXiv:1104.2971 [physics.atom-ph]

[10] J. D. Carroll, A. W. Thomas, J. Rafelski, and G. Miller, AIP Conf.Proc. **1354**, 25 (2011), delayed arXiv submission. To appear in 'Proceedings of T(R)OPICALQCD 2010' (September 26 - October 1, 2010). 7 pages, 1 figure. Superseded by arXiv:1104.2971, arXiv:1105.2384 [physics.atom-ph]

[11] G. Miller, (2011), private communication

[12] A. De Rujula, Phys.Lett. **B693**, 555 (2010), arXiv:1008.3861 [hep-ph]

[13] A. De Rujula, Phys.Lett. **B697**, 26 (2011), arXiv:1010.3421 [hep-ph]

[14] I. C. Cloet and G. A. Miller, Phys.Rev. **C83**, 012201 (2011), arXiv:1008.4345 [hep-ph]

[15] M. O. Distler, J. C. Bernauer, and T. Walcher, Phys.Lett. **B696**, 343 (2011), 6 pages, 4 figures, final version includes discussion of systematic and numerical errors, arXiv:1011.1861 [nucl-th]

[16] B. Y. Wu and C. W. Kao, (2011), arXiv:1108.2968 [hep-ph]

[17] C. E. Carlson and M. Vanderhaeghen, (2011), arXiv:1109.3779 [physics.atom-ph]

[18] G. Paz, (2011), arXiv:1109.5708 [hep-ph]

[19] R. J. Hill and G. Paz, Phys. Rev. D **82**, 113005 (2010)

[20] R. J. Hill and G. Paz, Phys. Rev. Lett. **107**, 160402 (2011)

[21] L. Cardman, J. Lightbody Jr., S. Penner, S. Fivozinsky, X. Maruyama, W. Trower, and S. Williamson, Phys.Lett. **B91**, 203 (1980)

[22] E. Offermann, L. Cardman, C. de Jager, H. Miska, C. de Vries, *et al.*, Phys.Rev. **C44**, 1096 (1991)

[23] L. Schaller *et al.*, Nucl.Phys.A **379**, 523 (1982)

[24] W. Ruckstuhl, B. Aas, W. Beer, I. Beltrami, K. Bos, *et al.*, Nucl.Phys. **A430**, 685 (1984)

[25] R. Ellsworth, A. Melissinos, J. Tinlot, H. Von Briesen, T. Yamanouchi, *et al.*, Phys.Rev. **165**, 1449 (1968)

[26] J. Kelly, Phys.Rev. **C70**, 068202 (2004)

[27] L. Camilleri, J. Christenson, M. Kramer, L. Lederman, Y. Nagashima, *et al.*, Phys.Rev.Lett. **23**, 153 (1969)

[28] I. Kostoulas, A. Entenberg, H. Jostlein, A. Melissinos, L. Lederman, *et al.*, Phys.Rev.Lett. **32**, 489 (1974)

[29] A. Entenberg, H. Jostlein, I. Kostoulas, A. Melissinos, L. Lederman, *et al.*, Phys.Rev.Lett. **32**, 486 (1974)

[30] L. Camilleri, J. Christenson, M. Kramer, L. Lederman, Y. Nagashima, *et al.*, Phys.Rev.Lett. **23**, 149 (1969)

[31] V. Tvaskis, J. Arrington, M. Christy, R. Ent, C. Keppel, *et al.*, Phys.Rev. **C73**, 025206 (2006), arXiv:nucl-ex/0511021 [nucl-ex]

[32] J. Arrington *et al.*, "A Measurement of Two-Photon Exchange in Unpolarized Elastic Electron-Proton Scattering," Jefferson Lab experiment 05-017.

[33] A. Gasparian *et al.*, Jefferson Lab PAC38 proposal PR-11-1xx, unpublished.

[34] R. Gilman, unpublished.

[35] G. Ron, E. Piasetzky, and B. Wojtsekhowski, JINST **4**, P05005 (2009), arXiv:0904.0686 [nucl-ex]

[36] J. Beringer *et al.* (Particle Data Group), "The Review of Particle Physics," (2012)

[37] P. J. Mohr, B. N. Taylor, and D. B. Newell, ArXiv e-prints (2012), arXiv:1203.5425 [physics.atom-ph]

[38] R.A. Schumacher and U. Sennhauser, "Particle Fluxes in πM1," unpublished, 1987.

[39] P. G. Blunden and I. Sick, Phys.Rev. **C72**, 057601 (2005), arXiv:nucl-th/0508037 [nucl-th]

[40] J. Arrington, P. Blunden, and W. Melnitchouk, Prog.Part.Nucl.Phys. **66**, 782 (2011), arXiv:1105.0951 [nucl-th]

[41] J. Arrington, Phys.Rev.Lett. **107**, 119101 (2011), arXiv:1108.3058 [nucl-ex]

[42] J. Bernauer, P. Achenbach, C. Ayerbe Gayoso, R. Bohm, D. Bosnar, *et al.*, Phys.Rev.Lett. **107**, 119102 (2011)

[43] E. L. Lomon, Phys.Rev. **C64**, 035204 (2001), arXiv:nucl-th/0104039 [nucl-th]

[44] P. Reimer *et al.*, Fermilab experiment 906, `http://www.phy.anl.gov/mep/SeaQuest/index.html`.

[45] E907 target web pages are at: `http://ppd.fnal.gov/experiments/e907/Targets/CryoTarget.html`.Shut Stop

[46] R. Gothe, E. Phelps, R. Steinman, and Y. Tian, "CLAS12 Forward Time-of-Flight at USC: A Comprehensive Update", Department of Physics and Astronomy, University of South Carolina, unpublished, November 2009, `http://www.physics.sc.edu/~gothe/research/pub/FToF12-review-11-09.pdf`

[47] N. Liyanage, "Commissioning of Tracking Package for Bigbite Spectrometer," unpublished, 2012.

[48] M. Mihovilovic, K. Allada, B. Anderson, J. Annand, T. Averett, *et al.*, Nucl.Instrum.Meth. **686**, 20 (2012), arXiv:1201.1442 [nucl-ex]

[49] R.D. Ransome, "Measurement of the Free Neutron-Proton Analyzing Power and SPin Transfer Parameters in the Charge-Exchange Reaction at 790 MeV," Ph.D. thesis, Los Alamos Report LS-8919-T, 1981.

[50] R. Ent, B. Filippone, N. Makins, R. Milner, T. O'Neill, *et al.*, Phys.Rev. **C64**, 054610 (2001)

[51] F. Weissbach, K. Hencken, D. Rohe, I. Sick, and D. Trautmann, (2004), arXiv:nucl-th/0411033 [nucl-th]

[52] A. Afanasev, I. Akushevich, and N. Merenkov, Phys. Rev. D **64**, 113009 (2001)

[53] P. Blunden, W. Melnitchouk, and J. Tjon, Phys.Rev. **C72**, 034612 (2005), arXiv:nucl-th/0506039 [nucl-th]

[54] D. Borisyuk and A. Kobushkin, Phys.Rev. **C75**, 038202 (2007), arXiv:nucl-th/0612104 [nucl-th]

[55] S. Boffi, M. Bouten, C. C. D. Atti, and J. Sawicki, Nuclear Physics A **120**, 135 (1968)

[56] R. J. Hill and G. Paz, Phys.Rev. **D82**, 113005 (2010), arXiv:1008.4619 [hep-ph]